

ABSTRACT

MONEGHAN, DANIEL. Characterization of a Fibrous Magnesium Phosphate Concrete for Nuclear Waste Storage Applications. (Under the direction of Dr. Mohamed Bourham and Dr. Jacob Eapen).

Nuclear waste storage is a broad field that intersects with several industries. Hospitals employ radioisotopes for nuclear medicine, generating radioactive waste in the form of contaminated needles and other biohazardous materials. Radioactive sludge and salt from the production of weapons grade radioisotopes are stored at sites such as Hanford and Savannah River. Commercial power and research reactors generate waste in the form of spent nuclear fuel; the radioactive fuel assemblies take years to decay to the point of safe storage even within concrete. Materials that have been used to design these structures are with interim lengths in mind; they may provide adequate containment for a design life of up to a century.

The goal of this project was to optimize an aggregate composition for use with a magnesium phosphate cement binder to create a better shielding concrete, and thoroughly investigate its suitability for use in a variety of nuclear waste storage applications. This was done through experiments designed to evaluate the material characteristics related to gamma attenuation, mechanical strength, corrosive/erosive behavior, outgas mass retention, and thermal degradation. After evaluating dozens of compositions of aggregates for their gamma attenuation and mechanical strength properties to verify minimum acceptable standards for a shielding concrete, two aggregate compositions were arrived at for further investigation in this project. In addition to samples of Portland concrete and base magnesium phosphate concrete (MPC) as control samples, MPC Base with powdered aggregate of 20% lead and 20% magnetite (MPC 2020 hereafter), as well as MPC Base with powdered aggregate of 30% lead and 30% magnetite (MPC 3030 hereafter) were used in this project.

Gamma attenuation experiments, using a variety of sources chosen to approximate the range of spent nuclear fuel, for measuring the linear attenuation coefficient of the materials, shows that both aggregate samples (MPC 2020 and MPC 3030) improve on the control groups by more the 70%. Basic mechanical evaluation of the ultimate compressive force shows minor improvement on the part of MPC 2020, and minor loss on the part of MPC 3030. Corrosion/erosion circulators provide a means to study the degradation of the material in acidic conditions and in brines; test results

indicate that both aggregate samples have reduced mass loss due to acidolysis by more than a factor of two in highly acidic conditions. Long-time 55 °C drying is used to evaluate the mass retention due to outgassing of the materials, which is the only experiment in which aggregate samples underperformed compared to MPC Base, though all three retain more mass than Portland.

At ambient conditions, MPC 2020 appears to be a vast improvement over Portland cement for use in the nuclear waste field. Differential scanning calorimetry is used in the thermal stability investigation, starting with a simple heating cycle on MPC Base from 40 to 180 °C. This shows an exotherm starting around 56 °C. Further investigation shows the presence of similar exotherms in MPC 2020 and MPC 3030, but none in Portland. This exotherm indicates a phase change took place within the MPC compositions, likely within the magnesium phosphate binder phase. X-ray powder diffraction (XRD), scanning electron microscopy (SEM), and various spectroscopy techniques are employed to determine the nature of this phase change. The results of this characterization are supported by literature, which indicate a one-step dehydration reaction occurs in the potassium magnesium phosphate hydrate (struvite-k) phase within the MPC. This reaction effectively consumes the primary strength-conveying hydration product of the concrete and volatilizes the water, weakening the material and creating large amounts of outgas at temperatures above the reaction threshold.

This experiment concludes that while aggregates inhibit the dehydration of MPC compositions, it is not to a sufficient threshold to be suitable for use in applications with high heat levels, such as those within a dry storage cask due to the phase change at a relatively low temperature of 56 °C. MPC compositions are, however, highly effective at ambient temperatures, and as such are suitable candidates for many other applications in nuclear waste storage. The dry cask superstructures could be improved in strength without an increase in geographic footprint, providing increased safety for the same design constraints. Radioisotopes could be grouted with MPC to be more optimally entrained, provided that a layer of non-immobilizing concrete, MPC or otherwise, is hydrated around the grout to protect it from direct heating incidents. Medical facilities that handle radioactive sources such as x-ray or radioactive materials can use MPC 2020 instead of layering lead and Portland concrete to reduce the amount of material needed to construct these shielded areas. For applications with normal operating conditions below 55 °C, MPC has superior characteristics and should be considered for use in nuclear waste facilities or industry.

Characterization of a Fibrous Magnesium Phosphate Concrete for Nuclear Waste Storage
Applications

by
Daniel Moneghan

A dissertation submitted to the Graduate Faculty of
North Carolina State University
in partial fulfillment of the
requirements for the degree of
Doctor of Philosophy

Nuclear Engineering

Raleigh, North Carolina

2020

APPROVED BY:

Dr. Mohamed Bourham
Co-chair

Dr. Jacob Eapen
Co-chair

Dr. Ralph Smith

Dr. Ge Yang

BIOGRAPHY

Dan Moneghan was born in Newton, Massachusetts on the 18th of May, 1993. After moving to Texas, and then Massachusetts again, then Virginia, then up to Connecticut, and then back to Virginia, he attended Atlee High School, graduating 6th in his class with a focus on engineering and mathematics.

Dan attended Virginia Polytechnic Institute and State University for four years, earning a Bachelor of Science in Chemical Engineering. During the course of his studies he made lifelong friends, learned to write in the third person, and grew to respect the challenges that climate change posed to society. He sought change from his petroleum dominated industry, by pursuing a Master of Science in Nuclear Engineering with Dr. Leigh Winfrey, whom he worked for as an undergraduate researcher. He received this degree from the University of Florida, before moving to Raleigh, North Carolina to work under her former advisor, Dr. Mohamed Bourham and his colleague Dr. Jacob Eapen. He has spent the past several years working with magnesium phosphate concretes, attempting to create an aggregate blend that can be used in nuclear waste storage to minimize material usage and replace the environmentally damaging Portland concretes that are the industry standard.

ACKNOWLEDGEMENTS

I would first like to thank my wife, Claire. Her constant support and encouragement helped me through this challenging and rewarding experience. I also owe a great deal to Dr. Eapen and Dr. Bourham for guiding both this research effort and me along the way. Thanks to them I have grown as a person in addition to developing as a researcher. Will and Cooper were both incredibly helpful to me in executing many of the experiments needed to complete this work; without their efforts, several aspects of this work would not have been fully completed. My parents, brother, wife's parents, and so many friends have also contributed through their insightful questions and technical suggestions, giving me new ideas to consider and pursue. Finally, sincere thanks to Armakap Technologies LLC. for funding this research and providing the MPC samples used in this work, this work couldn't be completed without their support.

TABLE OF CONTENTS

LIST OF TABLES	vii
LIST OF FIGURES	viii
Chapter 1. An Introduction to Concrete.....	1
1.1 Composition of Concrete	1
1.1.1 Cement.....	2
1.1.2 Aggregate.....	3
1.1.3 Concrete Reinforcement	4
1.1.4 Fibrous Concrete.....	5
1.2 Concrete Hydration Chemistry.....	6
1.2.1 Portland Cement Hydration	6
1.2.2 Magnesium Phosphate Cement Hydration	8
1.2.3 Microstructural Differences.....	9
1.3 Concrete in Nuclear Waste Storage	10
1.3.1 HLW - Spent Fuel Pools.....	10
1.3.2 HLW - Dry Storage Casks.....	11
1.3.3 LLW - Medical Radiowaste Disposal	12
Chapter 2. Project Motivation and Objectives	14
2.1 Technical Gaps in Nuclear Waste Storage	14
2.1.1 Corrosion of Embedded Steel.....	14
2.1.2 Thermal Degradation of Mechanical Properties and Dryout.....	15
2.1.3 Coupled Mechanisms	16
2.2 Project Objectives	16
2.2.1 Composition Optimization	16
2.2.2 Gamma Attenuation Properties	17
2.2.3 Corrosion/Erosion Properties	17
2.2.4 Mechanical Properties	18
2.2.5 Outgas Properties.....	18
2.2.6 Thermal Properties	19
Chapter 3. Concrete Composition Optimization.....	20

3.1 Introduction	20
3.2 Methods	21
3.3 Results	22
3.3.1 Attenuation	22
3.3.2 Compressive Strength.....	24
3.4 Conclusion.....	24
Chapter 4. Gamma Attenuation Properties	26
4.1 Introduction	26
4.2 Methods.....	29
4.3 Results	31
4.3.1 Impact of Cure Time.....	34
4.4 Conclusion.....	36
Chapter 5. Corrosion/Erosion Properties	37
5.1 Introduction	37
5.2 Methods.....	38
5.3 Results	40
5.4 Conclusion.....	43
Chapter 6. Mechanical Properties	45
6.1 Introduction	45
6.2 Methods.....	46
6.3 Results	46
6.4 Conclusion.....	48
Chapter 7. Outgas Properties	49
7.1 Introduction	49
7.2 Methods.....	50
7.3 Results	50
7.4 Conclusions	51
Chapter 8. Material Degradation Properties	52
8.1 Concrete Dehydration	52
8.2 Dehydration Evaluation Methods.....	53
8.2.1 Differential Scanning Calorimetry	54
8.2.2 X-Ray Powder Diffraction.....	55

8.2.3 Scanning Electron Microscopy and Energy-Dispersive X-Ray Spectroscopy.....	57
8.2.4 X-Ray Photoelectron Spectroscopy	59
8.3 Dehydration Characterization Results.....	61
8.3.1 DSC Results.....	61
8.3.2 XRD Results	64
8.3.3 SEM and EDS Results	69
8.3.4 XPS Results	74
8.4 Dehydrated Mechanical Results	77
8.5 Dehydrated Attenuation Results	79
8.6 Dehydrated Outgas Results	80
Chapter 9. Evaluation of the Suitability for Nuclear Waste Storage	82
9.1 Summary	82
9.2 Conclusions	83
9.4 Future Work	84
References.....	85

LIST OF TABLES

Table 1. Ultimate compressive strength.....	24
Table 2. Average mean free paths of typical energy radiation in common materials	26
Table 3. The linear attenuation coefficient	32
Table 4. The mass attenuation coefficient	33
Table 5. The tenth-value layer in cm for each concrete.....	34
Table 6. Ultimate compressive force and density of selected samples.....	48
Table 7. Outgas mass loss in percent of initial mass over a 24 hr drying at 55 °C.	50
Table 8. The elemental change in percent of MPC Base from pre- to post-dehydration samples.	76
Table 9. Mechanical property changes as a result of dehydration	78
Table 10. Average linear attenuation changes as a result of dehydration.....	80
Table 11. Property comparison for rigorously tested samples below 50 °C.....	84

LIST OF FIGURES

Figure 1. Tobermorite as viewed along a polysilicate chain.	7
Figure 2. An ettringite column.....	8
Figure 3. The mineral structure of struvite-k.....	9
Figure 4. (a) C-S-H gel in Portland concrete, and (b) Struvite-k in MPC	10
Figure 5. A spent fuel pool and transfer system for pressurized water reactors.....	11
Figure 6. dry storage cask design.....	12
Figure 7. Dual delay tank system.....	13
Figure 8. Samples used to optimize MPC composition.....	21
Figure 9. The linear attenuation coefficient of varying aggregate MPC	23
Figure 10. The dominance of photon interactions	27
Figure 11. The experimental setup for gamma ray attenuation.	30
Figure 12. spectrum produced by spent fuel assemblies.....	30
Figure 13. The linear attenuation coefficient.....	31
Figure 14. The mass attenuation coefficient.	33
Figure 15. The linear attenuation coefficient post cure	35
Figure 16. the high-density aggregate.....	36
Figure 17. Four individual circulators	39
Figure 18. Wetted mass by day for circulator solution of 6.3 pH for the four chosen samples. ..	40
Figure 19. Wetted mass by day for circulator solution of 0.7 pH for the four chosen samples. ..	41
Figure 20. Mass change rates in mmpy for selected samples for both pH circulator solutions....	42
Figure 21. The samples 60 in circulators compared to fresh samples.	43
Figure 22. Ultimate compressive force of selected samples.....	47
Figure 23. The mass difference due to outgassing after 24 hours of heating at 55 °C.	50
Figure 24. A sample schematic representing the DSC process.	54
Figure 25. The generation of Bremsstrahlung radiation	55
Figure 26. The atomic scale principles of EDS	58
Figure 27. The photoelectric effect as applied in XPS (Moulder, 1991).....	60
Figure 28. Heat flow curves output by the DSC Q200 for a 40 to 170 °C heating.	61
Figure 29. Progression of the dehydration reaction through MPC 2020 at 115 °C.....	62
Figure 30. Progression of the phase change front in MPC Base at 115 °C.	63

Figure 31. Progression of the phase change front in MPC 2020 at 115 °C.	63
Figure 32. Two XRD 2 θ graphs of struvite-k from different studies	64
Figure 33. Plot of the peak intensity over the tested 2 theta range for Portland.	65
Figure 34. Plot of the peak intensity over the tested 2 theta range for MPC Base.	65
Figure 35. Plot of the peak intensity over the tested 2 theta range for MPC 2020.	66
Figure 36. Plot of the peak intensity over the tested 2 theta range for MPC 3030.	66
Figure 37. Plot of the peak intensity over the tested 2 theta range pre- and post-dehydration.	68
Figure 38. Comparative 2 θ peak graphs showing pre- and post-dehydration MPC Base.	68
Figure 39. Portland (left) and MPC Base (right) at 100x magnification.	70
Figure 40. MPC Base pre- and post-dehydration at, left: 1000x; and right: 800x.	70
Figure 41. MPC 3030 at 1000x with EDS elemental mapping.	71
Figure 42. MPC Base at 100x, displaying individual element maps.	72
Figure 43. MPC Base at 100x, displaying different individual element maps.	73
Figure 44. XPS survey scan of MPC Base pre-dehydration.	74
Figure 45. XPS survey scan of MPC Base post-dehydration.	75
Figure 46. XPS high-resolution normalized peaks for pre- and post-dehydration MPC Base.	76
Figure 47. Ultimate compressive force pre- and post-dehydration.	77
Figure 48. Density pre- and post-dehydration	78
Figure 49. Linear attenuation coefficient pre- and post-dehydration	79
Figure 50 Outgas mass loss before dehydration and through dehydration for all tested samples.	80

Chapter 1. An Introduction to Concrete

1.1 Composition of Concrete

Concrete is a composite material formed by the hydration of a binder mixed with aggregate that hardens into a heterogeneous solid with high compressive strength. The most common binder today is Portland cement, though materials like asphalt are often used in applications such as roadway construction. Portland based concrete is so ubiquitous in industry that Portland cement is the second most consumed resource on the planet, surpassed only by water (Li, Tharakan, Macdonald, & Liang, 2013), though it is not the only option. Magnesium phosphate cement, for example, is a faster curing binder that is believed to provide many superior properties compared to that of the industry standard Portland (Walling & Provis, 2016) (Park, Kim, & Ann, 2016).

Aggregate materials have much more variety due to the large impact of composition, particle size, surface roughness, and many other features on the final properties of the concrete. Many production concretes utilize internal reinforcement, most often in the form of reinforcing steel (rebar). Rebar improves the tensile strength of concrete along the length of the reinforcement, one of the most lacking qualities of concrete. Tensile strength can also be augmented further using fibers within the concrete matrix, which provide an isotropic increase through random orientation of small filaments of a variety of materials. These together make up the particular material that is the investigation of this project, namely a fibrous magnesium phosphate concrete (Walling & Provis, 2016) with fine aggregate intended for use in reinforced structures.

1.1.1 Cement

Portland cement is a mixture of calcium silicates, aluminates, and ferrites that is formed by the heating of limestone with clay or shale which is then ground with gypsum. Each of these steps supplies a different source material into the process, creating the final blended mixture that is able to react with water forming a typical cement paste (Kosmatka & Wilson, 1988). This process is sufficiently capable of meeting the demand for cement in modern society, but it is not without flaws. Cement production is responsible for around 10% of the anthropogenic global emission of CO₂ (Mommaas, 2014). While some companies are attempting to address this issue, there has not been any industry wide movement to implement change. Despite some efforts for carbon capture being trialed in Norway in 2020, there is no great expectation for large-scale shift away from Portland based concretes (Bjerge & Brevik, 2014).

A distinct line of development on the traditional Portland cement began in 1867 with Stanislas Sorel (Sorrell, 1977). He created the eponymous ‘Sorel cement’ which uses magnesium oxide and magnesium chloride instead of limestone. The result of this change created a significantly stronger material that achieves peak strength faster (Dorrepaal & Gowen, 2018) while only reaching a pH of around 9, compared to that of 13 in Portland (Brichni, Hammi, Aggoun, & Adel, 2016). Sorel cement represented an improvement on Portland in many ways, but it could not form a hydraulic concrete. The resulting concrete was water permeable, which lead to accelerated corrosion of reinforcing metals when compared to Portland. As a consequence of being strictly inhydraulic, it leaches out part of the binding phase with prolonged exposure to water, resulting in a loss of strength.

The benefits of Sorel cement were impressive enough that the idea was not abandoned due to the limitations of the material. It developed into what is more commonly used today: magnesium phosphate cement. The base of Sorel cement remains the same in magnesium phosphate cements, but soluble phosphates are added instead of chlorides, which react with the magnesium base to form potassium phosphates. These then react with the magnesia present, and through an acid-base reaction form a gel which crystallizes into an insoluble phosphate binder, referred to as either potassium magnesium phosphate hydrate or as struvite-k (Hewlett, 2019). The added benefit of this process is the phosphate binder limits the penetration of water into the concrete, and with certain formulations can create a water impermeable material. The prevention of water penetration

and the ability for this process to take place hydraulically are what allow magnesium phosphate cements to succeed where the initial Sorel cement could not.

1.1.2 Aggregate

Aggregate material is less standardized than the choice of binder. Large size aggregates range from coarse gravel to crushed limestone and granite, while finer materials like metal powders and shot or ground up waste products are often used (Dhir, Brito, Silva, & Lye, 2019). Today, most aggregates are produced locally to the construction site, within some twenty-five miles on average. This contributes to the slight batch inconsistency present in concrete, and as most aggregate is locally sourced the qualities of a concrete pour can vary between regions despite use of a consistent binder. Typically, this is not an issue, but it can cause minor discrepancies in material properties.

One of the most common aggregates used in construction is recycled concrete that is crushed up and reintroduced to a binder during hydration. This recycled concrete typically comes from the demolition of existing construction projects, thus minimizing the material waste from rebuilding structures in safer and more sustainable ways (Rao, Jha, & Misra, 2007). In mixes, recycled concrete aggregate can be used as up to 30% by mass of the final cement mix without property loss. When used in concentrations greater than that, creep and drying shrinkage will increase, and while the compressive strength remains approximately the same the tensile strength is further reduced (Portland Cement Association, 2019).

Most concretes require 70-75% of the mass of a mixture to be aggregate, but this is further broken down into size categories (Sonawane & Pimplikar, 2019). Coarse aggregates are defined as aggregate pieces larger than can fit through a Standard No. 4 sieve but less than 2 inches in any dimension. Fine aggregates are defined as aggregate pieces that pass through a Standard No. 4 sieve, but are retained by a Standard No. 200 sieve (Mahmud, 2019). On average, two-thirds of concrete aggregate is coarse while the balance is fine aggregate (Sonawane & Pimplikar, 2019).

Aggregate usage to intentionally modify properties of concrete for nuclear waste disposal is not as widespread as it is in the construction industry for a variety of reasons. The primary use of modified concretes in this field is in so called ‘grouting’ applications, where highly radioactive fission fragments and similar waste are blended with concrete formers and stored in large drums to

eventually be buried somewhere (Spalding, Hyder, & Munro, 1985). This is currently an ongoing project at both Pacific Northwest National Lab and the Savannah River Site to dispose of much of the waste associated with nuclear weapons production from 1945 through 1990 (Greenberg, et al., 2007). Applications such as these primarily value the ability for the material to entrain radioactive particles. It is likely of concern to researchers in this area that larger aggregates present more escape pathways for any unbound but contained particles. This is not the only use of concrete in the nuclear waste storage field, though.

Concrete is used to build a variety of structures that directly and indirectly contain radioactive waste, many of which do not have concerns about the entrainment of radioactivity within the matrix itself. With regards to high-level waste (HLW) storage, aggregates are not considered for their use as a radiation attenuator, with the International Atomic Energy Agency report defining the purpose of aggregates as simply, “Inert particulate or granular minerals added as fillers. They dilute the heat of hydration and reduce shrinkage in the course of hardening. (International Atomic Energy Agency, 2013)” In applications like these, high-Z aggregates that improve material shielding without reducing the strength seem to be worth consideration. Radioactive waste, in a variety of forms, generated by nuclear medicine primarily undergo decay in shielded storage before being released for traditional disposal (Ravichandran, Binukumar, Sreeram, & Arunkumar, 2011). This is another application in which the entrainment of radioisotopes is not of concern, as the efficient shielding and housing of the low-level waste (LLW) is what matters.

1.1.3 Concrete Reinforcement

While these materials contribute various benefits to the properties of concrete, much industrial concrete uses reinforcement to improve the lacking tensile strength of the base material. The first use of reinforced concrete was in 1853 in the creation of Coignet’s four story house in Paris (Bell, 2019). While it is true that he added iron into the concrete walls of his house, he described the intent as simply keeping the walls in such a large monolithic construction from falling over (Condit, 1968). Due to this admission, many consider the first reinforced concrete structure to be one that took advantage of the ability to intentionally control stresses within concrete using metal.

This was done by William B. Wilkinson, who used reinforcement in the roof and floor of a concrete house he constructed to distribute tensile loads across the surface (Brown, 1966).

In addition to the tensile strength improvement that embedded steel allows for in concrete, the concrete benefits the steel, protecting it from corrosion through the process of passivation. As the concrete hardens and bonds to the steel rebar within, a passivating film forms in the interface due to the presence of calcium hydroxide in the highly alkaline environment created by the abundance of potassium and sodium hydroxides in the cement paste. This protects the steel from acidity, even as the concrete hardens and drops from a pH of 13 to around 8.5 through exposure to atmospheric carbon dioxide (Ferreira & Simoes, 1995). In nuclear waste storage, approximately 40% of the deployed dry storage casks use a reinforced concrete overpack (Gencturk & Attar, 2015). The protection of the embedded rebar is a high priority in spent nuclear fuel storage, as corrosion cracking within the overpack is a common problem. Radioactive waste generated from nuclear medicine has less concerns related to this as most decay storage tanks don't present conditions where corrosion of any embedded steel is likely.

1.1.4 Fibrous Concrete

Around the same time that reinforced concrete was growing in popularity in the modern era, other such developments were taking place. Ludwig Hatschek is credited with the creation of the first fiber-reinforced cement after mixing 90% Portland cement with 10% asbestos fiber (Mai, 1979). The mixing of this with water formed sheets that are similar in function to aluminum siding seen today in lower-cost housing structures. While the initial application of fibers into cements lost popularity due to the extreme health hazard that asbestos created, research into the concept has continued. Currently, fibrous concretes are most commonly made using cellulose or steel but maintain their historical application as siding materials and corrugated sheets (Beaudoin, 1990).

Fibrous concretes have some history of testing for use in nuclear power plants and high-level waste disposal as they require some of the highest performing concrete of any industry (Kamal, Safan, Etman, & Salama, 2014). Despite multiple studies evaluating fibrous concretes using materials like recycled PVC fibers (Kurup & Kumar, 2017) or hybrids of steel and polypropylene (Komloš,

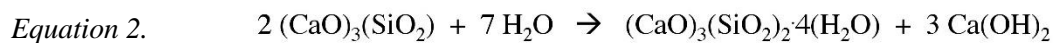
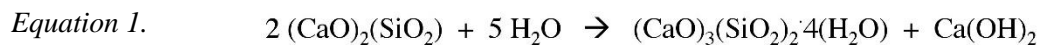
Babál, & Nürnbergerová, 1995), there is no major adoption of this technology in radioisotope waste packages.

1.2 Concrete Hydration Chemistry

Strictly speaking, there are as many chemical reactions to form concrete using a single precise composition of cement as there are aggregate materials, aggregate sizes, admixture materials, admixture concentrations, and for each such set across these four dimensions there are a multitude of curing methods. Covering them all would be near impossible, and equally impractical. The following chemistry should be treated as representative of the broader process for a single cement, and not taken as a strict discussion of the precise chemistry taking place to produce any given concrete.

1.2.1 Portland Cement Hydration

In Portland cement, around 80% of the weight is due to two silicate compounds, tri-calcium silicate (C_3S) and di-calcium silicate (C_2S) (ASTM C185-15a, 2015). These hydrate to form the initial and long-term strength components for Portland based concretes. C_3S reacts more quickly with water, contributing to material strength within the first month, while C_2S takes much longer. Both go through a hydration reaction that results in calcium hydroxide and a calcium-silicate hydrate gel (C-S-H), the chemistry of which is shown in Equations 1 and 2 (Leung, 2001).



This C-S-H gel phase is what creates most of the structural integrity within concrete, binding together the aggregates, as it is rigid in nature. The precise structure of C-S-H is not currently known, though some information is generally agreed upon. The likely structure of the material is similar to that of Tobermorite, which is shown in Figure 1.

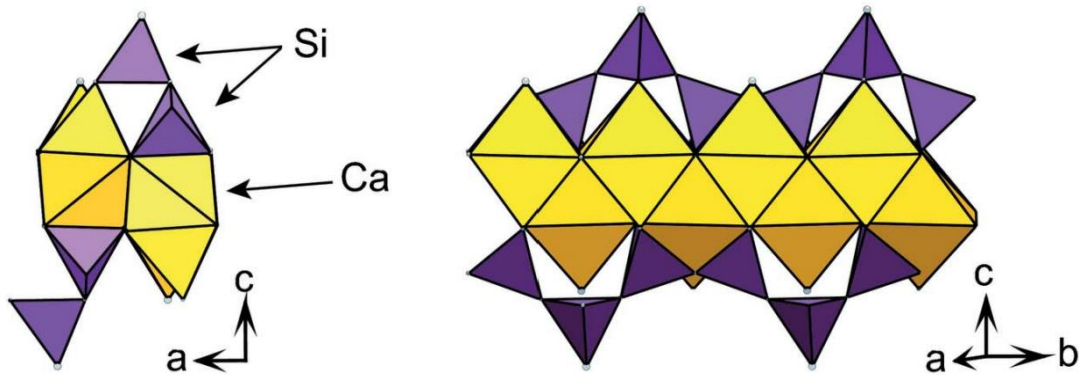
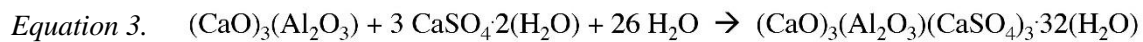


Figure 1. Tobermorite as viewed along a polysilicate chain, the structure of which is similar to C-S-H (Grangeon, Claret, Linard, & Chiaberge, 2013).

The silicates may comprise the majority of cement, but the presence of aluminate and ferrite in the cement drives the hydration reaction forward. Tri-calcium aluminate (C_3A) hydrates incredibly quickly, to the point of requiring a retarding agent like calcium sulfate dihydrate (gypsum) so that the entire concrete doesn't set prematurely. The reaction of these compounds is shown by Equation 3 (Hewlett, 2019).



This reaction produces a mineral known as ettringite, which has a columnar structure that entrains both water as well as sulfate ions. Figure 2 shows the physical structure of ettringite. The final hydration reaction occurs with tetracalcium aluminoferrite (C_4AF). It reacts similarly to C_3A , as it hydrates into ettringite with gypsum as a sulfate source, but it reacts significantly slower. The exact cause of this is not known, but it is speculated that the iron is less able to react than the aluminum due to lesser mobility in the cement paste (Barrow, 2010).

The progression of these reactions at their individual rates (differing by months) goes through several semi-discrete phases to take a cement powder hydrated with water to the final cured concrete. In the first ten minutes following the powder hydration, an amorphous gel and ettringite form from the hydration of the aluminum and iron phases in the presence of gypsum. After this, hydration slows down until around the three-hour mark. From hour three until hour twenty-four, around 30% of the cement hydrates, forming calcium hydroxide and C-S-H as per Equations 1 and 2. During this time, C-S-H forms in two distinct areas. C_3S forms C-S-H on the outside of the concrete, with C-S-H growing directly out of the ettringite columns which have migrated silicate

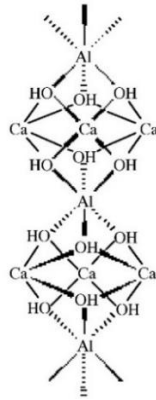


Figure 2. An ettringite column, containing octahedral aluminum, tetrahedral oxygen, and 8-coordinate calcium (Barrow, 2010).

from inside the paste. The balance of C-S-H in the material forms along the C₃S boundary with the hydration layer, which is often referred to as the ‘hydrating shell’ (Barrow, 2010).

At this point, the reactions slow down, remaining raw materials slowly continue to react and grow, and C-S-H fills the gap between the hydrating shell and the external C-S-H over the course of a few weeks. By then, the concrete has typically reached an effective strength to be used in various applications.

1.2.2 Magnesium Phosphate Cement Hydration

The reaction to produce magnesium phosphate cement (MPC) is considerably different from that of Portland, despite both being hydration driven. While the chemistry forming Portland is near exclusively a hydration, magnesium phosphates undergo a process that is more similar to an acid-base reaction with some hydration steps. To start, magnesium oxide (MgO) and potassium dihydrogen phosphate (KH₂PO₄) are hydrated. Potassium dihydrogen phosphate dissociates in three potential ways, all of which free a positive potassium ion, and two of which release free protons (H⁺) from the phosphate. Magnesium oxide hydrates into magnesium hydroxide (MgOH⁺), which then reacts with more water to form magnesium dihydroxide (Mg(OH)₂) and hydronium (H₃O⁺). The magnesium dihydroxide dissociates into Mg²⁺ and 2 OH⁻. The ionic magnesium bonds to water, and the reaction product of that bonds to the free phosphate ions, forming the final hydration reaction product of struvite-k, MgKPO₄·6H₂O. This mineral is a struvite analogue, hence

the name, which forms the basis for the strength of MPC. The reaction pathway for this process is shown in Equation 4, while the crystal structure of the final hydration product is shown in Figure 3.

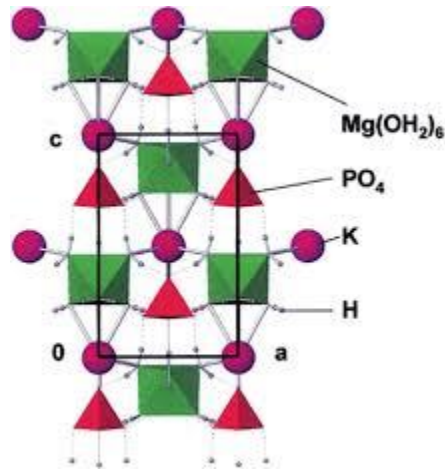
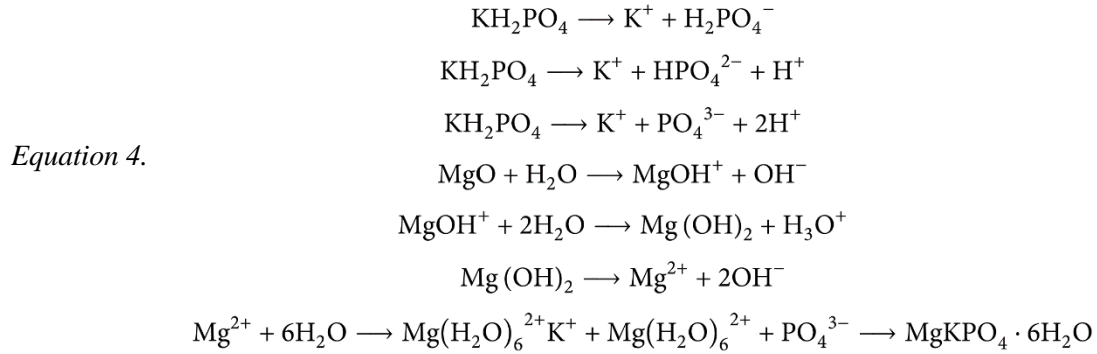


Figure 3. The mineral structure of struvite-k (Graeser, et al., 2008).

1.2.3 Microstructural Differences

The final hydration products are what contribute much of the structural differences between these two materials. The role of C-S-H in concrete is understood to be as a rigid matrix, often described as a “honeycomb” which contains aggregates of all size, macro- and micro-scale. An image of this structure can be seen in Figure 4a, taken using a Hitachi S3200N variable pressure scanning electron microscope at the Analytical Instrument Facility (AIF) at North Carolina State University. The equivalent material formed from magnesium phosphate hydration, struvite-k, is shown

alongside, in Figure 4b. Both images were taken at 1000x magnification using a Robinson backscatter detector.

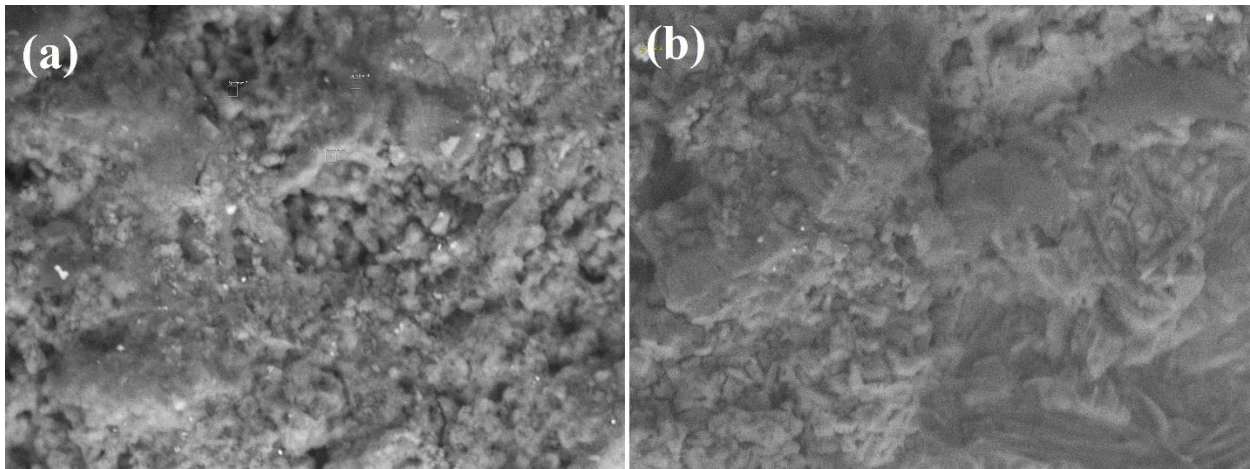


Figure 4. (a) C-S-H gel in Portland concrete, and (b) Struvite-k in MPC; at 1000x magnification.

C-S-H forms a more porous matrix than does struvite-k. This structural difference contributes to significant property differences, as will be illustrated by the remainder of this project. The higher density microstructure has the potential to contribute multiple property benefits to a concrete, such as reduced porosity, higher compressive strength, and increased density that results in better radiation attenuation properties (Baster, 1997). As all of these are attractive features for high- and low-level nuclear waste storage, it is easy to see why MPC are a candidate for study.

1.3 Concrete in Nuclear Waste Storage

1.3.1 HLW - Spent Fuel Pools

There are two ways in which spent nuclear fuel is primarily stored once it has been removed from a reactor. The first is in spent fuel pools, which are large artificially constructed pools of water in which fuel assemblies are deposited for up to twenty years to decay, cooling down in both thermal energy and in radioactivity (Alvarez, 2011). A representative image of a spent fuel pool is shown in Figure 5. These structures utilize a significant amount of reinforced concrete, as the structure which houses both the internal shielding liner and the racks for the spent fuel assemblies typically have a volume close to 400,000 gallons (National Research Council, 2006). Multiple studies have been done to evaluate the possible failure modes of a spent fuel pool including total seismic failure (Prassinis, et al., 1989) and various coolant loss scenarios (Ahn, Shin, & Kim, 2016). Failure of

the concrete structure was most prevalent in any seismic events, primarily through shear and bending failure. Fibrous concrete has been tested with both these failure modes, and for some beam sizes it was found that they improved upon nonfibrous materials (Noghabai, 2000).

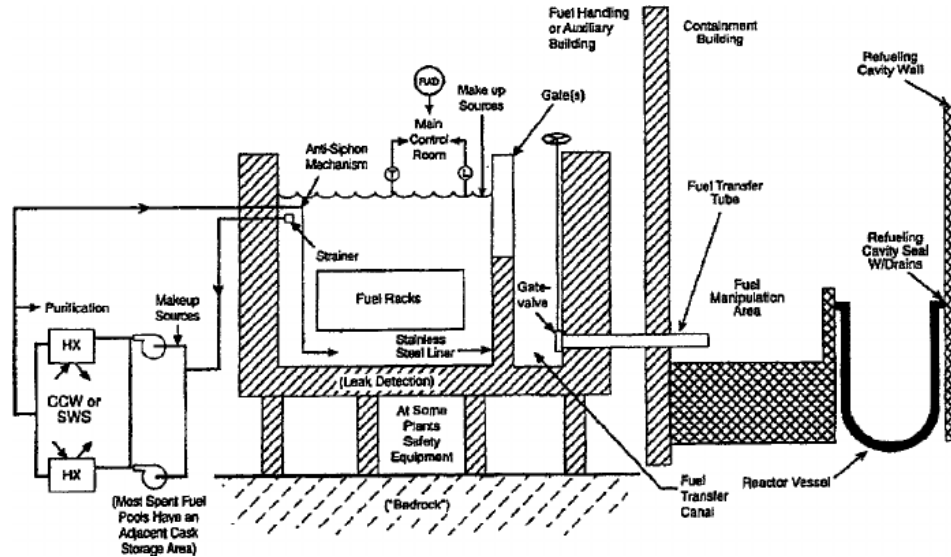


Figure 5. A spent fuel pool and transfer system for pressurized water reactors (NUREG- 1275 , 1997).

1.3.2 HLW - Dry Storage Casks

Spent fuel casks have a variety of designs, but they can be simplified to a few general structural components. The innermost part of the cask is the spent fuel assemblies. Once removed from the reactor, these assemblies are deposited in the pools, as mentioned above. They cool down for around six to ten years ideally, after which time they are intended to be moved into a fuel cask (Nuclear Regulatory Commission, 1987). The primary structure housing these assemblies is a steel cylinder that is sealed shut with bolts or welds and backfilled with an inert gas. Surrounding this steel cylinder is typically a large volume of concrete, referred to as an overpack. The thickness of these overpacks is usually around two feet in each direction, resulting in a final spent fuel cask close to 20 feet in height, and around 8 feet in diameter, weighing approximately 100 tons when loaded. The scale of these storage casks requires very meticulous transport and long-term storage. Figure 6 shows a representative dry storage cask, with part (a) illustrating the internal steel canister and (b) illustrating the canister within the overpack and lid.

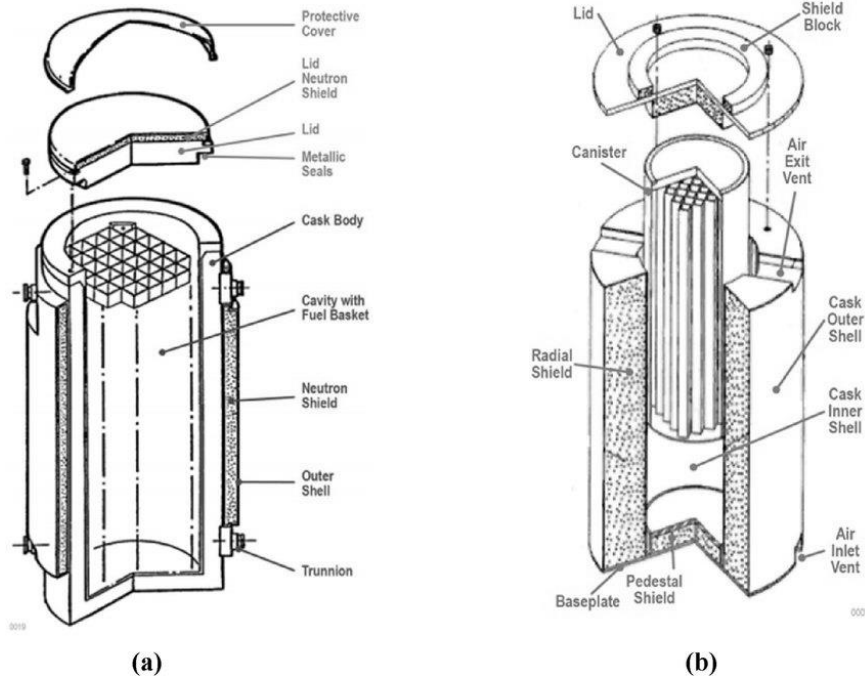


Figure 6. A vertical dry storage cask design, (a) the internal steel canister housing the spent fuel assemblies, and (b) the steel canister contained within the concrete overpack and lid (Li & Liu, 2016).

While it is desirable for these storage casks to be moved to a permanent facility, such as a deep geological repository like that planned for Yucca Mountain (Meyers, 2008), or that being currently undertaken by the Canadian Nuclear Safety Commission (Canadian Nuclear Safety Commission, 2019), no such facility is currently available, or even under construction in the United States of America. Consequently, dry storage casks are currently being stored either on-site at reactor facilities in a variety of vertical or horizontal vaults, or in offset Independent Spent Fuel Storage Installations (ISFSIs) (Fischer & Howe, 1999).

There is currently no alternative to the long-term storage of spent fuel casks in these locations and conditions. Casks stored this way have been projected to undergo cracking due to corrosion within the next 20 years (Wald, 2011). Materials improvements appear to be a necessity to remedy these issues within the political and economic constraints.

1.3.3 LLW - Medical Radiowaste Disposal

Radioactive waste from nuclear medicine comes in a variety of materials. The easiest to dispose of is all Tc-99m waste, as this isotope has such a short half-life that contaminated materials can be disposed of as radiation free after 48 hours of shielded storage. Glove and syringe waste that were used with other short-lived isotopes go through a similar process. Any material that was in

contact with longer-lived isotopes has to undergo a shielded decay for 2 months before being checked with a GM-counter and disposed of safely if no radiation is detected (Ravichandran, Binukumar, Sreeram, & Arunkumar, 2011).

While the materials used to administer radiative medicine have to be safely stored before disposal, there is also radioactivity present in the form of the patients' excreta. This presented a problem for many hospitals, as the radioactive waste streams were not always caught before the waste entered the plumbing, leading to some hospitals waste streams being rejected for treatment (Evdokimoff, Cash, Cardenas, & Buckley, 1994). Nowadays, patients who have undergone radioisotope injection in the form of tracers for FMRI and similar applications have to dispose of their waste in the isolation wards they are retained in, where it enters a waste delay tank to allow it to decay for 2 months before entering the sewage system (Khan, et al., 2010). Figure 7 shows a basic schematic for a delay tank system.

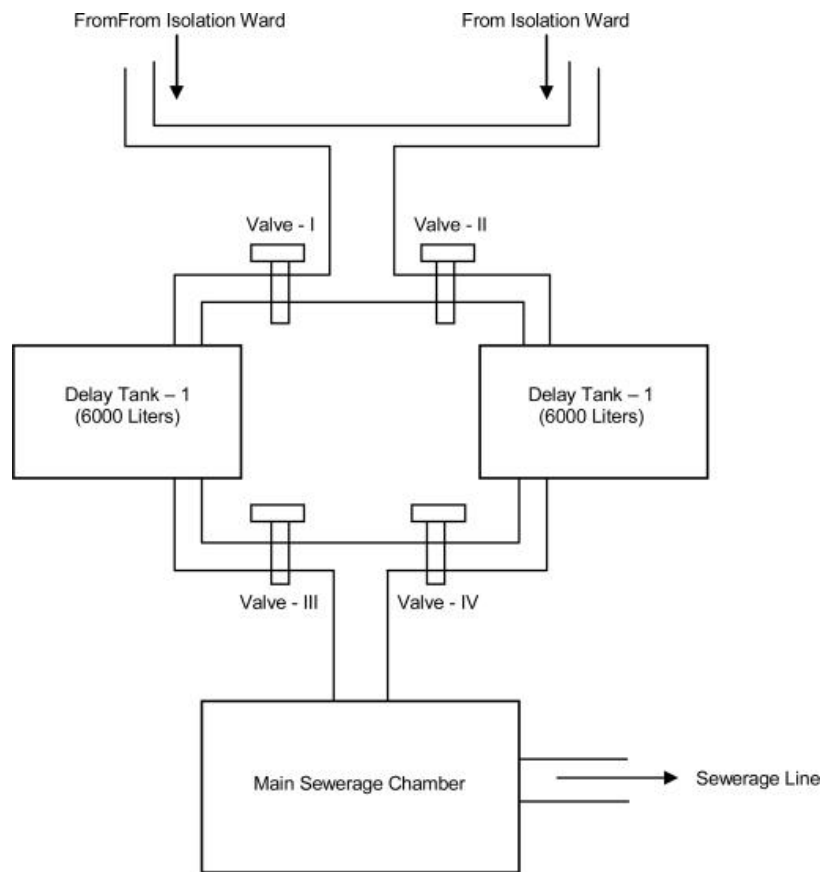


Figure 7. Dual delay tank system, to isolate for activity decay the excreta of two patients with active waste (Khan, et al., 2010).

Chapter 2. Project Motivation and Objectives

2.1 Technical Gaps in Nuclear Waste Storage

While there are many formulations of concrete hydrated from differing cement chemistries, more specific applications of the concrete products will be discussed next, namely that of nuclear waste storage. The most convenient place to start with a brief survey of nuclear waste storage as it relates to concrete materials research is with the most recent global survey on data gaps. The Review of Used Nuclear Fuel Storage and Transportation Technical Gap Analyses from 2012 will be the primary reference used for this topic, as it is the most recent release of data available (Used Fuel Disposition Campaign, 2012).

This technical gap analysis covers numerous data gaps in understanding as they relate to most aspects of nuclear waste storage. This project is focused on concrete, so the concrete sections of the gap analysis will be the only ones considered here. Each regulatory body for nuclear energy from several major countries contributed their reasoning and priority on the majority of these technical gaps, including the NRC. For each technical gap that the NRC considered high priority as they relate to concrete, a brief summary will be presented.

2.1.1 Corrosion of Embedded Steel

The first such technical gap is related to the corrosion of embedded steel in concrete. While most regulatory bodies consider this to be a medium or low priority technical gap due to the ease of monitoring such corrosion through techniques like ultrasonic emissions (Antonaci, 2013), the NRC assigned it a high priority in cases where such monitoring is not possible (Used Fuel Disposition Campaign, 2012). Their reasoning is based on the longevity of the passive layer within

most concretes. While concrete forms a pH between 8 and 13 depending on the time in the life cycle (as mentioned, cement paste reaches a pH of around 13 initially and slowly becomes more neutral as it cures, reaching a pH of around 8), this passivity can be lost through calcium hydroxide leaching to the environment. According to a study done in 2011 by Sindelar et al., it is likely that an overpack of traditional concrete will carbonate within 300 years through normal exposure, allowing corrosion of the reinforcing steel to initiate (Sindelar, et al., 2011). As this is not something that can be traditionally prepared for with monitoring due to the timescale, further advancements in materials technology are desired for this technical gap.

2.1.2 Thermal Degradation of Mechanical Properties and Dryout

As is it relatively easy to study, concrete dry-out is a well-understood technical space, with years of thorough research and results. It is known that temperatures above the vapor point of water cause bound water within the concrete to evaporate out, leaving a weakened physical structure behind (Naus, 2005). The remaining concrete is capable of being sufficiently rehydrated through rainwater or equivalent, so long term consequences are minimal (Farage & Galle, 2003). Since NUREG 1536 was released in 1997, standardized temperature limits have been considered for concrete. Normal conditions are considered to have temperatures at or below 150°F, local areas under normal conditions can reach 200°F, and accident conditions are considered to reach 350°F (Office of Nuclear Material Safety and Safeguards, 2010). Despite the well documented research surrounding thermal degradation of concrete, the NRC attributed a high priority to high-temperature thermal degradation up to 1000°C for short term heating on non-monitored concrete in accident scenarios (Used Fuel Disposition Campaign, 2012). They explain that “the effects of temperature on the properties of concrete have significant variability and are known to be dependent on the concrete chemistry and construction practices,” in a statement from 2012. For this reason, they do not consider the current data on thermal degradation of concrete sufficient. Additionally, this statement implies that each and every differing composition of concrete needs to be fully evaluated for the thermal behavior, as the chemistry changes between binders, with admixtures, and in a variety of methods mentioned in the previous chapter.

2.1.3 Coupled Mechanisms

This is a technical gap only considered by the US NRC, and it relates to the compound interaction of a variety of failure mechanisms. One provided example is how calcium hydroxide leaching can be accelerated by the evaporation of bound water, leading to both accelerated reinforcing steel corrosion and accelerated mechanical weakening. Any such pairing of mechanisms like leaching, carbonation, acid attack, and cracking that leads to loss of properties is considered a coupled mechanism by the NRC. They attribute high priority to any coupled mechanism studies as they relate to concrete that is not easily monitored. This is a consistent trend across these technical gaps the NRC considers that other regulatory bodies do not. It is convenient for experimental design to study coupled mechanisms with regards to thermal degradation, as the properties of a material after heating can be readily tested to observe the coupling of those two interactions.

2.2 Project Objectives

As materials improvements appear to be needed based on the NRC technical gaps and multiple reports illustrating dry cask failure within the century, let alone the failure of tunnels at the Hanford site (Bowman, 2019), this project seeks to characterize one such possible candidate. A fibrous magnesium phosphate cement was selected as the binder for this project, based on much of the reasoning discussed in Chapter 1. Fibrous concretes have isotropic tensile strength improvement over traditional concretes. MPC are both more environmentally friendly as they are not formed from the same process as Portland, and cure to a higher strength faster than any other concrete. Additionally, they have a denser microstructure which corresponds to improved particle entrainment and gamma attenuation.

2.2.1 Composition Optimization

The first goal of this project was to optimize an aggregate blend that would increase the gamma attenuation of this concrete without compromising structural properties. To that end, preliminary gamma attenuation experiments were performed on the base MPC and compared to that of a similarly manufactured Portland concrete sample. The results of this were compared to

compressive strength data, as well as product workability based on experience from the manufacturer who assisted in the initial optimization. With that information considered, the composition for further testing was determined.

2.2.2 Gamma Attenuation Properties

The second goal of the project was to determine the gamma attenuation of the potential aggregate compositions of concrete. To meet this objective, a spectrum composed of gamma rays somewhat similar in relative energy levels to that of spent nuclear fuel was acquired (Vaccaro, et al., 2017). While there are multiple possible applications for an effective shielding MPC, the design choice to target a spent fuel spectrum was made due to the complexity of that type of source. If a shielding material can effectively shield HLW, it can shield any and all of the gamma emitters found in LLW. The initial composition optimization spectrum was formed using the following isotopes: Ba-133, with a primary peak at 356 keV, Cs-137 with a primary peak at 662 keV, and Co-60 with major peaks at 1170 and 1330 keV. The majority of the experimental setup remained consistent between the initial composition optimization attenuation experiments and the more rigorous aggregate composition attenuation experiments. The main difference was the introduction of two more sources to better capture the low energy gamma range, as much of the radiation emitted by both nuclear medicine radioisotopes (KAERI) and spent nuclear fuel is below 356 keV in energy. Cd-109 and Co-57 were added to the source list, and their respective primary peaks at 88 keV and 122 keV were added to the list used to calculate the linear attenuation coefficient.

2.2.3 Corrosion/Erosion Properties

Concrete corrosion is not a largely relevant metric, but the ability for concrete to resist mass loss and acid attack due to corrosive/erosive effects is one way to reduce the corrosion of embedded reinforcing steel (Elsener, 2013), which is considered a high priority technical gap by the NRC in many cases. For this reason, understanding the behavior of aggregate MPC in acidic and erosive conditions was the next objective of this project. There are multiple methods of determining the impact of acid attack on a concrete, as well as mass loss attributable to erosive effects. While methods such as electrochemical accelerated corrosion are beneficial for extrapolating long-time

corrosion behavior of a material, they are difficult to employ in nonconductive samples, and don't yield as precise results (González, Molina, Escudero, & Andrade, 1985). A long-term exposure using a circulator and acidic or brine solution can deliver more useful data, as the raw mass change due to corrosive and erosive effects is captured over the course of months, and the effects of prolonged acid attack are more likely to be of concern than electrochemical corrosivity.

2.2.4 Mechanical Properties

There are several important mechanical properties for concrete, but the two that will be discussed here are density and compressive strength. These each directly relate to the efficacy of concrete as a construction and shielding material for high- and low-level nuclear waste. The compressive strength dictates the volume of material needed to ensure physical integrity of the structure, and the density directly relates to the gamma shielding capabilities (Parker, Smith, & Taylor, 1984), as well as influencing the allowed volume of concrete in multiple storage applications. Access to machines for rigorous stress-strain evaluation was not able to be obtained during the course of this investigation, so ultimate compressive force is the metric used to discuss this property. As concrete is not a ductile material, and MPC and other high strength concretes primarily undergo peak load failure in methods typical with brittle materials, ultimate compressive force is an acceptable surrogate property for discussion (Kotsovos, 1984).

2.2.5 Outgas Properties

To immobilize nuclear waste, volatile and radioactive material like tritiated water or fission fragment sludges can be mixed into concrete in the curing process, either with the concrete formers and aggregates before water is added or as a part of the water itself (Spence, Gilliam, Mattus, & Mattus, 1999). This is a very efficient way to contain radioactive materials that are difficult to store due to their volatility or extreme activity. Troubles arise when the bound water within the concrete is able to vaporize and exit the material; such scenarios are referred to as 'outgassing' or 'offgassing.' Due to the potential for heavy aggregate MPC to be an effective waste immobilization material based on the microstructural properties, mass loss through heating was investigated.

2.2.6 Thermal Properties

Careful management of the temperature profiles of both the spent nuclear fuel casks themselves as well as the honeycomb housing structure for long-term storage is done to prevent accidents. Decay heat presents a thermal load for concrete within a spent fuel casks, with average temperatures near the air gap exceeding 100 °C (Koyanbayev, Skakov, Ganovichev, Martynenko, & Sitnikov, 2019). Maintaining material properties at elevated temperatures is of concern for hydrated materials like concrete, and the specific effects of aggregates modify these properties as well as the underlying degradation chemistry (William, Rhee, & Xi, 2005). For these reasons, a thorough investigation of the degradation mechanisms and any material property changes that occurred as a result of degradation was performed.

Chapter 3. Concrete Composition Optimization

3.1 Introduction

Both aggregate material and aggregate size can affect the final properties of cured concrete. When improving the linear attenuation coefficient of a material, most of the aggregates seen in literature are compounds with relatively high atomic weight (high Z) compared to those found in normal concrete like Portland (Kaplan, 1989) (Kharita, Takeyeddin, Alnassar, & Yousef, 2008) (Akkurt, Akyildirim, Mavi, Kilincarslan, & Basyigit, 2010) (Maslehuddin, Naqvi, Ibrahim, & Kalakada, 2013). One such paper tested barite, magnetite, goethite, serpentine, silica fume, and ground granulated blast-furnace-slag to attempt to create a ‘high-performance heavy density concrete’ (Ouda, 2015). This project intended to create a similar material, so several of these aggregates were tested in the initial optimization process. In addition to barite and magnetite, fly ash was chosen as another aggregate (Amritphale, Anshul, Chandra, & Ramakrishnan, 2007), with the final aggregate tested being lead.

Lead has a high atomic weight compared to the other aggregate choices, but such low physical strength that it is often an unusable candidate material. It was selected for inclusion based on the superior strength characteristics of MPC. Figure 8 shows a series of sample compositions produced for initial aggregate optimization. All percentages discussed hereafter will refer to mass percent of the dry mixture, blended with both cement and aggregates, before hydration. Magnetite and lead were anticipated to be the most useful aggregates, so aggregate concentrations of 10-50% in 10% increments were made for initial testing. Fly Ash was added at a 15% concentration to a series of samples, and Barite at 10, 15, and 30% to round out the composition optimization sample set. Aggregate size was selected on the order of 1 mm, with the exception of lead introduced in powder

form, to ensure the best homogeneity possible, imparting consistent and diffuse radiation attenuation improvement.

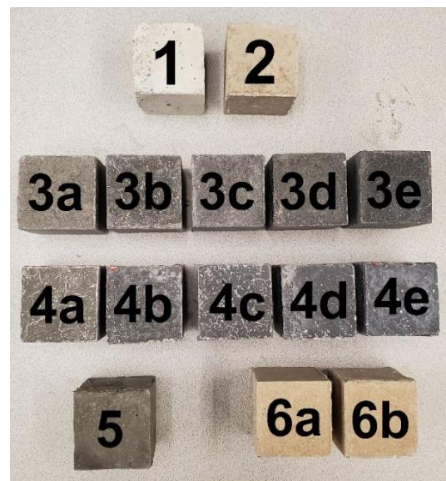


Figure 8. Samples used to optimize MPC composition. (1) Portland, (2) MPC Base, (3a-e) MPC Base w/ 10-50% Magnetite, (4a-e) MPC Base w/ 10-50% Lead, (5) MPC Base w/ 15% Fly Ash, (6a) MPC Base w/ 10% Barite, (6b) MPC Base w/ 30% Barite.

3.2 Methods

The first goal of this project was to optimize an aggregate blend that would increase the gamma attenuation of the chosen MPC without compromising structural properties. To that end, gamma attenuation experiments were performed on the base MPC and compared to that of a similarly manufactured Portland concrete sample. The results of this were compared to compressive strength data, as well as product workability based on experience from the manufacturer. With that information considered, the composition for further testing was determined.

There are two primary production methods used in this experiment. The first was the production of the control samples of ordinary Portland concrete. Off-the-shelf bags were purchased from a home supply store chain, with all large particle aggregates (5mm and larger) filtered out with a mesh, leaving the base Portland cement mixture. This was combined with 18% water, poured into 5 cm side length cube molds, and allowed to cure for twenty-eight days. All further Portland samples were produced using this method, with a select portion only poured to half the height of the mold to create half-height cubes 2.5 cm tall with a 5 cm square base for some experiments with size constraints.

The MPC was produced using the manufacturer's magnesium phosphate cement binder. This cement was then mixed with 15-18% water and left to cure for twenty-eight days, or further mixed with whatever aggregate materials were needed for the testing compositions. For the aggregate samples, the same proportion of water was added after aggregate blending, and they too were left to cure for twenty-eight days. These samples were produced using the same molds as Portland, resulting in 5 cm cubes for the majority with some half-height samples as mentioned above.

Further sample processing occurred for several of the analytical instruments used in Chapter 9 which require differing geometries of structure. For x-ray powder diffraction and x-ray photoelectron spectroscopy, powders were needed. To that end, small fragments were sheared off the larger samples and ground to a fine powder in a mortar and pestle. This powder had a grain size no larger than 1 mm.

Methods such as Raman spectroscopy and secondary ion mass spectroscopy required small cubic samples no larger than 1 cm in side length. These were machined to shape from the larger as-manufactured cubes using a diamond blade water cooled saw. This presented one of the larger sources of potential error, as part of the spectroscopic process was to determine the composition of dehydrated samples, but the only way to create samples to fit in the machines was with this water-cooled saw. While samples were cut quickly and re-dried as soon as they were removed from the saw, it is possible that the water cooling partially rehydrated them, introducing error into the final measurement.

3.3 Results

3.3.1 Attenuation

Once the initial series of concrete samples were finished curing, attenuation testing was able to begin. The specific methods of this testing will be discussed in further detail in Chapter 4. The linear attenuation coefficient for each discrete energy was calculated, then plotted and compared, the results of which are presented in Figure 9. Each subplot compares Portland and MPC Base samples to the various aggregate samples tested.

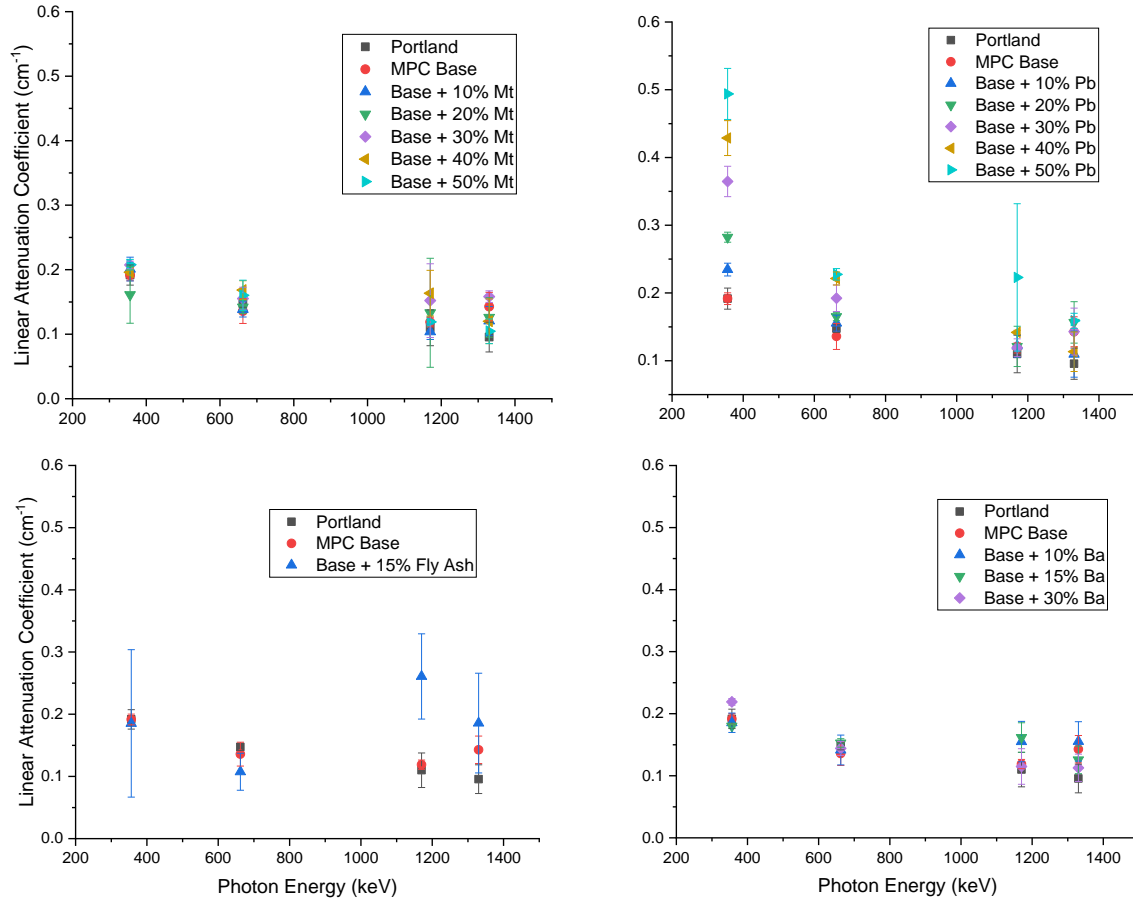


Figure 9. The linear attenuation coefficient of varying aggregate MPC over the tested energy spectrum.

As can be seen from the subplots within Figure 9, one material had a significantly higher impact on the linear attenuation coefficient than the others. Lead additive as low as 10% by mass resulted in more increase to the linear attenuation coefficient than any other aggregate at any tested concentration. This is not an unexpected result, as the atomic weights of the other aggregates are all considerably lower than lead ($Z = 86$), the next highest being the barium present in barite ($Z = 56$). Lead is not commonly used in concrete as an aggregate due to the loss of structural properties it causes, though when used in the form of lead shot it creates a concrete with very high density, approaching 9000 kg/m^3 (Collins, 2019). Based on the goal of improving the radiation attenuation of MPC, lead distinguished itself as an aggregate, but it is important to consider the loss of strength that such aggregate likely caused. To this end, compression testing was performed.

3.3.2 Compressive Strength

As the radiation attenuation improvement caused by lead was superior to that of the other samples using high-Z materials (namely barite and fly ash), those aggregate samples were omitted from compression testing. Based on the working properties of the solely lead aggregate concretes, they were ruled out as candidates due to the thin pour properties. Magnetite alone did not yield relevant linear attenuation coefficient improvement but contributed significant working properties. For these reasons, two hybrid compositions were tested using magnetite and lead to attempt to capture the beneficial properties of both aggregates. The first contained 20% by mass powdered lead and 20% by mass fine aggregate magnetite, referred to as MPC 2020. The second contained 30% by mass of the same lead and 30% by mass of the same magnetite, referred to as MPC 3030. Initial ultimate compressive strength experiments were performed at the production facility by the manufacturer for the purposes of verifying the intended testing compositions' function and physical stability. The plant manager used a Forney Compression Machine, taking measurements twenty-eight days after cure for all samples. Table 1 shows the measured ultimate compressive strength of each of the aggregate MPC alongside Portland and MPC Base as control samples.

Table 1. Ultimate compressive strength as measured by the manufacturer for each of the intended testing compositions.

Portland	MPC Base	MPC 2020	MPC 3030
20 MPa	41 MPa	45 MPa	17 MPa

3.4 Conclusion

Based on the initial gamma attenuation experiments, it was clear that lead was the most important aggregate to reaching the desired goal of an improved shielding MPC. Barite was not able to match the linear attenuation, or the mass attenuation, imparted by lead powder and so was ruled out as a candidate for this application. Fly ash, while the study of many other investigations, held more weight as a primary concrete former and less so as a shielding aggregate when a high-Z option such as lead was available and so was also ruled out as a candidate for this application. Magnetite did no more than barite or fly ash with regards to the gamma attenuation, but was sufficiently capable of replacing magnesium phosphate concrete in the cement mix as a cost reducer, while

giving the cement paste more viscosity, allowing it to flow and self-level. For these reasons, magnetite was chosen as a candidate aggregate. Lead, as mentioned prior, is significantly higher in atomic weight than any of the other materials tested and imparted the highest gamma attenuation improvement, and so was chosen as the second candidate aggregate.

Lead and magnetite were added to the magnesium phosphate cement blend in individual mass percentages of 20 and 30, resulting in the two candidate aggregate MPC for this investigation. MPC 2020 showed the highest ultimate compressive strength based on initial testing done by the manufacturer, at 45 MPa, more than double that of the tested Portland sample. MPC 3030 had the lowest ultimate compressive strength at only 17 MPa, though within normal ranges for ordinary Portland concrete, and sufficiently capable of maintaining its own structure and bearing meaningful loads. This composition optimization provided the final set of tested samples for the duration of the investigation, with MPC 2020 and MPC 3030 being compared to the control samples of ordinary Portland concrete and MPC Base.

Chapter 4. Gamma Attenuation Properties

4.1 Introduction

Gamma rays are one of several kinds of radiation that are emitted from the nuclear decay of radioactive waste. Other common forms include alpha particles (a helium nucleus, comprised of two neutrons and two protons stripped of their electrons), beta particles (electrons or positrons), and neutrons (Nuclear Regulatory Commission, 2018), which are all considerably easier to shield with relatively small widths of materials. It may be noted here that this is not an exhaustive list of the forms of radiation. One way to consider the ease of shielding radiation is through a value known as the mean free path. When a photon or particle from radioactive decay enters a material, it can interact in multiple ways, losing some or all of the inherent energy at each such interaction. The average distance between interactions is defined as the mean free path. Table 2 shows some representative mean free paths for each of the mentioned forms of radiation in common materials. The energy considered for each form of radiation in this table is noted, due to the inherent energy dependence of radiation attenuation.

Table 2. Average mean free paths of typical energy radiation in common materials (Mattingly, 2020).

Material	5 MeV Alpha Particle	1 MeV Beta Particle	1 MeV Neutron	1 MeV Gamma Ray
Air (STP)	0.035 m	0.46 m	54 m	121 m
Water	0.00004 m	0.00044 m	0.018 m	0.141 m
Lead	~	0.000052 m	0.060 m	0.012 m

The radiation present in spent nuclear fuel, radioactive sludge and salt, and nuclear medical waste all come from distinct radioisotopes with differing intensities and forms of radioactive decay. Despite this, it can be seen from Table 2 that for each waste form, the radiation with the highest probability of penetrating shielding materials are any emitted gamma rays. Without getting into details, this is due to their lack of both mass and charge, as gamma rays are photons while all other

forms of radiation are physical particles like leptons or hadrons. Similarly, the distinction between a neutron or gamma and an alpha or beta particle is the lack of charge, which also decreases the probability of interaction (Shultis & Faw, 1996). Since a material that can sufficiently shield gamma rays is similarly capable of shielding all other forms of radiation, gamma rays were the primary form of radioactive decay studied in this experiment.

These photons interact with matter in three distinct ways that are each dominant in a different energy regime. A summary of this energy dependence is shown in Figure 10. At low energies, typically between 0 and 150 keV, the photoelectric effect is the most common form of photon interaction. In this interaction, a photon traveling through a physical medium at low energies becomes absorbed by an orbital electron. All of the kinetic energy of movement the photon held is imparted to the electron, which is then ejected from the orbital and moves away from the atom.

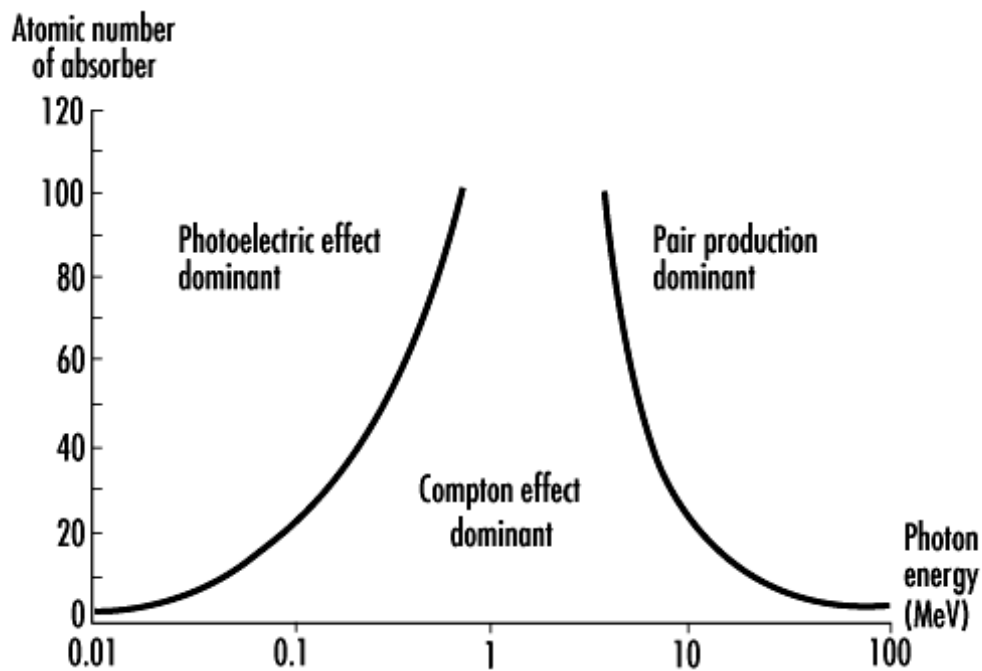


Figure 10. The dominance of photon interactions at varying energies in varying materials (Stellman, 2012).

In the intermediate energy regime, typically between 150 keV and 3 MeV, the Compton effect dominates. In this form of interaction, a photon will become incident to an electron similar to the photoelectric effect. Due to the higher energy of the incident photon, not all of the energy can be

absorbed by the electron, which leads to a scattering interaction where the photon will “knock off” the electron, ejecting the electron and itself leaving with some portion of the initial energy.

Above 3 MeV, but strictly beginning at no lower than 1.022 MeV, pair production is the dominant form in interaction. When a photon has at least two electron rest masses of energy (1.022 MeV) and passes through the electric field generated by an atom, it can undergo pair production and spontaneously split into an electron-positron pair which move in opposite directions with half of the photon’s energy each.

In most industry applications, shielding these photons requires large quantities of concrete or thick plates of lead to reduce the gamma rays penetrating the shield to a safe fraction of the original source. For dry-storage casks of spent nuclear fuel, the concrete overpack surrounding the steel canister is typically in excess of 60 cm (Nuclear Regulatory Commission, 2011). This is due to the physics behind the attenuation of gamma rays; Equation 5 shows the canonical equation governing this attenuation.

Equation 5.
$$I(x) = I_0 e^{-\mu x}$$

In this equation, $I(x)$ refers to the intensity of the shielded radiation counted by a detector (cts), I_0 is initial unshielded intensity of the source (cts), x is the thickness of the shield used (cm), and μ is the linear attenuation coefficient (cm^{-1}) which is a measure of the ability for a material to attenuate. This linear attenuation coefficient is the primary parameter of interest in gamma ray attenuation for this project, as it will be used to compare the various shielding materials on their efficacy at the task.

The linear attenuation coefficient can also be used to calculate a variety of other properties that help show data in potentially more meaningful ways. It is indirectly proportional to the mean free path, which is the parameter shown in Table 2 to compare the thickness of shielding materials. It is also directly proportional to the mass attenuation coefficient, which is effectively a density normalized attenuation coefficient. Equation 6 shows the mean free path, as l (cm). The mass attenuation coefficient is simply the linear attenuation coefficient divided by the density and will be shown as μ/ρ (cm^2/g).

Equation 6.
$$l = \frac{1}{\mu}$$

4.2 Methods

Since the first goal of the project is to optimize the composition of the MPC for gamma attenuation, the second goal of the project is to determine the gamma attenuation of the concrete. The gamma spectra output by medical radioisotopes is quite precise and can be readily determined based on the isotopes in question. In general, they fall below 300 keV in energy. The spectra generated from weapons production waste and by spent nuclear fuel are much more complex, and range in energy from the low 100s keV up past 1500 MeV. Based on this, it is reasonable to conclude that a material that can shield one of these HLW forms can also sufficiently shield LLW. A spectrum composed of gamma rays somewhat similar in relative energy levels to that of spent nuclear fuel was acquired to apply that concept. The initial composition optimization spectrum was formed using the following isotopes: Ba-133, with a primary peak at 356 keV, Cs-137 with a primary peak at 662 keV, and Co-60 with major peaks at 1170 and 1330 keV. The majority of the experimental setup remained consistent between the initial composition optimization attenuation experiments and the more rigorous product composition attenuation experiments.

The main difference was the introduction of two more sources to better capture the low energy gamma range, as much of the radiation coming from spent nuclear fuel is below 356 keV in energy. To that end, Cd-109 and Co-57 were added to the source list, and their respective primary peaks at 88 keV and 122 keV were added to the list used to calculate the linear attenuation coefficient. In both cases, the sources were positioned on the base of a ring stand, with partial collimation from lead bricks surrounding them. 15 cm above the base of the ring stand, a ring clamp was positioned that held the concrete samples during exposure. 30 cm above that ring clamp was where the detector window was positioned, held in place by a clamp. An Ortec NaI(Tl) detector was used, attached to an Ortec DigiBase for processing, and interpreted using Maestro software. The experimental setup is depicted in Figure 11.

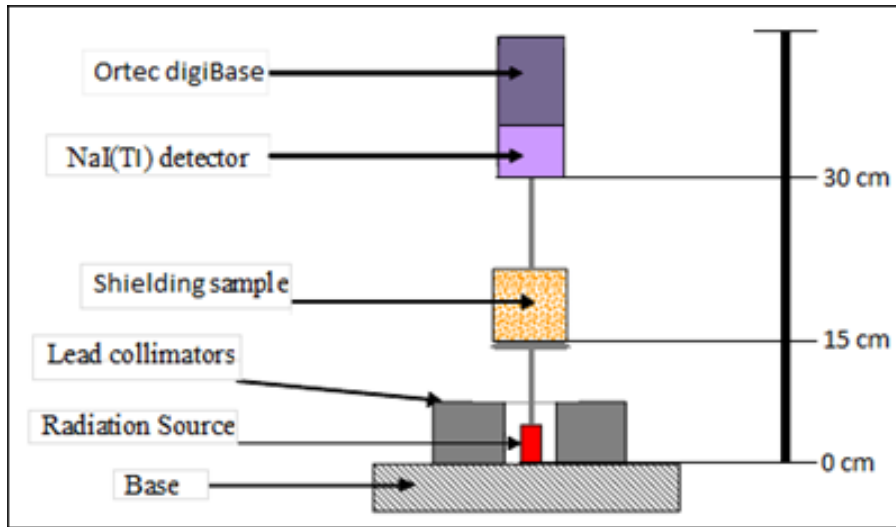


Figure 11. The experimental setup for gamma ray attenuation.

Figure 12 compares the spectrum produced by the chosen sources to the spent fuel spectrum of a PWR spent fuel assembly after five years of cooling, which is the average length of time a fuel assembly will spend in a pool before being moved into a dry cask for long-term storage (Alvarez, 2011).

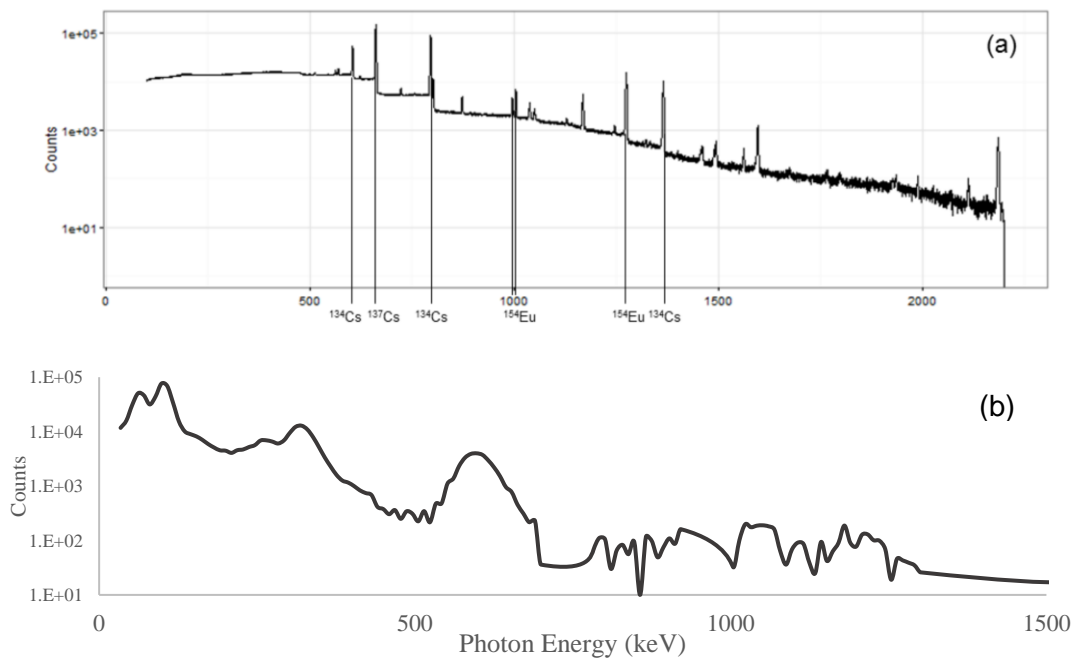


Figure 12. (a) the spectrum produced by irradiated PWR spent fuel assemblies after 5.2 years cooling time (Vaccaro, et al., 2017), and (b) the spectrum produced by the selected isotopes for attenuation testing.

Data was collected with no sources or shielding sample present for one hour during each day of experimentation. This background data was removed from all subsequent runs based on the day they were taken through simple channel-based subtraction. After the background data was collected, the sources were positioned based on the description above, and a spectrum using only the sources was collected. This provided the first piece of information needed to determine the linear attenuation coefficient of the material, the unshielded intensity. Following the source spectrum, data was collected with each of the shielding samples present for the same duration, resulting in the various shielded intensities. In order to account for batch inconsistency, ten different samples were tested for each composition, spread across two different pours of concrete. Once all spectra had been collected and corrected for background, the location of the known primary peaks were used to perform a basic linear regression to verify the energy value of each channel. The counts at each such peak were then isolated and used with physical data to solve Equation 5 for the linear attenuation coefficient.

4.3 Results

Linear attenuation coefficients were the first calculated parameters, and so will be first discussed. Figure 13 shows the average linear attenuation coefficients at each peak energy level for the four chosen samples, with Table 3 showing the same data in tabular form.

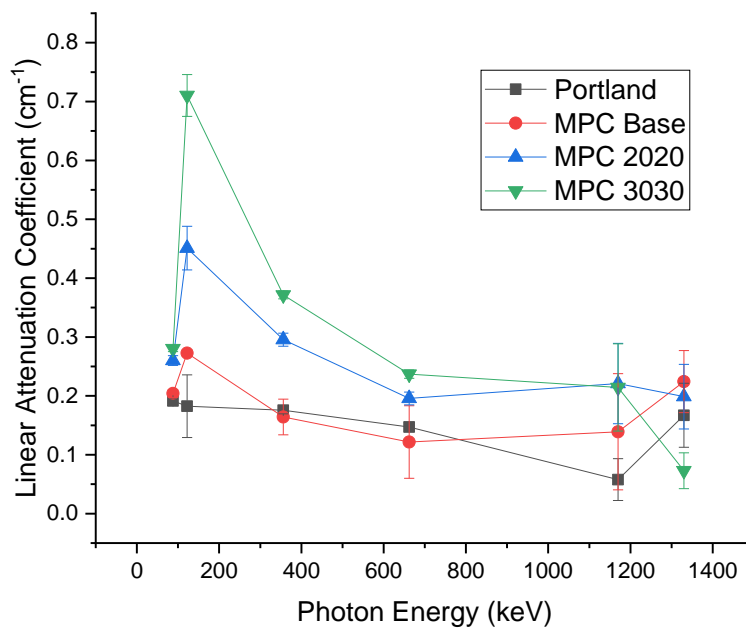


Figure 13. The linear attenuation coefficient for each sample over a wide range of energy levels.

Table 3. The linear attenuation coefficient in cm^{-1} for each sample over a wide range of energy levels.

Material/Energy	88 keV	122 keV	356 keV	662 keV	1170 keV	1330 keV
Portland	.1915	.1826	.1757	.1471	.0578	.1671
MPC Base	.2041	.2727	.1642	.1216	.1390	.2242
MPC 2020	.2601	.4510	.2955	.1957	.2209	.1987
MPC 3030	.2802	.7104	.3716	.2370	.2143	.0729

Error bars for Figure 13 have been set to show one standard deviation away from the mean value. In general, these results are consistent with the initial testing. The presence of 30% lead by mass contributed to a linear attenuation coefficient of 0.36 cm^{-1} at 356 keV, which is comparable to that of the 30% lead 30% magnetite sample shown here with a value of 0.37 cm^{-1} at the same peak. Similar trends are maintained for the 20% lead aggregate samples. Both mixed aggregate samples performed better than Portland or MPC Base. When averaged over the energies tested, this increase in the linear attenuation coefficient corresponded to 76% for MPC 2020 and 104% for MPC 3030 when compared to Portland.

While this information shows a clear improvement on the part of both aggregate MPC, the weight of the material matters with regards to industry application. If weight did not matter, lead could simply be added as a thick slab within larger concrete pours and the materials improvement would be unnecessary. For this reason, comparing the mass attenuation coefficient is also of interest. Figure 14 and Table 4 replicate the information of the prior two, showing the mass attenuation coefficient of these materials.

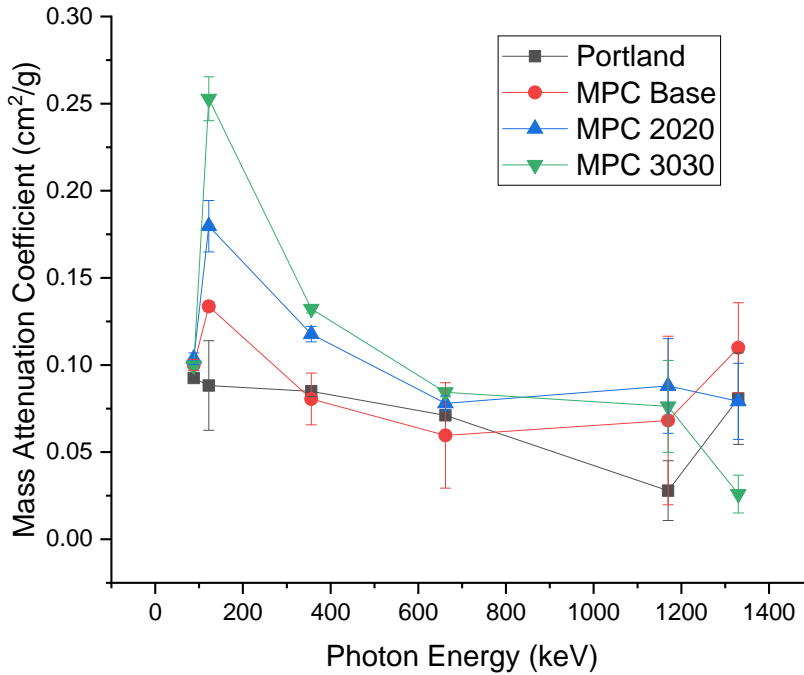


Figure 14. The mass attenuation coefficient for each sample over a wide range of energy levels.

Table 4. The mass attenuation coefficient in cm²/g for each sample over a wide range of energy levels.

Material/Energy	88 keV	122 keV	356 keV	662 keV	1170 keV	1330 keV
Portland	.0925	.0882	.0849	.0711	.0279	.0807
MPC Base	.1001	.1337	.0805	.0596	.0681	.1099
MPC 2020	.1036	.1797	.1177	.0780	.0880	.0792
MPC 3030	.0997	.2528	.1322	.0843	.0763	.0259

The general trends present in the linear attenuation hold true for that of mass attenuation. MPC 3030 maintains the highest attenuation at midrange energy levels, between 122 keV and 662 keV, with MPC 2020 producing consistently similar results between 88 keV and 1170 keV. These two materials do show closer attenuation coefficients when normalized for density, indicating that MPC 2020 may overall be a more effective material for general shielding efficacy. At higher energies, the aggregate samples show less attenuation than the nonaggregate samples, indicating the possibility of them being weaker shields for higher energy gamma rays. Based on this, it can be concluded that the linear attenuation coefficient is sufficient to discuss these materials shielding capability trends for the duration of the project.

Another way to compare these materials based on the attenuation of gamma rays is through the tenth-value layer. This is another use of the linear attenuation coefficient, as a means of describing the thickness of material needed to reduce the intensity of incident radiation to one-tenth the starting value. Table 5 shows the tenth-value layer of the four concretes using a peak-averaged linear attenuation coefficient.

Table 5. The tenth-value layer in cm for each concrete based on a peak-averaged linear attenuation coefficient.

Portland	MPC Base	MPC 2020	MPC 3030
14.99	12.27	8.52	7.32

This again highlighted the distinction between aggregate and non-aggregate samples. MPC 3030 required a full half the thickness of Portland, which is a stark difference in shielding capacity. The two materials were within the same working strength of each other based on initial compressive strength testing, so the aggregate MPC being capable of reducing the necessary shielding thickness by half is a nearly direct improvement based on discussed parameters.

4.3.1 Impact of Cure Time

To determine if the concrete curing longer than the 28-day standard impacted the linear attenuation coefficient, samples were tested at nine months after the initial cure began. Chapter 1 showed how Portland hydration can take months to reach reaction completion, and while magnesium phosphate concrete cures to working strength far faster, the internal aggregate migration can still take longer than the first month. Figure 15 shows the linear attenuation coefficients over the same energy spectrum of MPC Base, MPC 2020, and MPC 3030 at one- and nine-months post cure compared to Portland. The Portland was tested at nine-months post cure, but values did not deviate so the data points were omitted for clarity.

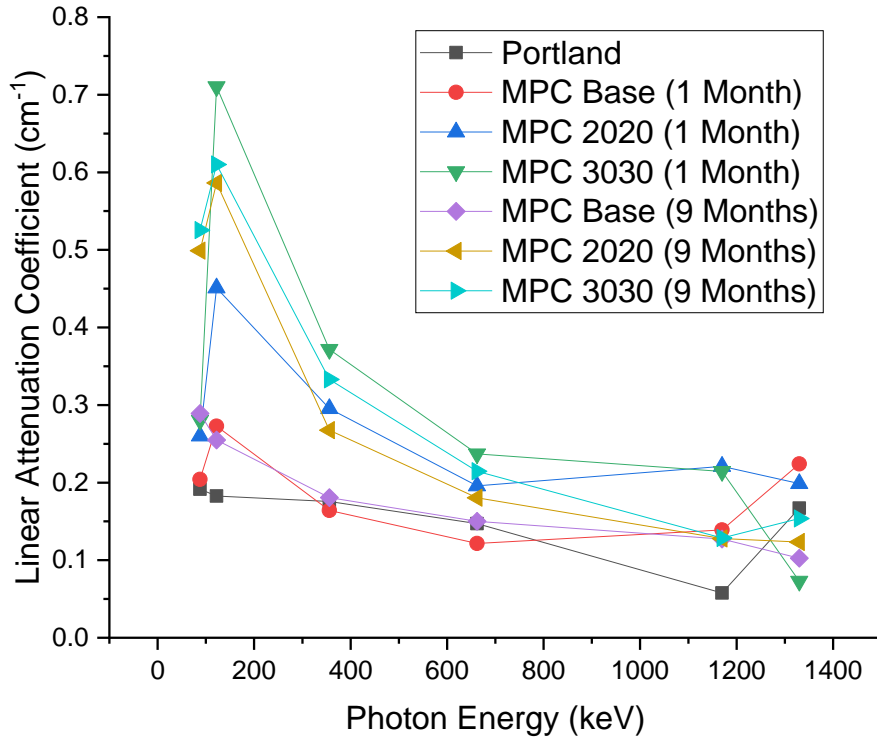


Figure 15. The linear attenuation coefficient of each sample over the energy spectrum at one- and nine-months post cure for MPC materials compared to Portland.

For each MPC, the average of these linear attenuation values does improve from one- to nine-months post cure. For MPC 3030 specifically it is entirely due to the increase at 88 keV, as the nine-months post cure sample does show a decrease in the linear attenuation coefficient at all other energy levels, but the increase at 88 keV is sufficiently large to result in a net increase. Both other samples improve at nearly all energy levels in addition to representing an average increase. It is speculated that this is due to the internal migration of aggregates throughout the material. As the diffuse lead powder can be attributed responsibility for nearly 100% of the gamma attenuation imparted to MPC 2020 and MPC 3030, the homogeneity of lead within the sample would account for variations in gamma attenuation over time. The samples tested at one-month post cure were likely exposed with somewhat less homogenized lead and thus less consistent attenuation within a single sample. Testing sufficiently far after the hydration would allow a more consistent and higher level of gamma attenuation. This homogeneity was verified through nano-computed x-ray tomography. Figure 16 shows two images taken using a Zeiss Xradia 510 Versa 3D X-Ray Tomography System at 140 kV and 10W, reconstructed using Dragonfly Pro.

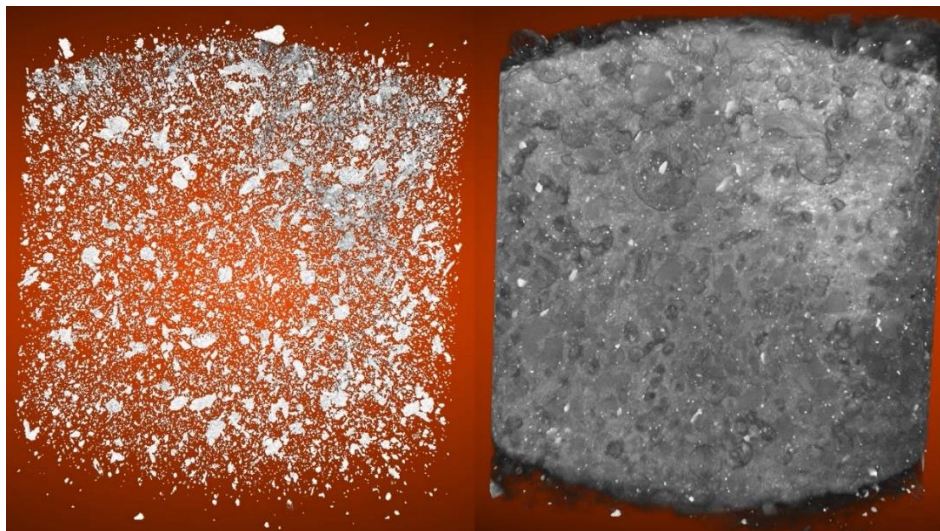


Figure 16. Left: the high-density aggregate (lead/magnetite) within MPC 2020. Right: the same image without the low-density filter.

As can be seen, there is even distribution of the somewhat irregularly shaped particles of magnetite and finer powdered lead within this MPC 2020 sample. This was taken 9 months after cure to verify the homogeneity of the sample. Similar images were unable to be taken prior to this time due to the lack of sufficiently penetrative x-ray systems in the region.

4.4 Conclusion

When comparing the linear attenuation coefficients, MPC 3030 stood out as a far superior shielding material to the others. This was backed up by MPC 3030 maintaining the highest mass attenuation coefficient as well, which is effectively the density normalized version of the linear attenuation coefficient. Comparison of the tenth-value layer shows that MPC 3030 required less than half the material to shield incident gamma radiation to one-tenth the initial level when compared to Portland. While MPC 2020 did not have quite as high a shielding capacity as did MPC 3030, it was still a significant improvement over the standard Portland across all metrics as well.

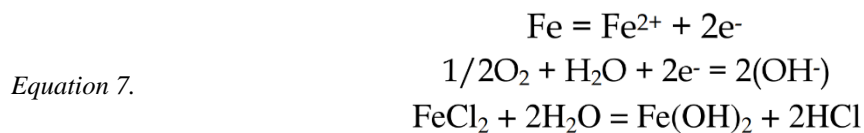
As the attenuation of gamma rays is only one facet of comparing materials for nuclear waste storage, no strict conclusions can be drawn until all properties are discussed, and so each subsequent section will supplement the prior conclusions as new data is discussed.

Chapter 5. Corrosion/Erosion Properties

5.1 Introduction

When corrosion is discussed with regards to concrete, the direct corrosion of concrete is never the primary topic. Concrete does not undergo meaningful corrosion, with the degradation processes focused around the corrosion of embedded steel, which was discussed in Chapter 2 related to NRC technical data gaps. Concrete can degrade in related ways though, such as through carbonation (Chang & Chen, 2006), aggregate expansion (Johnson & Parsons, 1944), or fire (William, Rhee, & Xi, 2005), though several of these are beyond the scope of this investigation.

Concrete rebar corrosion typically occurs when chloride ions are able to penetrate concrete and reach the embedded steel within (Choi & Yang, 2013). In the presence of sufficient oxygen and water, the chloride ions can drive a pitting reaction in the embedded steel. The equations shown as Equation 7 are a high-level overview of this oxidation-reduction reaction (Ma, 2012).



When the chloride becomes incident to the iron within the steel, it bonds and frees two electrons. These react with any free oxygen and water, as are often present in voids within concrete especially in the course of a leaching or penetration event. The hydroxide formed by this reaction can continue to drive iron reactions, forming FeOOH which can precipitate into hematite (Fe₂O₃), further weakening the steel (Song, Jiang, Chen, Zhao, & Tian, 2017). The iron chloride can further react with water, forming iron hydroxide and hydrochloric acid, which propagates a more corrosive behavior as the oxygen and water sources are sustained.

Preventing the penetration of chloride into the concrete is the foremost way of preventing the corrosion of embedded steel, as the steel inside is protected in a variety of ways, including physical sheltering within the concrete as well as the formation of a passive layer due to the alkalinity of the concrete (Poursaee & Hansson, 2007), though there is dispute as to whether or not magnesium phosphate concretes mild alkalinity is sufficient to cause a passivating layer within the reinforced concrete (Walling & Provis, 2016) (Xing & al., 2017). Chloride ions are more easily able to penetrate porous materials, and the erosion of surface material provides more penetration pathways that are of shorter distance. For these reasons, the focus of this experiment was on the mass retention of the various concrete samples in a variety of applicable conditions.

5.2 Methods

There are multiple methods of determining the corrosion/erosion rate of a material. While methods such as electrochemical accelerated corrosion are beneficial for extrapolating long-time corrosion behavior of a material, they have difficulty in delivering accurate results when the material in question is non-conductive. Additionally, the lack of mechanical erosion from a brine or acid solution lessens the amount of usable information. When concrete sits exposed to the environment, such as dry storage casks can and do, the erosion from rain or acid attack from acid rain can cause just as much harm to the material as can the corrosive environment present within the overpack itself. A long-term exposure using a circulator and acidic or brine solutions can deliver more precise results, as the raw mass change due to corrosion precipitate buildup or raw mass loss due to erosive material removal is captured over the course of months. Figure 17 shows the experimental setup used for this testing.



Figure 17. Four individual circulators made of a small pump connected to a sample housing by tubing.

Each circulator is designed to withstand acids below 1 pH in acidity. PVC piping (white tubing) is used to connect a sample housing (light grey and rectangular) to a pump (black and cylindrical), allowing acidic or brine solution to be agitated within the system, adding an erosive element through the mechanical flow of the solution across the sample. Each of the systems is filled with solution of the selected pH until the sample housing fluid level is slightly above the lowest point of the tubing. At this point, the sample is deposited in the housing. This is done to ensure there is no overflow with larger samples, preserving the fluid and avoiding accidental splashing. This in particular is a strong safety concern, as the experiments are often run with extremely acidic solutions, so any splashed fluid can cause bodily harm. The system is then filled with solution until the fluid level rises above the highest surface of the sample.

At this point, the samples are left for 24 hours to fully saturate. For porous materials such as concrete this is an important step, as the difference between the initial dried mass and the initial wetted mass after saturation is on the order of several percent. If this is considered in the data, trends can be drastically thrown off. The samples are then removed, evenly air dried, and the initial wetted mass of the sample is taken. For these experiments, samples were placed on an absorbent material and given 5 minutes to air dry for each large face, and 2.5 minutes to air dry for each small face. After the mass has been recorded, the sample is deposited back into the housing gently

so as not to splash solution, and the cover closed. The circulators are then run for a consistent amount of time. For this experiment, circulators were allowed to run for an hour after the weighing process. At regular intervals, every other day ideally, the same sample mass measurement process is repeated. After 60 days in solution the sample can be removed, and the circulator cleaned.

5.3 Results

For this experiment, the first chosen solution had a pH of 6.3, made using potassium nitrate and water, as this is where the acidity of much environmental water falls due to the presence of various minerals (Bertolini, Elsener, Pedefferri, & Polder, 2004). The second solution was a higher acidity solution, with a pH of 0.7 made using nitric acid and water. This was chosen to attempt to accelerate the rate of mass loss due to acid attack by all four materials to compare the relative rates. It is also not significantly lower than currently observed acid rainfall, which has reported levels around a pH of 2 (Levy & Przyborski, 2019). Figures 18 and 19 show the wetted mass on the recorded dates for each of the four tested samples for the respective pHs of 6.3 and 0.7.

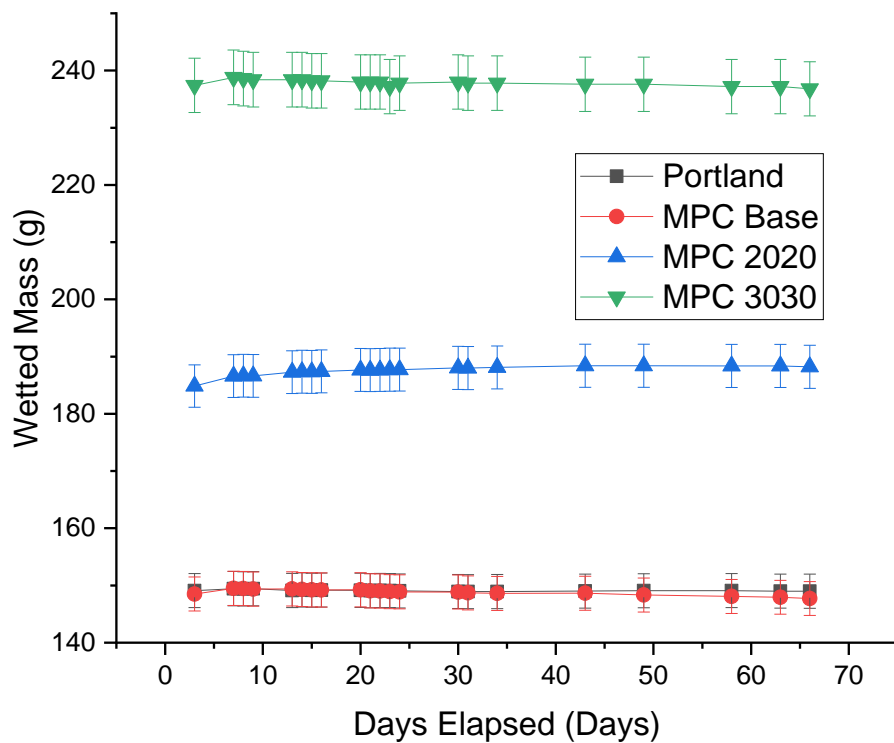


Figure 18. Wetted mass by day for circulator solution of 6.3 pH for the four chosen samples. Replace date with time duration.

Error bars indicating 2% of the total wetted mass have been added to the graph instead of standard deviation or similar error metrics. Slight change in the mass can be observed, but no significant mass loss (or gain) took place. Small gains are due to the buildup of some salts on the samples with metallic aggregate, and for MPC 3030 in particular, are also attributable to the mass balance precision, as the sample was overweight for the precision balance and had to be measured using a less precise machine with a higher weight allowance. This disparity in mass precision was corrected in future experiments.

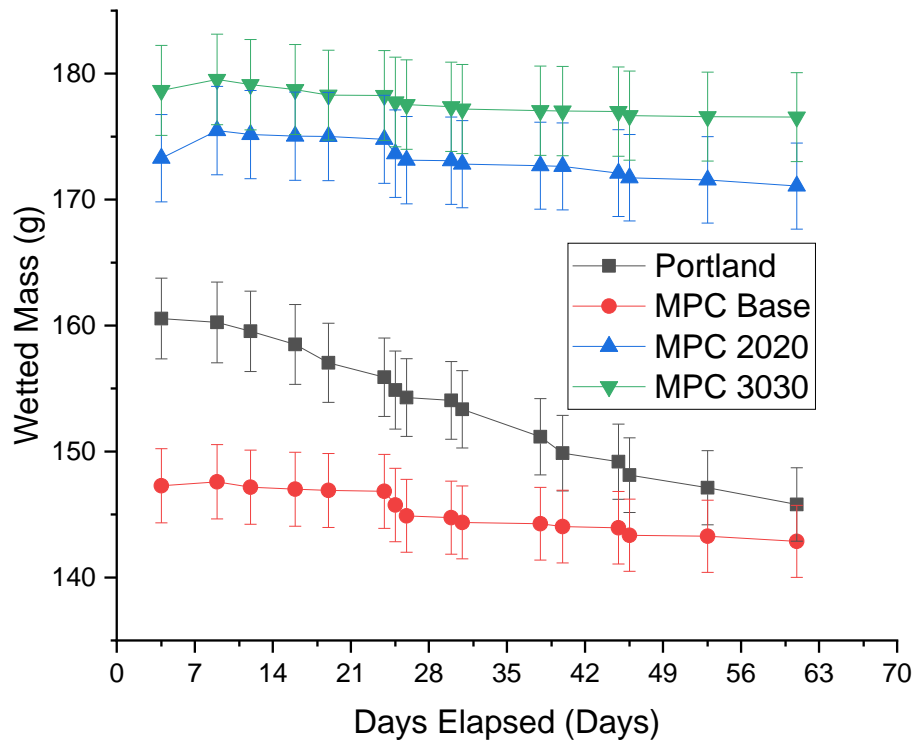


Figure 19. Wetted mass by day for circulator solution of 0.7 pH for the four chosen samples.

The same error bars present in Figure 17 are present in Figure 18. Based on the lack of precision in the 6.3 pH circulator corrosion test for MPC 3030’s mass measurement, a slightly smaller sample was chosen for use in the 0.7 pH run to make better use of the precision balance. While all four samples show more significant mass loss in this solution, only Portland loses more than 2% of the initial wetted mass over the 60 days allotted. Mass change rates have been calculated, converted to millimeter per year (mmpy) for consistency, and displayed in Figure 20.

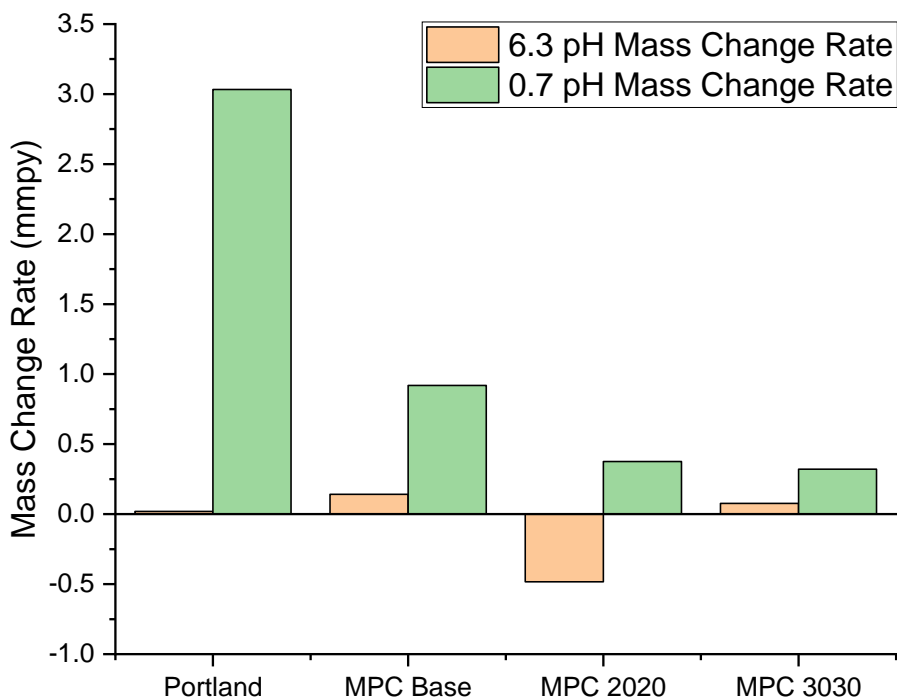


Figure 20. Mass change rates in millimeters per year for selected samples for both pH circulator solutions.

The mass change related to circulation in the 6.3 pH solution is much weaker than the 0.7 pH solution. The primary driver of this difference is the susceptibility of concrete to acid attack, and less so to direct corrosion. Precipitate buildup of strongly adhering salts is responsible for the mass gain seen in the MPC 2020, though the precise composition of the salts is not known. For the purposes of this experiment, more useful information can be gained from examining the mass loss rates due to the 0.7 pH solution. As the corrosion of reinforced concrete is driven by the penetration of acidic and ionic species through the material, mass loss and surface degradation are more harmful to the overall structures these materials are intended for. Portland lost mass at a rate of 3.03 mmpy, while MPC Base, 2020, and 3030 showed rates less than a third of that, at 0.92, 0.38, and 0.32 mmpy respectively. So in highly acidic conditions, all MPC compositions retain mass better than Portland, and aggregate addition to the MPC further inhibits mass loss due to acid attack. This is due to the alkalinity difference of the two binders. As mentioned, Portland concrete ranges in pH from 9 to 13 depending on the time after cure. MPC only reach a pH of 8.5 at the highest point, and are relatively neutral sufficiently far after cure, so the Portland was more alkaline at the time of circulation. This drove a stronger acid-base reaction, responsible for the difference.

5.4 Conclusion

It is poignant to simply show these samples after their 60 days within the circulator, as the comparison is more strongly aided by true visual evidence. Figure 21 displays all 8 samples that underwent testing in the circulators side by side, the top row are the samples that underwent 60 days in a 6.3 pH brine solution, while the middle row are the samples that underwent 60 days in a 0.7 pH acidic solution. The bottom row are four samples that underwent no testing, as controls. From left to right, they are Portland, MPC Base, MPC 2020, and MPC 3030.



Figure 21. The eight samples after their 60 days each in the circulators compared to fresh samples. Top row - 0.7 pH. Middle row - 6.3 pH. Bottom row – fresh. Left to right - Portland, MPC Base, MPC 2020, MPC 3030.

While each sample underwent various changes in coloration, porosity, and surface loss, the starkest difference between fresh and circulated is the Portland sample from the 0.7 pH solution which can be seen in the top left. This sample barely maintained its own shape. In fact, small fragments of it can be seen just to the top right of the sample, circled in red. They fractured off the corner as the samples were gently positioned for this picture to be taken, illustrating the damage that acid attack had on ordinary Portland concrete. No MPC samples had similar levels of degradation due to acid attack or brine circulation. The data from the 0.7 pH acidic circulator experiment showed that MPC

2020 and MPC 3030 both lost around 90% less mass than Portland over the duration, which indicated MPC 2020 and MPC 3030 were superior materials in their resistance to acid attack and brine corrosion. Recalling from Chapter 4 that MPC 2020 attenuates gamma rays 76% better than Portland, and MPC 3030 104% better, the two aggregate MPC continued to improve upon the control groups in each measured metric by considerable margins.

Chapter 6. Mechanical Properties

6.1 Introduction

There are several important mechanical properties for concrete, but the two that are within the scope of this work to discuss are density and compressive strength. These each directly relate to the efficacy of concrete as a construction and shielding material for all forms of nuclear waste. With increasing quantities of stranded spent-nuclear fuel that need to be stored indefinitely, space utilization is a key factor (Werner, 2012). If volume reduction without compromising radiation shielding or structural integrity were possible, the volume of spent fuel that could be stored on-site would potentially increase.

Dry-storage casks need to maintain structural integrity through ‘tip-over’ tests (Huang & Wu, 2009) and several angles of vertical drop (Shirai & Saesuga, 2006). To pass these tests they need to be resistant to impact; compressive strength is one way to evaluate this resistance. As equipment for evaluating high-strength concretes is nontrivial to acquire, and resources for this project were limited, ultimate compressive force will be used to evaluate the materials relative to each other. Ultimate compressive strength would be ideal, but the specific data was not able to be taken.

Density is another relevant metric for waste storage, especially as it relates to the entrainment of radioisotopes as required for grouting applications. Tighter microstructures minimize escape pathways within material, which is one of the primary mechanisms for entrained radioisotopes to escape, analogous to leaching (Ekström, 2001). Porous materials provide pathways for water to leach in and extract ions entrained in ettringite within Portland; the inverse mechanism is of concern here, when immobilized radioisotopes migrate out of an MPC when it heats up and bound water volatilizes.

In addition to the application specific needs of nuclear waste storage, from either reactor or weapons production sources, these metrics are expected of any primary construction material. If MPC 2020 or MPC 3030 are intended for use in construction of radioactive delay tanks for hospitals, or even for simply building the walls around pressure vessel rooms in nuclear power plants, basic mechanical properties such as these must be known.

6.2 Methods

Density was determined through volume and mass measurements. The mass of each sample was measured with a Radwag XA balance, and volume was calculated with measurements of each side length taken by Vinca Digital Vernier calipers. The side lengths were multiplied into the volume, which was divided by the mass. The density values for each composition were averaged to conclude a final calculated density.

Ultimate compressive force measurements were obtained using Mark-10 Model M3-500 Force Gauge. For this force gauge, samples as manufactured are placed within the horizontal clamp, and the user manually operates a lever, imparting force until the material fails, in the case of concrete this was through shear. The highest force of compression is measured by the equipment.

6.3 Results

Figure 22 displays both the measured ultimate compressive force as well as the calculated density of the samples alongside each other, for comparison.

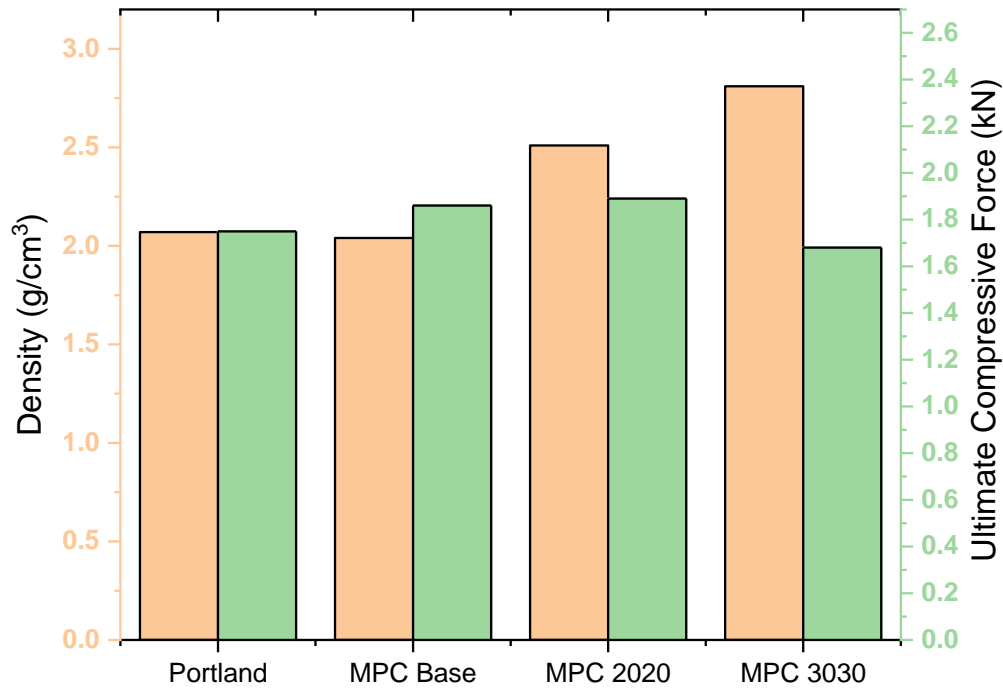


Figure 22. Ultimate compressive force of selected samples.

Ordinal axes have been set so that Portland displays a density equivalent in height to the ultimate compressive force, as Portland concretes are the standard. In essence, this means that any material with an ultimate compressive strength that displays as a higher bar on this plot than its own density has improved mechanical properties to Portland, doing so with less weight required.

While there were larger differences in the ultimate compressive strength measured by the manufacturer during the initial composition optimization tests done, there are only small differences shown in the ultimate compressive force by Figure 22. Similar trends hold true, though. MPC Base improves upon Portland, MPC 2020 improves upon MPC Base, and MPC 3030 is the weakest of the four samples. The structural differences between MPC Base and Portland are primarily in the density of the hydration product, so it is expected that MPC Base will be somewhat stronger inherently. MPC 2020 includes aggregate, and while magnetite does improve the mechanical strength of the material as evidenced by the increase in ultimate compressive force, it does not do so at a rate that surpasses the increase in density from the addition of lead. The lead increases the density, but also weakens the concrete by replacing some amount of struvite-k which lowers the barrier to fracture; this can be inferred from existing research that shows heavy iron aggregate in concrete improves the fracture resistance (Kan, Pei, & Chang, 2004). MPC 3030 shows a similar increase in density but continued decrease in ultimate compressive force due to

the increasing presence of the mechanically weak lead. Table 6 shows the numerical values of these properties, for completion.

Table 6. Ultimate compressive force and density of selected samples.

Property	Portland	MPC Base	MPC 2020	MPC 3030
Density (g/cm ³)	2.07	2.04	2.51	2.81
Ultimate Compressive Force (kN)	1.75	1.86	1.89	1.68

6.4 Conclusion

Increased density and ultimate compressive force are desirable properties for a material to have in all nuclear waste storage applications. The three MPC compositions had increased density when compared to base Portland, but the aggregate MPC compositions did so without a correspondingly high increase in ultimate compressive force. MPC 2020 improved in both metrics, but the density increase was not offset by the ultimate compressive force increase, meaning it was a stronger material but the increase in strength came at the cost of an increase in weight. This would introduce some problems with regards to spent nuclear fuel storage, given the massive volume of material needed. Spent fuel casks and their housing have to be stored on specially designed pads made from seismically durable concrete. These pads can only accommodate so much mass before they will fracture themselves, so the required weight to safely store the spent fuel cannot significantly increase past the initial design limits. This means density increases must be surpassed by strength and attenuation improvements. MPC 3030 had shown in prior chapters to improve upon the tested properties but was slightly lacking in mechanical properties. MPC 2020 was close enough in density and ultimate compressive force that it was valid to conclude it was a better material than Portland based on prior parameter improvements.

Chapter 7. Outgas Properties

7.1 Introduction

Many materials undergo a behavior known as outgassing, in which the material loses vapor of some constituent or bound component under normal or abnormal operating conditions. In the case of concrete, it can happen naturally as the slow-to-hydrate di-calcium silicates continue to react and release byproducts over the course of months. This outgassing behavior has many potential negative consequences. In primary construction, it can promote the growth of mold, which is then aerosolized from the pores within Portland as bound water outgasses (Swanson, 2001). When concrete is used to immobilize radioisotopes, such as tritiated water (water with the radioactive hydrogen-3 instead of the more abundant hydrogen-1), outgassing has the potential to volatilize the radioisotope itself, and emit what it was intended to entrain. This is why vitrification is the current immobilizer for hard to entrain radioisotopes (Weber, Navrotsky, Stefanosky, Vance, & Vernaz, 2009).

In order for a concrete to be technologically competitive with vitrification for the purposes of nuclear waste immobilization, it needs to outgas far less than current concretes. Vitrification is a much more complex and expensive process than grouting, with estimates for Hanford's LLW alone showing that vitrification costs between \$18 and \$28 Billion more than grouting (Federally Funded Research and Development Center, 2019). For these reasons, a cheaper alternative such as the grouting method of blending nuclear waste with concrete formers that are effectively just coal-plant waste is desirable. Currently these grouting applications are for lower level waste rather than vitrification, but a concrete that can immobilize the higher activity radioisotopes would free up vast amounts of nuclear waste disposal budget to be used in remediation and cleanup, moving towards a true end-state for many of the legacy sites surrounding nuclear weapons development.

7.2 Methods

There are multiple ways to evaluate the outgas mass loss of concrete, but the simplest is to heat a sample of known mass for a set duration and measure the mass again after heating. Any mass loss between the can be attributed to outgassing. The samples were left on a Scilogex MS-H280-Pro Hot Plate for a set duration at a specific temperature. Masses before and after heating were taken on an OHAUS Mass Balance. The first temperature selected for use in outgas testing was 55 °C, with a drying duration of 24 hours.

7.3 Results

Samples were evaluated for this mass loss due to heating. The results of the 55 °C 24 hr heating are shown in numerical form in Table 7, and in Figure 23. No samples show a significant loss of mass due to heating at low levels, though the dense microstructure uninterrupted by aggregates of MPC Base is the most successful at retaining all entrained material.

Table 7. Outgas mass loss in percent of initial mass over a 24 hr drying at 55 °C.

Portland	MPC Base	MPC 2020	MPC 3030
0.29	0.04	0.18	0.26

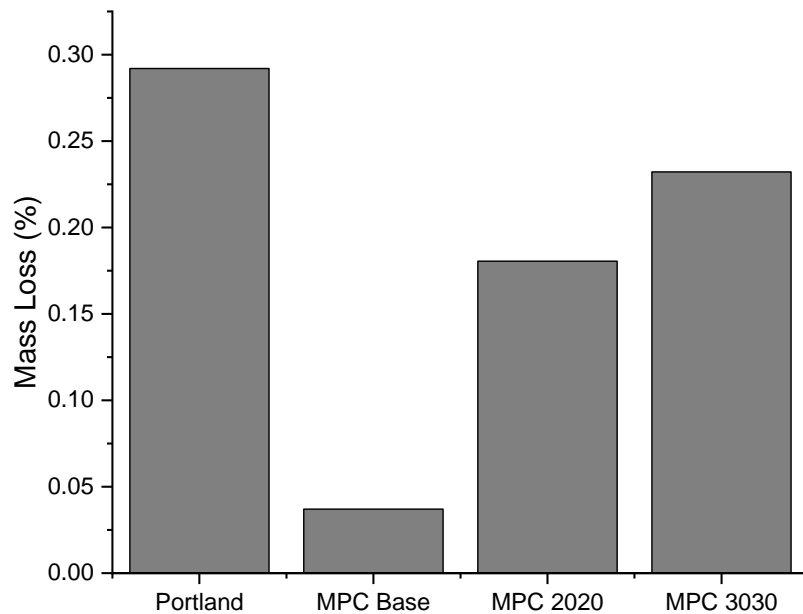


Figure 23. The mass difference due to outgassing after 24 hours of heating at 55 °C.

All MPC samples outgassed less than all Portland samples. This was due to the difference in microstructure between C-S-H and the struvite-k formed in MPC. As discussed in Chapter 1, Portland concrete forms C-S-H through a hydration reaction, which holds together the various aggregates through its honeycomb crystal structure. This structure was weaker and less dense, as shown in Chapter 6, both of which contributed to the larger loss in bound water through heating when compared to the denser matrix formed by the acid-base 'hydration' reaction in MPC. The metallic aggregates that were retained within the struvite-k matrix likely caused lattice strain, or on a larger scale simply created more grain boundaries, leading to increased escape pathways for the bound water (Llorca, Needleman, & Suresh, 1991).

7.4 Conclusions

With each MPC, the denser microstructure imparted by struvite-k reduced porosity and thus reduced the amount of pathways for bound water to volatilize from within the concrete. Aggregate addition to the MPC caused strain within the struvite-k and added grain boundaries that increased the amount of these escape pathways, but not to the same degree that Portland had inherently. For these reasons, MPC compositions outgassed less than Portland across all tested compositions. MPC Base was the most effective material tested at mass retention through heating, implying it would be the best candidate for waste immobilization purposes. Due to the nature of nuclear waste immobilization, many of the prior properties such as gamma attenuation and corrosion resistance are less impactful than simply entrainment. Waste forms, when grouted, are typically in vast containers themselves, with millions of gallons of capacity. The sheer volume of material is sufficient to shield any and all activity, and the quantity is internally stable enough that very little would be capable of impacting mechanical damage to it. For these reasons, MPC Base was the most effective material tested for the purposes of nuclear radioisotope immobilization.

Chapter 8. Thermal Dehydration

8.1 Concrete Dehydration

There are a variety of reasons that thermal degradation evaluation is necessary for nuclear waste storage materials. The foremost of which is that concretes are well documented as thermally unstable at a variety of temperatures (William, Rhee, & Xi, 2005). As Portland concrete is the industry standard, the degradation of this will be discussed first.

Up to 300 °C, Portland concrete exhibits stable behavior, with only typical thermal expansion as notable feature changes (Sellevold & Bjøntegaard, 2006). Once it passes that threshold, water loss begins to occur, and the concrete will physically shrink. This process is partially dependent on pore humidity in a non-linear fashion, but also somewhat linearly proportional to the water content, so the coefficient of shrinkage is treated as a constant (Bažant, 1983). Past 400 °C full material decomposition begins. C-S-H begins to degrade at that temperature, with a secondary degradation occurring at around 600 °C (Hager, 2013), and at 900 °C the compound completely breaks down internally, with no bonds remaining. For these reasons, Portland based concrete is considered to be nonfunctional after 400 °C (Tufail, Shazada, Gencturk, & Wei, 2017).

Magnesium phosphate concretes also have thermal degradation issues, some starting as early as with the hydration process. The initial hydration reaction shown in Chapter 1 is so aggressively exothermic, that if it is initiated without a retarding agent, such as boric acid, the reaction can move to completion so exothermically that it dehydrates the cement paste by boiling off the water before the paste has a change to set (Lahalle, et al., 2016). There is also some existing research into the thermal instability of struvite-k. The latter instability is the largest challenge associated with magnesium phosphate concretes in high temperature applications. In most studies of the material in lab settings, synthesized powdered struvite-k is found to dehydrate between 50 and 60 °C. It

undergoes a simple one-step dehydration which when driven to completion results in A 58.5% mass loss (Zhang, Shi, Huang, & Zhang, 2013). This is equivalent to the behavior of Portland concrete at 400 °C, which is a considerably higher temperature for material breakdown.

8.2 Dehydration Evaluation Methods

This investigation started by use of a TA Q200 differential scanning calorimeter (DSC). Setup for the DSC Q200 followed the traditional calibration procedure described in the Thermal Analysis supplied Quick Start Guide. For initial tests, a small fragment of material was placed in the sample pan and loaded into the DSC. These fragments were obtained through the fracture of larger, as-manufactured samples using a hammer and chisel. Helium was used as a purge gas at a flow rate of 50 mL/hr, and heating was performed from 40 to 170 °C. As the MPC dehydration canonically occurs in the 50-60 °C range, but the DSC is not capable of outputting a heating cycle sufficient to encompass the full degradation of Portland up to 900 °C, it was decided that only the dehydration of MPC would be studied in full. The thermal behavior of Portland is incredibly well documented, and any curious readers may trivially find that information from a variety of sources, including those in the previous section.

Once the behavior was confirmed through this method, further investigation into the kinetics of the dehydration took place using the same Scilogex hot plate used in the outgas experiments. To study the progression of the phase change, video was recorded of the sample as it was heated isothermally (within machine limits), and the time progression was tracked through the material. Thermocouples were attached to the top and bottom face of the samples so the temperature profile within the material could be determined. For the purposes of this testing, the dehydration reaction was treated one dimensionally, propagating through the material along the centerline as the temperature threshold was reached.

After experimental evaluation was performed, and multiple dehydrated samples had been created, analytical testing was performed on the samples to further characterize the dehydration of struvite-k in the manufactured MPC samples. For these tests, the following equipment was used: a Rigaku SmartLab X-Ray Diffractometer for evaluating the phase composition of samples, a Hitachi S3200N scanning electron microscope with a Robinson backscatter detector for high magnification imaging and energy-dispersive x-ray spectroscopy to elementally map samples, an XPS/UVS –

SPECS System with PHOIBOS 150 Analyzer to further evaluate the composition of the sample through bond resonance.

8.2.1 Differential Scanning Calorimetry

Differential scanning calorimetry is an analytical technique that uses the difference in measured heat flux through a reference material and the sample material to determine the thermal behavior of a material over a wide temperature range. Most commonly, DSC experiments are used to determine the glass transition temperature of a polymer, the melting or crystallization temperature of a solid, or temperature measurements of reacting systems (GROENEWOUD, 2001).

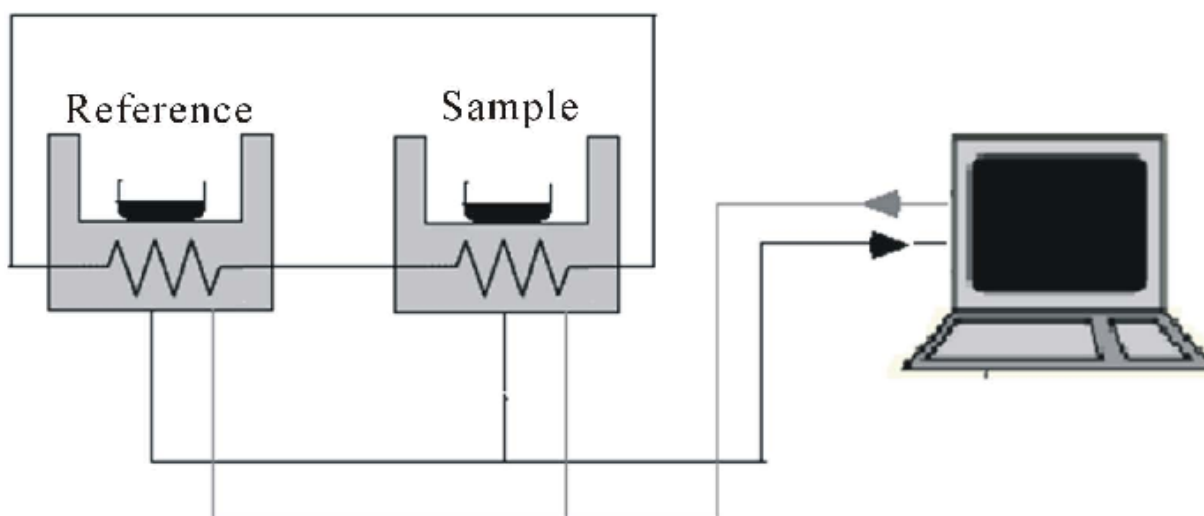


Figure 24. A sample schematic representing the DSC process (Ghandi, 2013).

Small pans contain the reference and the tested sample which are situated on small pedestals within an environmentally controlled chamber. These pedestals are heat resistive material surrounding thermocouples. A purge gas is flowed through the chamber, and the heating elements surrounding it begin to raise the temperature. As the temperature rises, heat flows through the samples and into the thermocouples beneath. The difference between the two creates the reading of heat flow as processed by the software. As changes occur within the sample material, such as a glass transition or a melt, the heat flow through the sample changes relative to that of the reference, and so information about the change in heating can indicate the nature of a departure from linear heat flux. Figure 24 briefly shows the circuit diagram related to these features.

8.2.2 X-Ray Powder Diffraction

There are several forms of x-ray generation that are possible, each with their own characteristic properties and procedures. Bremsstrahlung, or the “slowing-down” x-rays will be the first discussed. Figure 25 illustrates this process. When an electron passes through the electromagnetic field generated by a nucleus, it can slow down and emit a photon, satisfying the conservation of energy principle. Due to the continuous nature of electron kinetic energy conversion, Bremsstrahlung emits photons along a continuum.

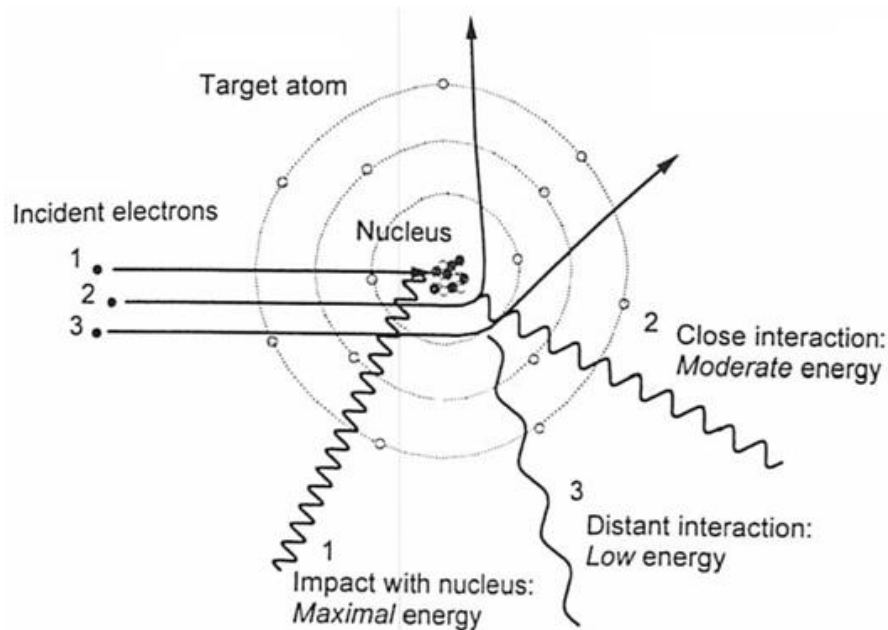


Figure 25. The generation of Bremsstrahlung radiation, from the slowing down of an electron due to the electromagnetic field generated by a nucleus (Thayalan, 2014).

A potential difference is created between an anode and cathode, with electrons accelerating along the gap. They pick up kinetic energy and deliver it as they impact the anode. 99.5% of the time this impact causes waste heat loss and produces nothing usable. 0.5% of the time the energy loss is great enough, and the angle of impact with the target atom sufficient that instead of impacting and creating waste heat, the electron will slow down creating the x-ray. As this is not based on a discrete energy level step, a true polyenergetic spectrum is formed. It typically takes the form of a continuum closely described by Kramer’s Law, which is shown as Equation 8 (Laguitton & Parrish, 1977).

Equation 8.

$$I(\lambda) d\lambda = K \left(\frac{\lambda}{\lambda_{\min}} - 1 \right) \frac{1}{\lambda^2} d\lambda$$

The next production method that can occur is the characteristic x-ray. This x-ray is formed when the incident electron directly impacts an inner, or k-shell, electron. The inner electron is ejected, with a higher shell electron from the l-shell dropping in energy to fill the void. This step change in energy produces an x-ray with energy corresponding to that size of the energy gap. As it is emitted at one of the characteristic energies for each atom, this photon is known as the characteristic x-ray.

The application of these principles in an x-ray tube is what allows machinery to generate the necessary x-rays for imaging and similar applications. X-ray tubes are traditionally glass, containing filaments that have a very precise voltage driven across them, combined with a precise amperage, creating the thermionic emission spectrum desired for the electron energies needed to create the proper x-rays. A focusing cup is sometimes used to bias the electron generation and control the path they take. As these x-rays are generated in a broad band, and not all can be precisely directed to the target, leakage needs to be accounted for in design. Lead is used internal to the housing to mitigate as many of these leakage x-rays as possible, with a maximum leakage emission capped federally as 100 mR/hour at 1m distance when the tube is operating at maximum output (Office of Medical Products and Tobacco, Center for Devices and Radiological Health, 2008).

X-Ray powder diffraction is one of the more useful tools available to researchers today for the purposes of phase identification in materials. It is based on the principle of diffraction, as x-rays are no different from visible light for the purposes of transmission through or scattering off a material. X-Rays are generated in a traditional x-ray tube and transmitted to a sample, then collected by a detector. The x-ray tube and detector rotate around the sample, capturing measured intensity at each of the angles. Whenever the angle of the x-rays and the sample satisfies Bragg's Law, shown as Equation 9, constructive interference occurs and a high intensity peak is captured. This signal is stored in pair with the angle at which it occurred, and the collection of these data points corresponds to a traditional XRD 2θ graph that is seen in literature (Dutrow & Clark, 2019).

Equation 9.
$$2d \sin \theta = n\lambda$$

This technique has a variety of applications as it relates to concrete. One of the most prominent uses of XRD in concrete research has been in determining the hydration behavior of Portland

cement. Due to the phase complexity of any concrete, determining the actual phases present from the results of an XRD experiment is nontrivial, and doing so in the middle of upwards of five distinct chemical reactions is extremely difficult. For these reasons, the work of Scrivener et al. in their 2004 article in *Cement and Concrete Research* is an impressive achievement. They develop an XRD/Rietveld analysis of Portland cement hydration over time, allowing the time dependent behavior of the various chemical reactions to be determined, illustrating the complexity of concrete chemistry (Scrivener, Füllmann, Gallucci, Walenta, & Bermejo, 2004).

XRD has been commonly used to verify the presence of minerals in base cements for study in concrete hydration. Many researchers have performed XRD on the cement powder itself prior to hydration, noting the presence of specific minerals they sought to react with during hydration (Nochaiya, Wongkeo, & Chaipanich, 2010).

8.2.3 Scanning Electron Microscopy and Energy-Dispersive X-Ray Spectroscopy

While optical microscopes from the biologic, chemical, and metallurgical field have at best a resolution limit around 100 nm, electron emission microscopes are capable of finer images. Scanning electron microscopes (SEM) can capture 1 to 10 nm resolution, 1000x that of the highest quality optical microscopes. Transmission electron microscopes (TEM) are even more detailed, reaching resolutions of 0.5 nm. There are, however, functional limits on the imaging magnification that can be used with materials like concrete that are high in hydrogen content. Backscattered electrons must be used, with the machines in variable pressure mode. This creates magnification limits closer to 1000x, but still improves upon what an optical microscope is typically capable of achieving for samples such as these.

The first step in electron microscopy is the generation of the electrons used for imaging. This is most often done using tungsten filament, LaB₆ crystal, or a ZrO/W Schottkey emitter. They are heated, allowing electrons to escape the material used. If a sample is incredibly heat sensitive, there are cold field emission options using tungsten whereby electrons can be released without heating, but they are incredibly expensive to build, maintain, and operate.

In either case, the next step in the imaging process is the use of “lenses” to focus the electron beam. These are not optical lenses as in metallurgical microscopes, but electromagnetic lenses serving

the same basic function. They are typically numerous coils of insulated copper wire formed into an annulus, with the electron emission beam running down the center void. This allows the magnetic field generated to focus the electron beam into a circular path. While one might imagine that removing a physical medium of transmission from the lens proper might reduce the aberrations possible, the same phenomena continue to occur. The most prevalent is axial astigmatism. This aberration is very frequent, and typically must be corrected for nearly every refocus to ensure optimal image quality. It is noticeable in the image as a blurring along only a single axis, so an image with sharp resolution along the vertical axis but experiencing some blurring along the horizontal is indicative of axial astigmatism (Kaech, 2013).

A complementary technique to SEM is that of energy-dispersive x-ray spectroscopy. This is a technique that utilizes the characteristic x-ray generation potential of an electron beam to allow spectroscopy of a sample. Figure 26 illustrates the physics of this principle.

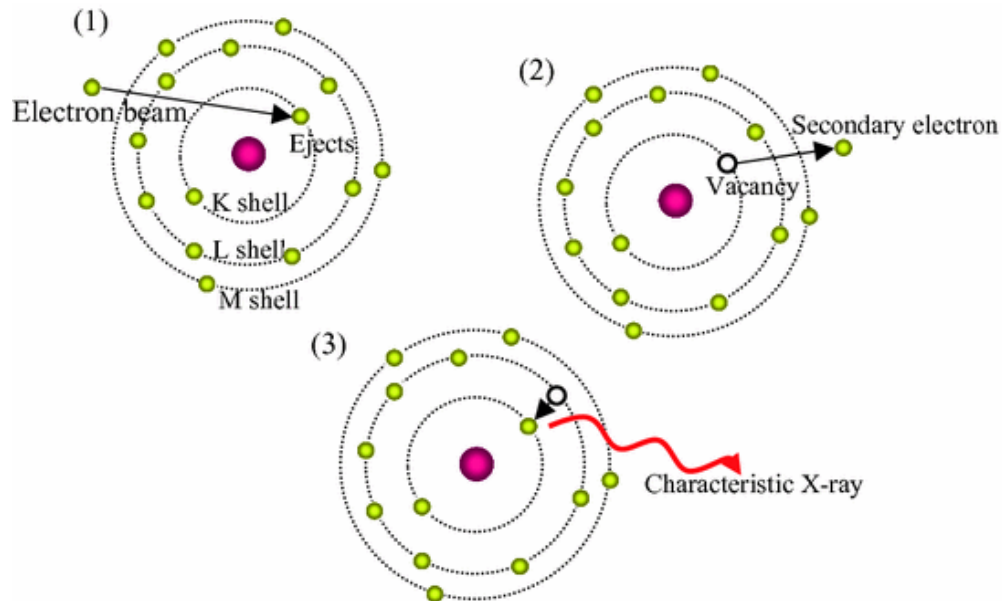


Figure 26. The atomic scale principles of EDS, wherein an electron generates a characteristic x-ray (Morita, 2018).

When the generated electron beam collides with an atom's electron, it can eject through a relatively elastic collision. Doing so emits a secondary electron and creates a vacancy within the inner shell. The secondary electrons are typically much lower energy than the backscattered electrons and are unable to be used for imaging materials like concrete, which need to operate in variable pressure

mode. The vacancy within the inner shell is filled by an outer-shell electron dropping down from a higher energy level. The electron moving between energy bands releases a characteristic x-ray at a precise energy, which is used to not only specify the element which released the electron, but which electron it was.

The coupling of these two forms of analysis allow microstructural observation and elemental analysis confirmation of near surface levels of the material. This technique is commonly applied to Portland concretes for determining porosity (Head & Buenfeld, 2006) or elemental doping (McWhinney, Cocke, Balke, & Ortego, 1990). For these reasons, they were techniques that were sought out for this project.

8.2.4 X-Ray Photoelectron Spectroscopy

Another analytical technique that was used to perform elemental analysis was x-ray photoelectron spectroscopy. This technique uses an x-ray source to irradiate the surface of a sample, in the case of a concrete it is in powder form. The x-rays are absorbed by various atoms within the sample down to a depth of around 5 nm (Doh, Papaefthimiou, & Zafeiratos, 2015). This x-ray imparts enough energy to drive the emission of a electron, specifically a photoelectron. This is an analytical application of the photoelectric effect which was discussed in Chapter 4. Figure 27 shows the process of this interaction.

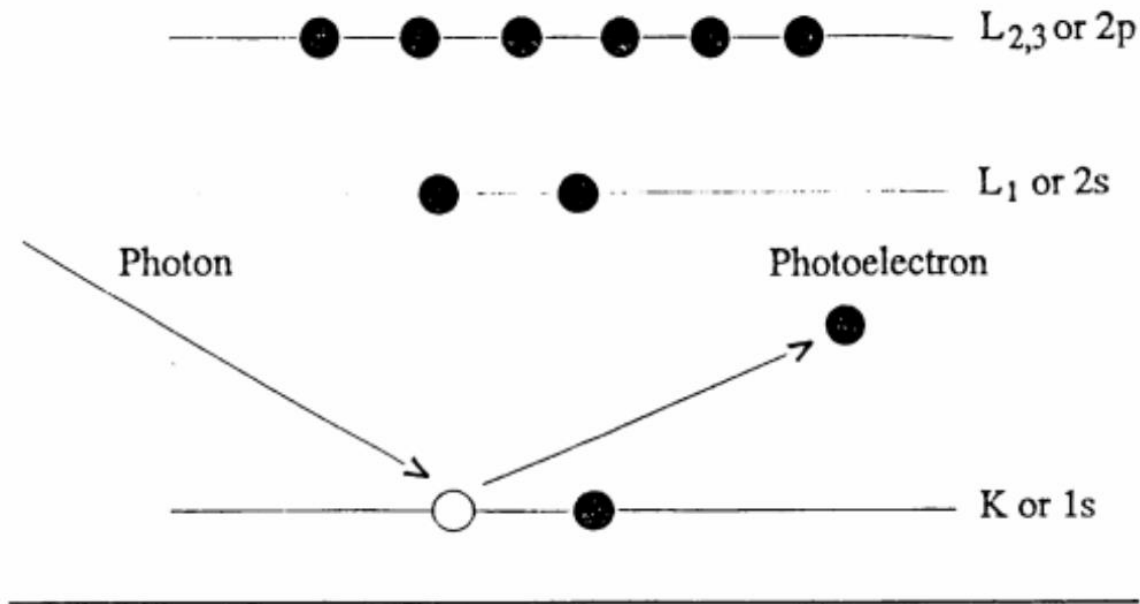


Figure 27. The photoelectric effect as applied in XPS (Moulder, 1991).

By varying the energy of incident photons and collecting the electrons using detector that preserves information about their kinetic energy, Equation 10 can be applied to determine the binding energy of the electron.

Equation 10.
$$E_{binding} = E_{photon} - (E_{kinetic} + \phi)$$

In this equation, there is a minor correction factor present called the work function, ϕ , which is used to account for any losses of energy due to detector absorption. It is typically on the order of a few eV. The binding energy of these electrons is collected for each photon energy level used in the experiment, and the results are plotted together with the intensity of counts on the ordinate axis.

Interpreting this data is relatively straightforward, as books such as the Handbook of X-Ray Photoelectron Spectroscopy (Moulder, 1991) have catalogued canonical peaks of each electron shell and spin for each element. A survey plot is first calibrated to known peaks, typically through a strong element signal that emits an auger electron in addition to a photoelectron. In the case of concretes such as those in this work, carbon was the element selected for this process. Once any small eV calibrations have been made, each major peak is compared to elements expected to be within the material, and higher resolution scans of those peak regions are made. This allows

background to be corrected for on an elemental basis, and comparisons of relative atomic composition between differing samples can be made (Moulder, 1991).

8.3 Dehydration Characterization Results

8.3.1 DSC Results

The results of the heating cycle from 40 to 170 °C using the Q200 DSC are shown in Figure 28.

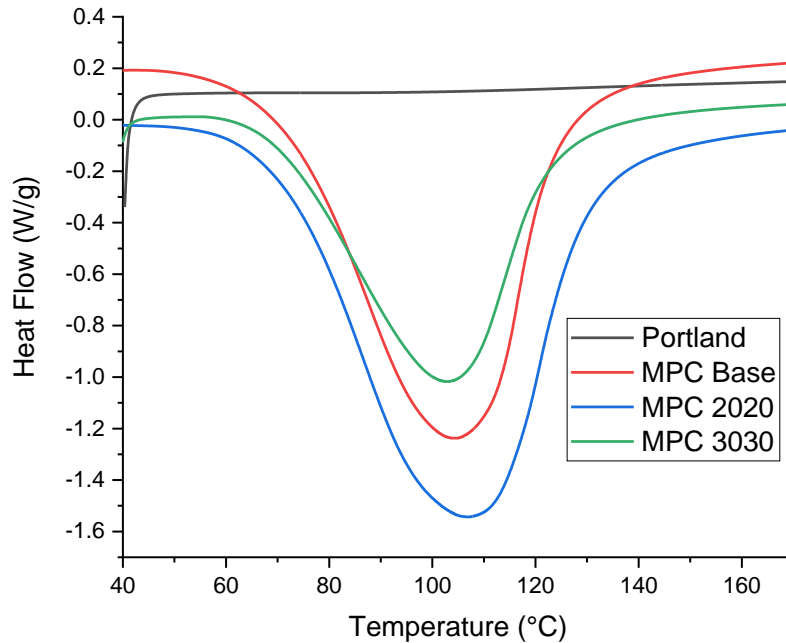


Figure 28. Heat flow curves output by the DSC Q200 for a 40 to 170 °C heating.

In a DSC heat flow diagram, an exothermic extrema is characteristic of a crystallization phase change, based on the energy released from an energetically favorable reordering (Kousksou, Rhafiki, Mahdaoui, Bruel, & Zeraoui, 2012) (Šesták, 2005). The crystallization minima seen in the MPC samples at around 107 °C is not present in Portland, as Portland does not undergo a phase change due to heating within this temperature range. This feature is not present in secondary runs of the same sample, or in heat-cool-heat cycles of fresh samples, indicating that it is an irreversible phase change of the MPC material. This behavior is consistent with a one-step dehydration reaction, as anticipated by the literature based on the degradation of both cement materials.

It can be seen from the start of these local minima features on each MPC curve that the departure from constant heat flow takes place at a higher temperature as the metal content of the sample increases. Further investigation of the dehydration took place using the hotplate.

As it is not possible to include video in a textual report, those will be saved for the presentation, but three screenshots of the MPC 2020 sample over time will be shown in Figure 29. They are taken from precisely the hour marks of the experiment.

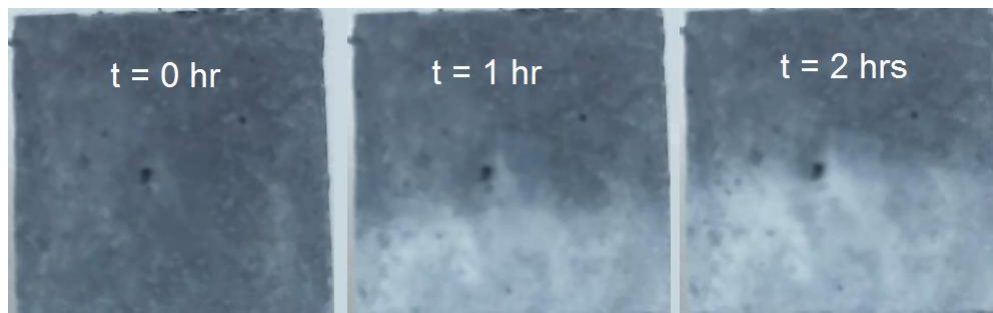


Figure 29. Progression of the dehydration reaction through MPC 2020 at 115 °C.

The phase change progresses as a distinct color shift of the material moving mostly linearly away from the heat source (on the bottom, as oriented). For the purposes of marking the distance from the heat source, the centerline of the material is used. Based on further investigation, the semi-random progression of the phase change front horizontally grows more chaotic as aggregate concentration increases, and in the case of MPC 3030, was not possible to track using the same methods as MPC Base and MPC 2020.

Figures 30 and 31 show the linear progression of the dehydration over time, with bottom and top surface temperatures included. While these figures end the progression at around 3 cm away from the heat source, recall that these cubes are 5 cm side length, so the dehydration is not able to fully propagate through the material. The phase change takes a small amount of time once the material has surpassed the initiation temperature, but once the reaction begins it progresses at a linear rate until around 3 cm in the material, at which point progression slows almost to a stop. As the bottom temperature is not increasing, and the top temperature at that point is no longer increasing, the reason for this is likely due to the internal temperature of the material not being sufficiently high to continue to the progression of the reaction. In both cases shown, the temperature at the top of the material stops below 60 °C.

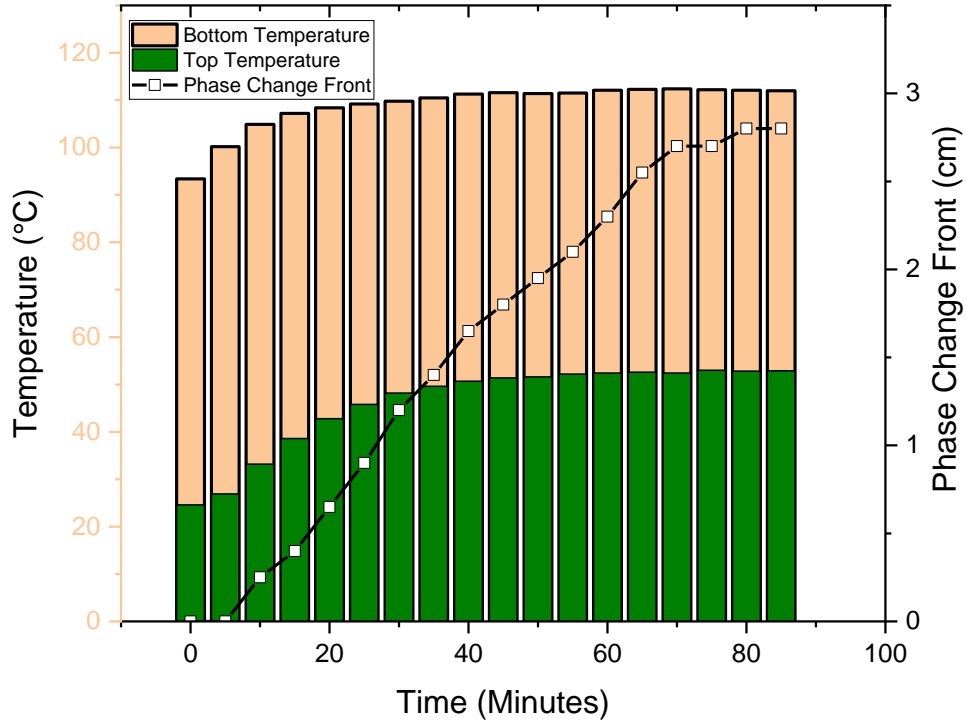


Figure 30. Progression of the phase change front in MPC Base at 115 °C.

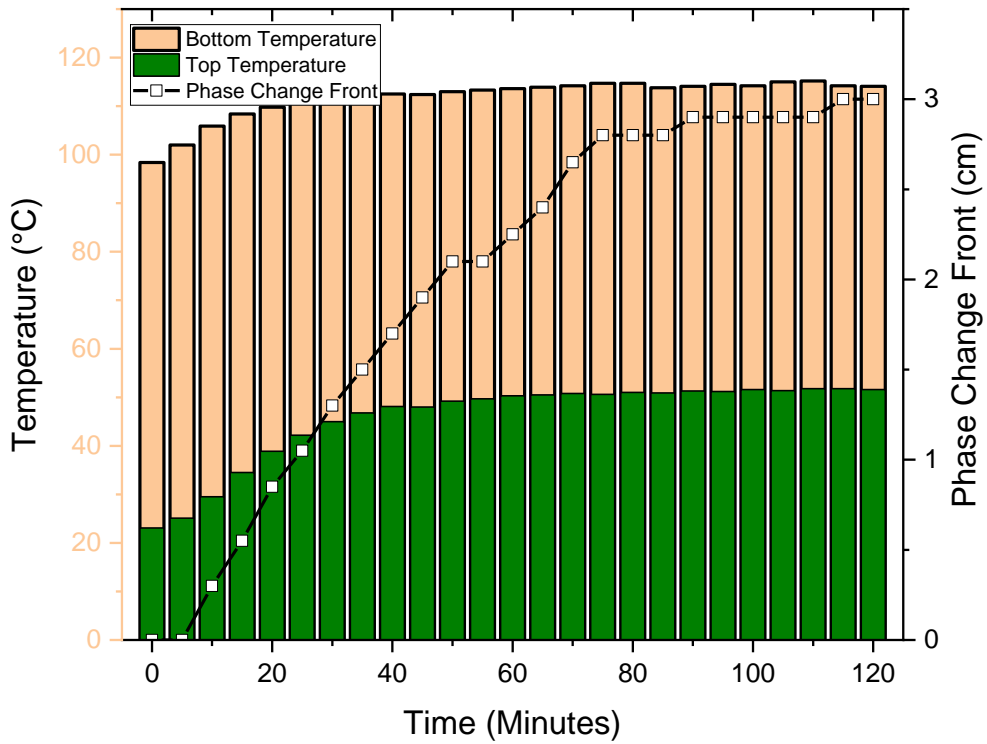


Figure 31. Progression of the phase change front in MPC 2020 at 115 °C.

Further information about this thermal degradation can be obtained through the use of analytical instruments like x-ray powder diffraction (XRD), scanning electron microscopy (SEM) with energy-dispersive x-ray spectroscopy (EDS), and x-ray photoelectron spectroscopy (XPS).

8.3.2 XRD Results

Analyzing the results of XRD as they relate to composite, heterogeneous materials is challenging at best due to the presence of incredibly complex peak results. Figure 32 shows a pair of 2θ plots of struvite-k taken from two distinct studies to illustrate the differences in appearance that a singular complex mineral can have.

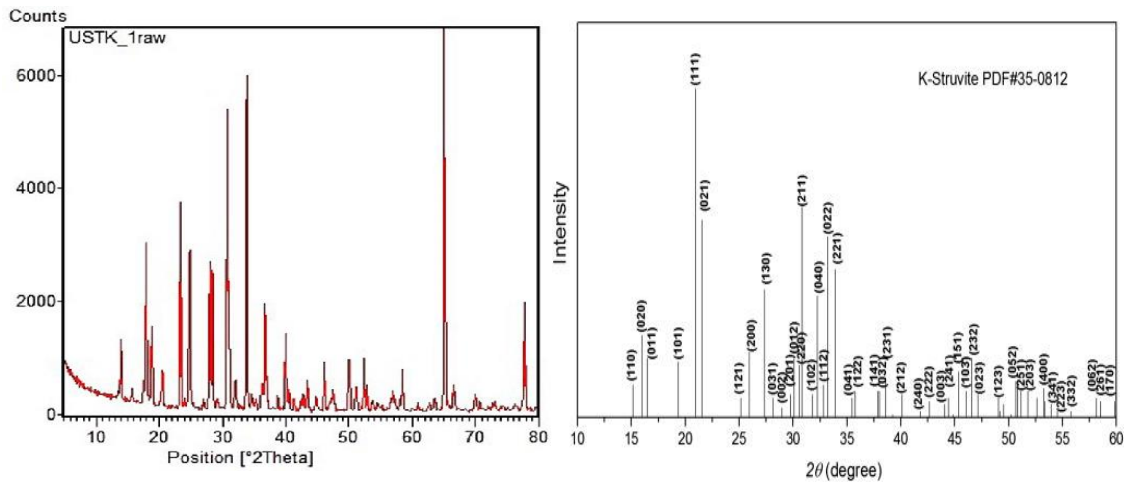


Figure 32. Two XRD 2θ graphs of struvite-k from different studies. Left- (Suryawanshi & Chaudhari, 2014). Right- (Shih & Yan, 2016).

Large peaks that are present in the left graph in the 60° to 80° range were not even evaluated for in the graph on the right. Furthermore, the relative intensity of peaks at 34° and 23° in the graph on the left invert for the graph on the right. Keeping this in mind, the results of x-ray powder diffraction from 10° to 70° for Portland, MPC Base, MPC 2020, and MPC 3030 will be shown in Figures 33 through 36.

There are several distinct peaks in this plot, all of which correspond well to known compounds that make up Portland concrete. Silicon oxide in quartz form corresponds to the peaks at 21° , 27° , and 68° . Calcium carbonate in the form of calcite is another common material within Portland and is responsible for many of the smaller peaks at 27° , 33° , and 50° . As this project is focused on MPC, more time will not be spent discussing the composition of the control.

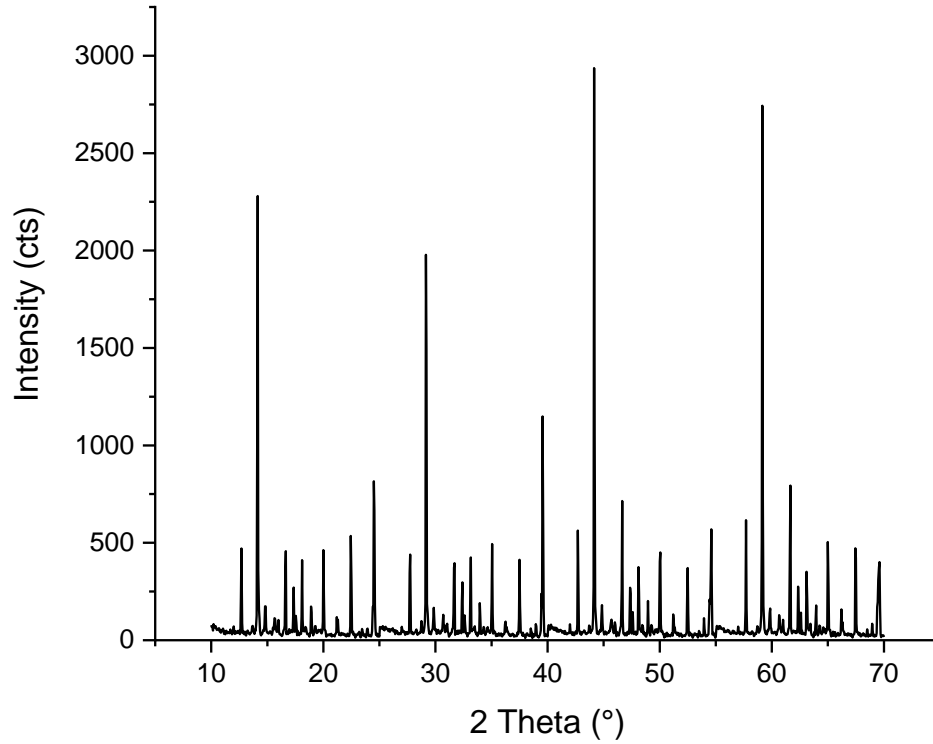


Figure 33. Plot of the peak intensity over the tested 2 theta range for Portland.

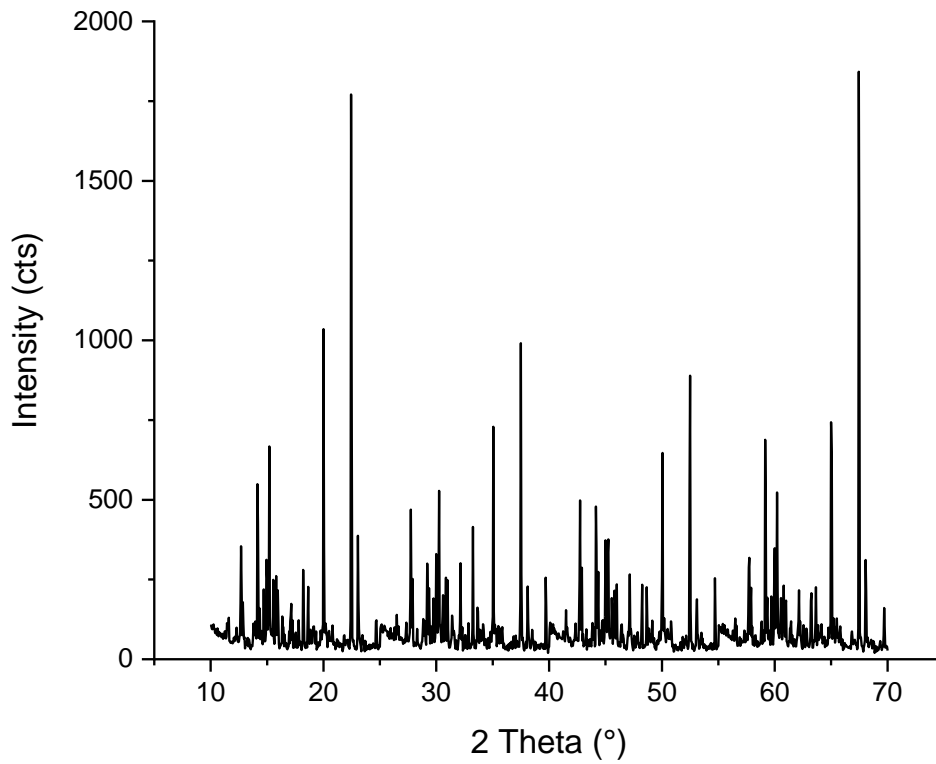


Figure 34. Plot of the peak intensity over the tested 2 theta range for MPC Base.

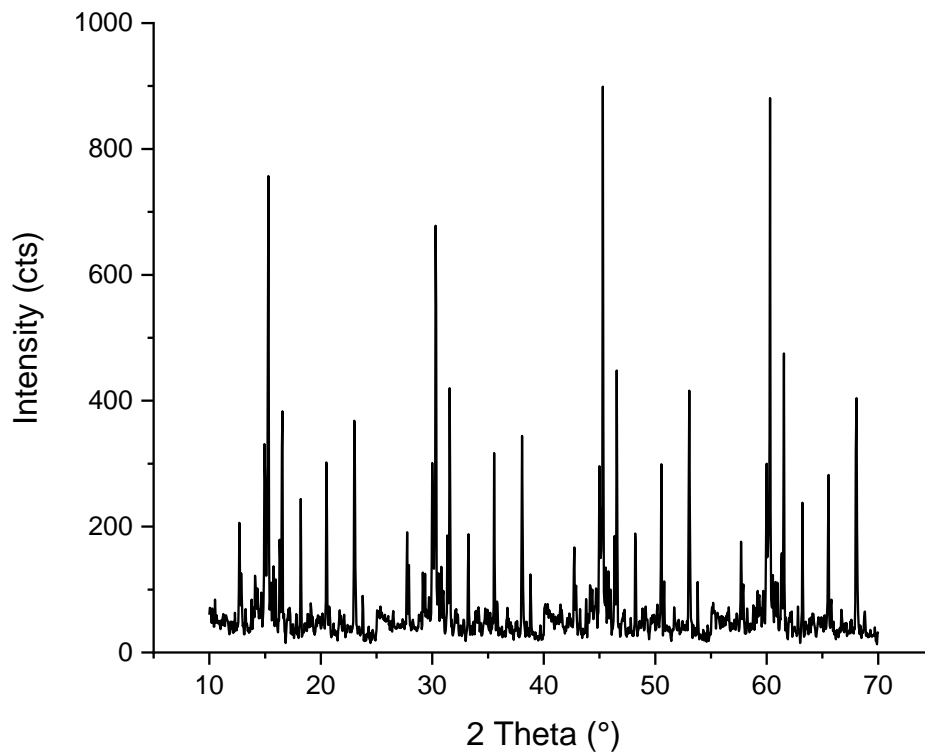


Figure 35. Plot of the peak intensity over the tested 2 theta range for MPC 2020.

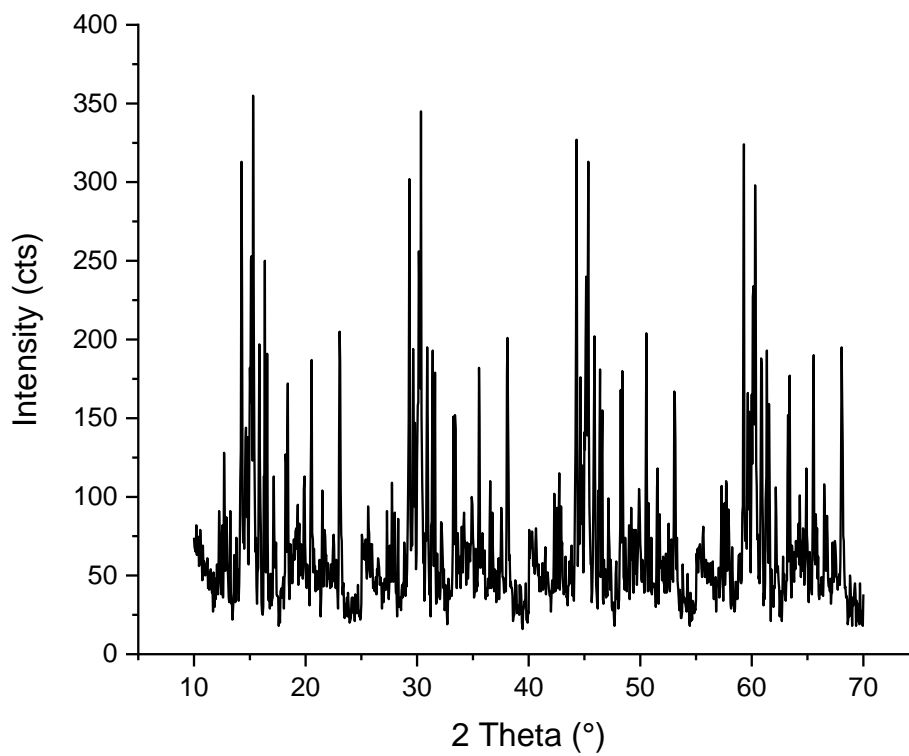


Figure 36. Plot of the peak intensity over the tested 2 theta range for MPC 3030.

The first feature that varies between the MPC plots is the absolute intensity. While this is not a strict measure of anything, it does trend strongly with the increase in gamma ray attenuation. While x-rays and gamma rays are technically distinct, they are both photonic radiation forms, and a material that has a strong gamma attenuation coefficient will shield x-rays similarly effectively. While the drop in intensity with linear attenuation coefficient worsens the signal to noise ratio of these plots, it does not do so past the point of relevance.

At 23° and 67° for MPC Base, two of the largest primary peaks for struvite-k can be seen. These are consistent with literature values, as seen from Figure 32. The addition of aggregate lead and magnetite replacing some quantity of struvite-k decrease the relative intensity of these peaks when compared to elemental lead or various iron oxide compounds formed within the MPC.

Peaks that appear in the aggregate samples include those from elemental lead, which correspond to the high relative intensity peaks at 31° and 36° seen in Figures 35 and 36. Magnetite, based on the best peak matching, appears in mineral form in the compound magnesium iron oxide which manifests peaks at 30° , 35° , and 62° . The relative intensity between these peaks and those corresponding to struvite-k equalizes as aggregate concentration goes in, from MPC 2020 to MPC 3030. This is consistent with the aggregates being added replacing magnesium phosphate cement powder in the concrete mix. This all aides in verification of the basic composition of the MPC and aggregate MPC samples, but XRD is also able to compare samples before and after chemical reactions driving a material changing phase. Figure 37 shows the results of Figure 34, plotted below the results of XRD analysis on MPC Base after being driven through the dehydration reaction.

Here there is a significant and notable difference. As mentioned, struvite-k has primary peaks at 23° and 67° , which can be seen in black at those locations. These peaks are almost entirely absent in the red curve, which corresponds to the dehydrated sample of MPC Base. While not all of the struvite-k has been dehydrated, this severe drop in the relative intensity of struvite-k peaks to existing, and newly appearing, peaks signals a confirmation of the dehydration of struvite-k. Figure 37 is difficult to read, and so a peak intensity threshold figure will be used for further reference. Figure 38 shows all peaks with normalized intensity above a set threshold but maintains the same source data as Figure 37. Peaks are also labeled as they correspond to different compounds.

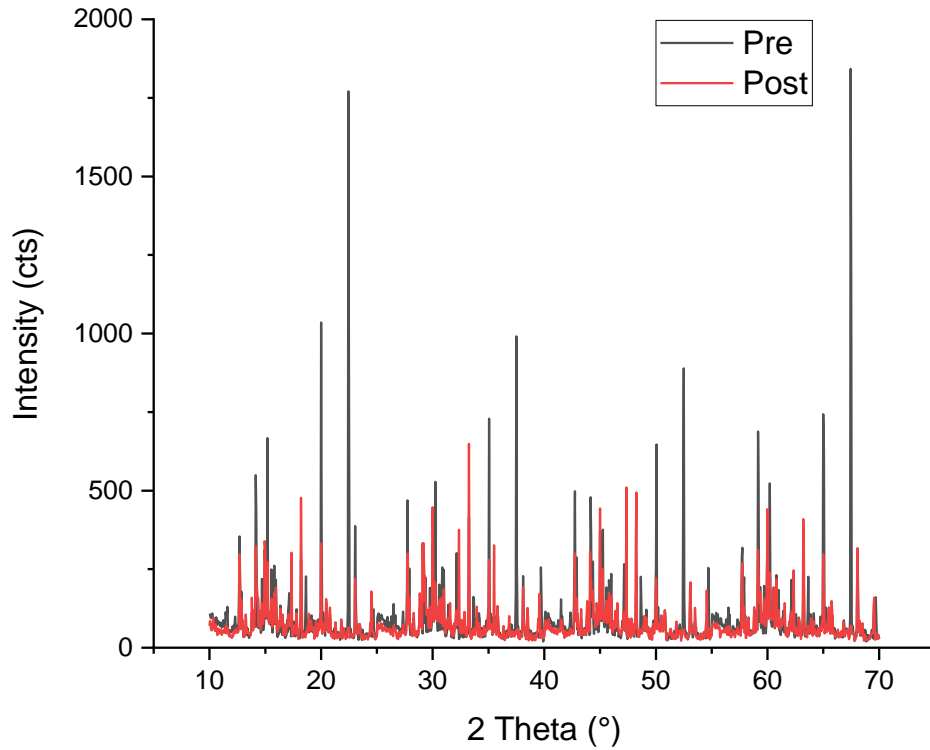


Figure 37. Plot of the peak intensity over the tested 2 theta range for MPC Base pre- and post-dehydration.

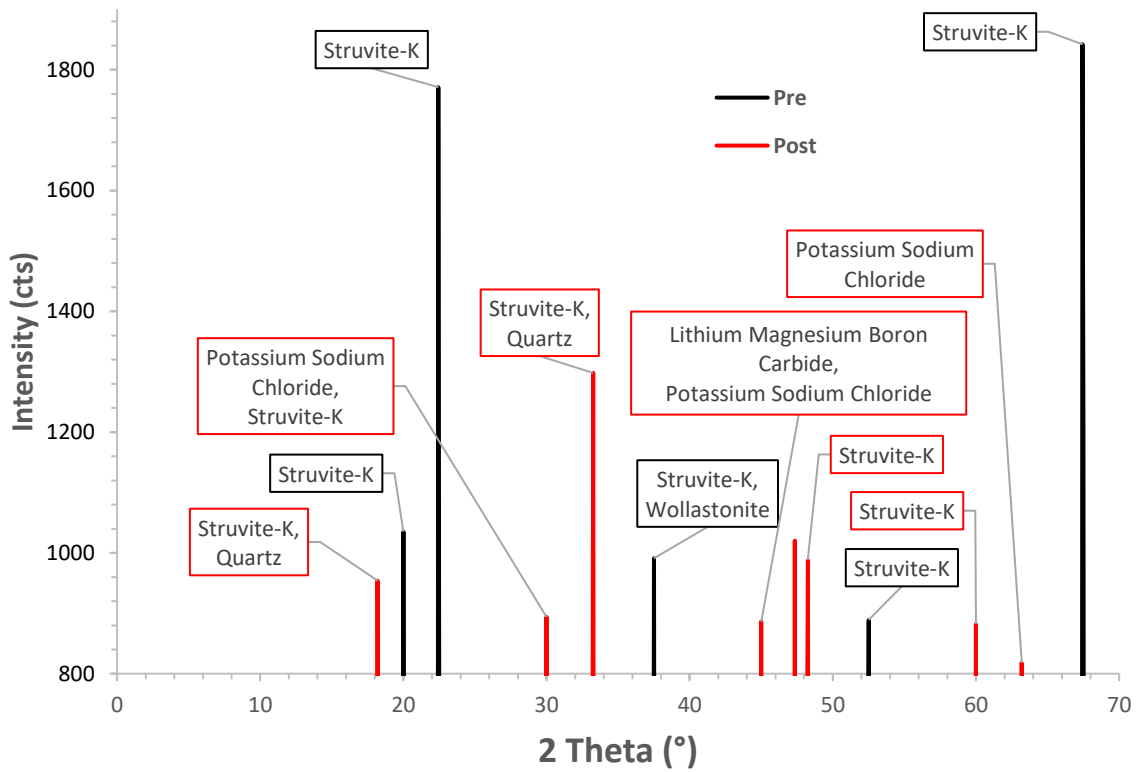


Figure 38. Comparative 2θ peak graphs showing pre- and post-dehydration MPC Base.

CaSiO_3 in wollastonite-2M form is the only other primary peak compound in MPC Base, other than the anticipated struvite-k. This is a typical byproduct of any natural mineral based concrete, as calcium silicates can form through a variety of mechanisms from a variety of sources. Once the material undergoes dehydration, both of the primary struvite-k peaks at 23° and 67° entirely disappear from the range shown, and what replaces them in relative intensity are a variety of secondary reaction products. The dehydration of struvite-k, or $\text{KMgPO}_4 \cdot \text{H}_2\text{O}$ as it appears elementally, is weakly bound K, Mg, and PO_4 . These compounds, based on the peaks shown in Figure 36, appeared to rebond to various lower concentration free elements that can exist within the bulk of the concrete, such as sodium, chlorine, lithium, and boron.

The next step in characterizing this dehydration was to perform scanning electron microscopy to visualize some of the potential microstructural degradation that will occur from dehydrating the strength compound, and with energy-dispersive x-ray spectroscopy to attempt to confirm the presence of some or all of these trace materials that the anhydrous struvite-k ions appeared to be bonding to after dehydration.

8.3.3 SEM and EDS Results

Using a Hitachi S3200N variable pressure scanning electron microscope in backscatter detector mode, with a Robinson backscatter detector, images were taken of the various samples. The imaging aspect of SEM can be used to gain information about the microstructural changes of this material through dehydration. MPC Base is a relatively smooth material, with minimal surface features, as is expected of a concrete with less inherent porosity than Portland. Figure 39 is a similar image to that of Figure 4, comparing Portland to MPC Base at 100x magnification. C-S-H, the primary hydration product in Portland concrete shows more features in general, and more discrete boundaries between phases.

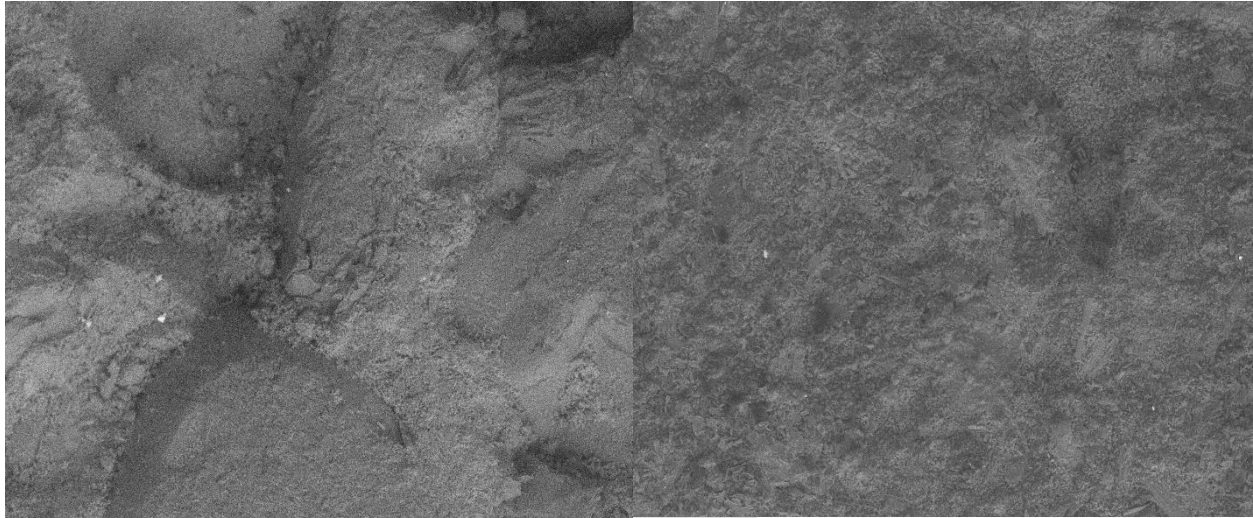


Figure 39. Portland (left) and MPC Base (right) at 100x magnification. Struvite-k (right) creates a relatively smooth and nonporous bulk when compared to C-S-H (left).

The lack of features shown in MPC Base at this magnification can be directly contrasted to MPC Base post-dehydration. Figure 40 shows MPC Base at a higher magnification pre- and post-dehydration, showing the growth of negative features. When driven through a dehydration reaction, bound water exited the material causing the struvite-k to become anhydrous which weakened it. This allowed voids and microcracks to form on the surface and in the bulk.

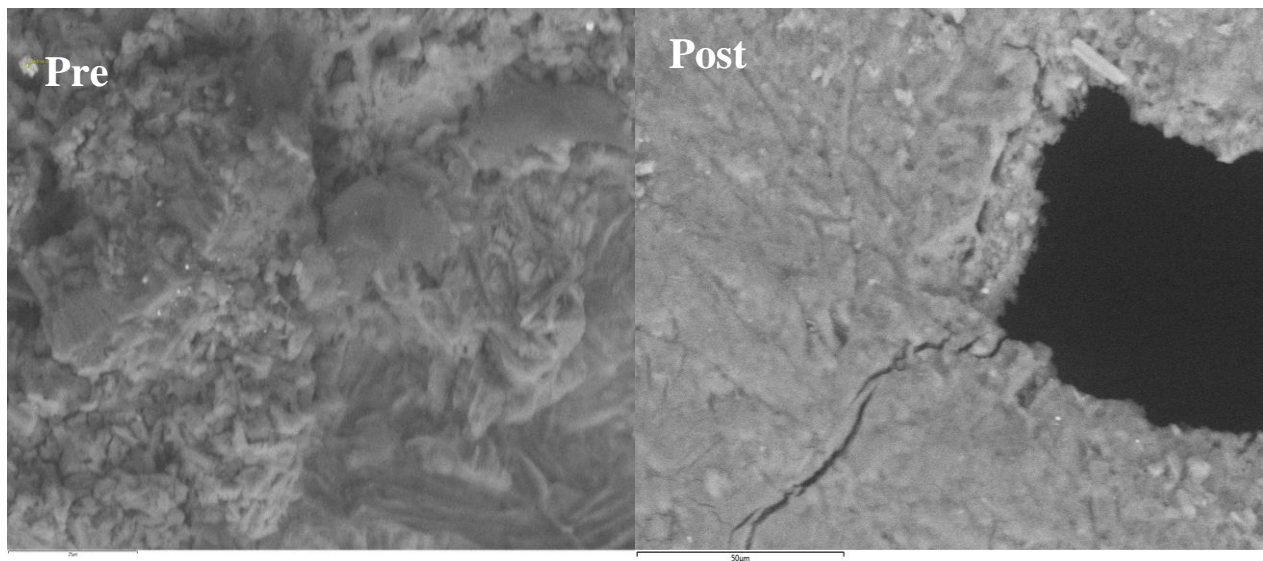


Figure 40. MPC Base pre- and post-dehydration at, left: 1000x; and right: 800x.

The void on the right was approximately 70 μm in width, which would be readily visible on a 100x magnification image. Any similar features noted in observation of the pre-dehydration MPC Base were larger in width and contained more crystalline deposits of struvite-k and wollastonite-2M,

indicating that these small width voids formed during the dehydration process. In addition, microcracks on the order of several microns in width and stretching for over a hundred microns in length emanate from this and other voids that were not present in the pre-dehydration sample.

Studies of microcrack propagation in concrete have shown that load stress is of higher concern to the propagation of microcracks in the mortar, or bulk, of a concrete than surrounding the joint to aggregates (Yamaguchi & Chan, 1991). Given the absence of aggregate bonds in this image, which was confirmed by EDS, these microcracks formed entirely within what Yamaguchi and Chan would call the mortar. The dehydration reaction drove microcrack propagation in the most vulnerable way that microcracks were able to propagate in a concrete, which indicated the phase change from struvite-k to anhydrous struvite-k would cause loss of strength, and decreased fracture resistance.

EDS was used first to confirm that each phase assumed to be present in the aggregate samples was indeed, present. Figure 41 shows an elemental mapping image of MPC 3030 at 1000x magnification. It has been colorized to distinguish between three clear elemental phases.

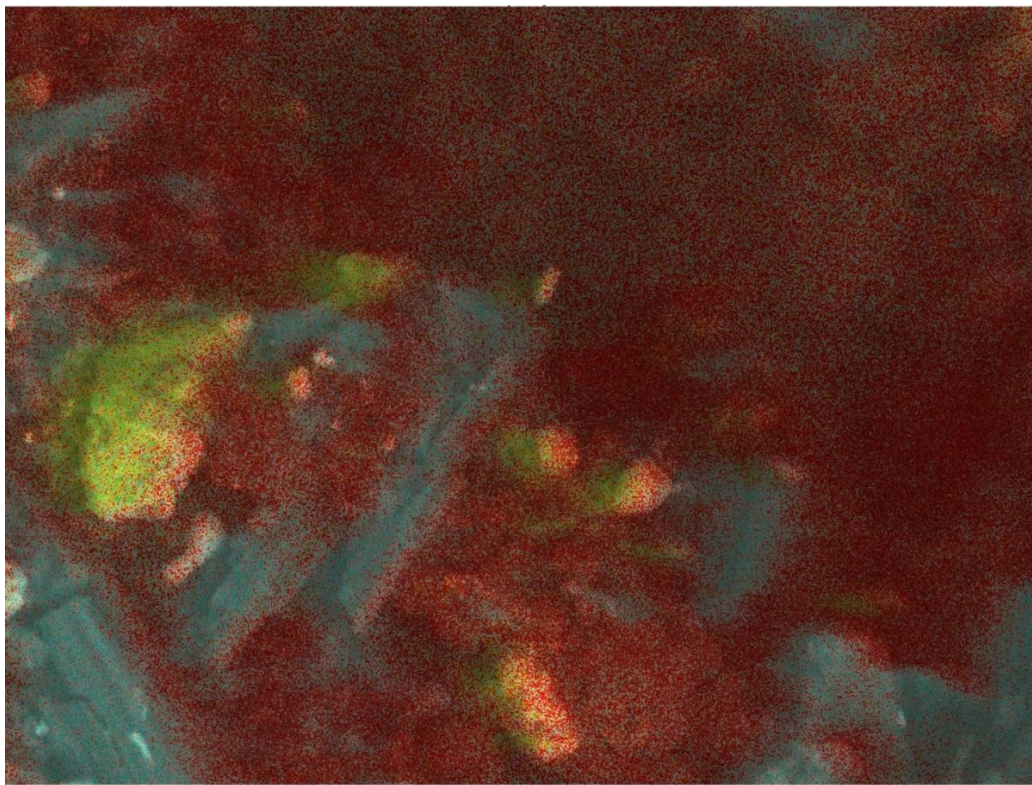


Figure 41. MPC 3030 at 1000x with EDS elemental mapping: Red - K, P, Mg, O, Fe; Cyan - Si, Ca; Lime - Pb.

The bulk of MPC 3030 maps very similarly to this representative image. Three distinct phases form within the material. The red corresponds to struvite-k (potassium, magnesium, phosphorus, and oxygen) as well as iron, which is in the form of magnetite (iron oxide). The cyan is calcium and silicon, likely in the form of wollastonite-2M as apparent from the XRD data. Finally, the lead is in elemental form in powder sizes as shown by the Lime.

Another way to visualize EDS data is through individual elemental maps. Figure 42 displays potassium, magnesium, phosphorus, and oxygen for MPC Base, at an image magnification of 100x. They overlap in incidence as they are all constituent elements of struvite-k which occupies the most space in MPC Base. Figure 43 shows the elemental maps of calcium, silicon aluminum, carbon, sodium, and iron.

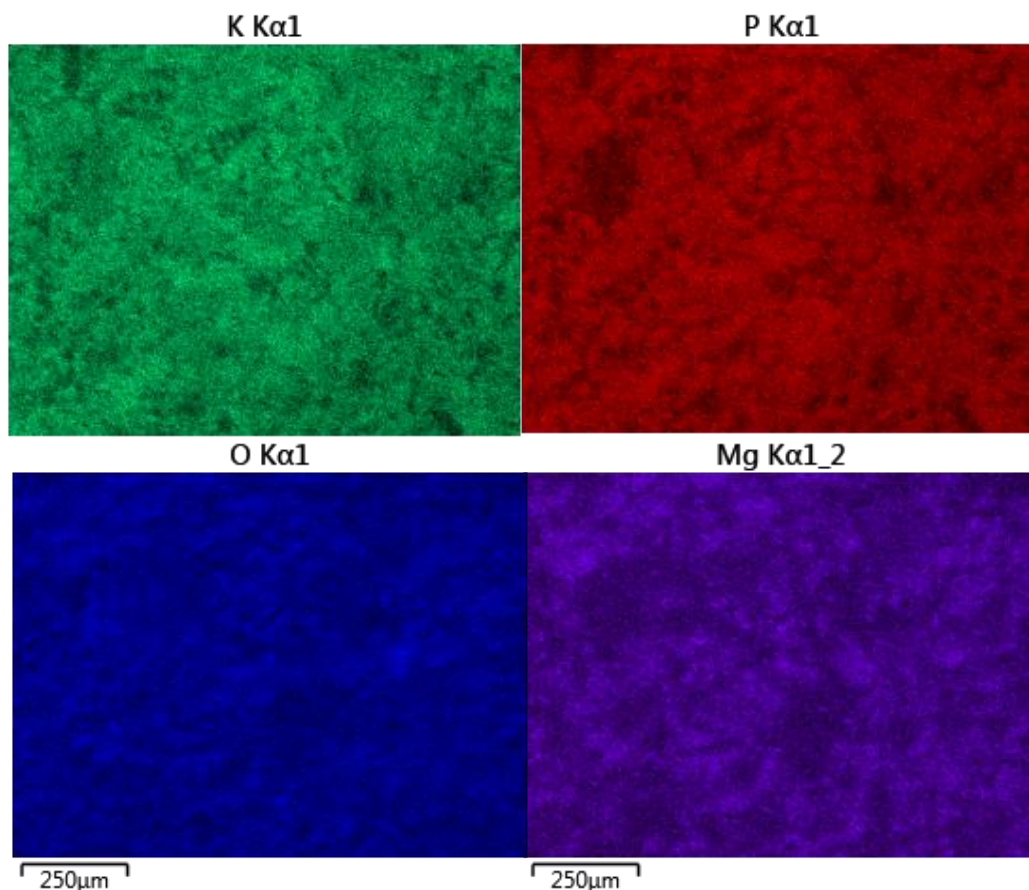


Figure 42. MPC Base at 100x, displaying individual element maps.

These simply showed further indication that the bulk of MPC Base, and all MPC compositions, are occupied by struvite-k. These subplots do not occupy the entire region shown, which indicated

that on this less microscopic scale there remains heterogeneity which is expected of concretes. Figure 43 shows similar elemental maps for additional elements within the MPC, several of which occupied the darker regions where struvite-k appeared to be absent in Figure 42. The presence of wollastonite-2M, for instance, is shown by the coincidence of calcium and silicon in regions of oxygen presence but potassium, phosphorus, and magnesium absence.

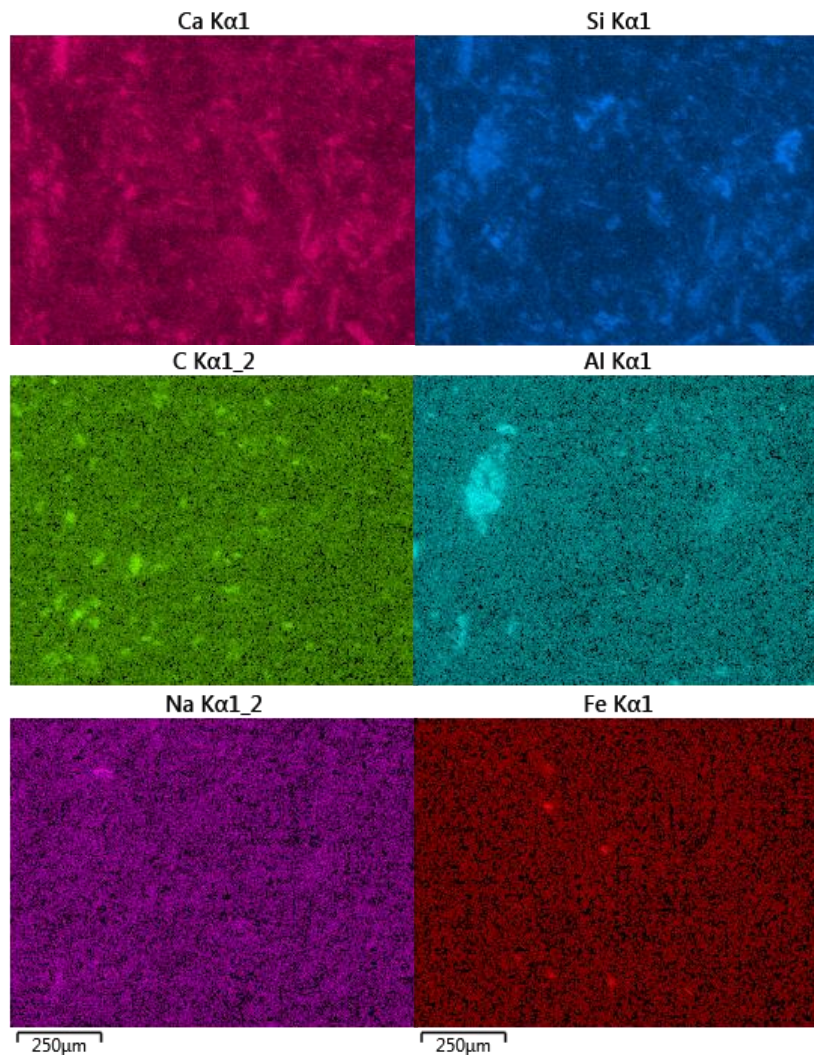


Figure 43. MPC Base at 100x, displaying different individual element maps.

In addition to the coincidence of calcium and silicon, there was a notable region of coincident aluminum and silicon that could be seen in a region with no magnesium or phosphorus presence, which indicated some potassium aluminum silicate, or an oxide thereof. There was also trace presence of carbon, sodium, and iron. The iron was likely due to contamination between sample

mixing, leftover from uncleaned tools during fabrication at the manufacturer and can be ignored. The sodium was a trace element that appeared to bond to potassium after dehydration, as was shown in Figure 38. One other element that appeared in the same figure that should be noted is lithium. This element is not detectable with EDS, as the emission of characteristic x-rays from electron bombardment is below the threshold which is observable from the detectors. Lithium's characteristic x-rays are only in the 40 V range, so the element cannot be mapped using EDS (Rollefson, 1925).

8.3.4 XPS Results

Initial survey scans of both the pre- and post-dehydration MPC Base were first made, to identify the basic composition of these powdered samples. They were taken using an XPS/UVS – SPECS System with PHOIBOS 150 Analyzer. Figure 44 shows the results of the survey scan of MPC Base before dehydration, while Figure 45 shows the results of the same range scan of MPC Base after dehydration.

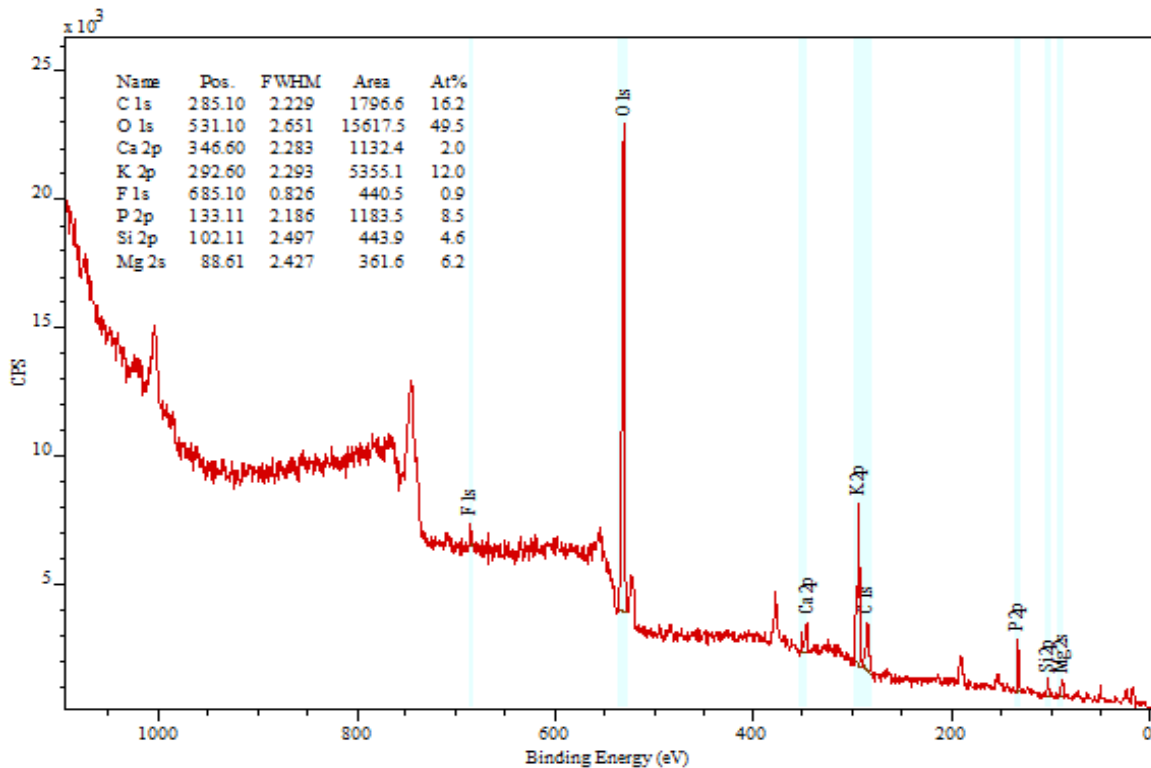


Figure 44. XPS survey scan of MPC Base pre-dehydration.

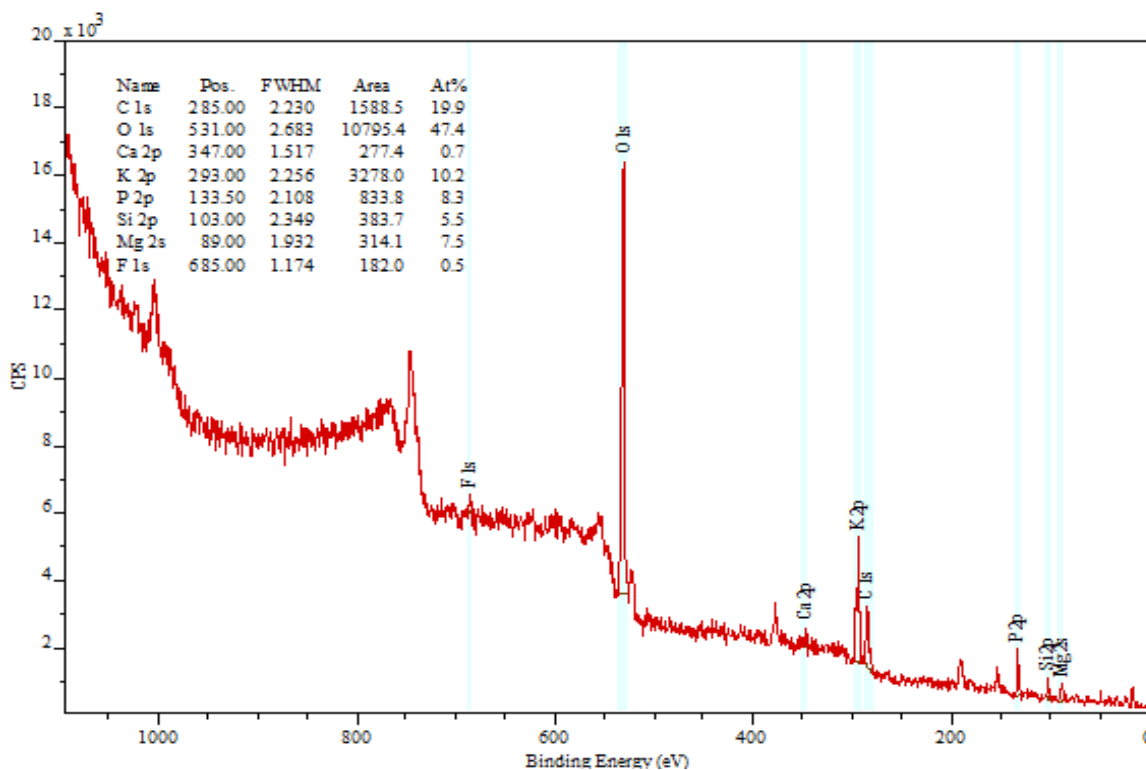


Figure 45. XPS survey scan of MPC Base post-dehydration.

The survey results appeared quite similar initially, which is not unexpected as the reorganization of elements within the samples is something XRD is more sensitive too than XPS. There appeared minor changes in the concentration of elements, the foremost of which was Oxygen. To compare these peak values, high-resolution scans of the oxygen peak for pre- and post-dehydration samples were performed and background corrected. The normalized peaks were plotted alongside each other in Figure 46.

As these were the highest relative intensity peaks within the MPC Base samples, the relative difference in intensity is the most visible. The drop in counts of approximately 33% accounted for a change in elemental composition corresponding to a 2% loss of oxygen. The compositional change between samples is done by the comparison of relative peaks within a sample, resulting in a relative composition of XPS identified elements. These can be compared between samples to identify variations. This method is somewhat inaccurate, losing precision to the inability for XPS to identify some low atomic weight elements, and is only applicable for the surface level.

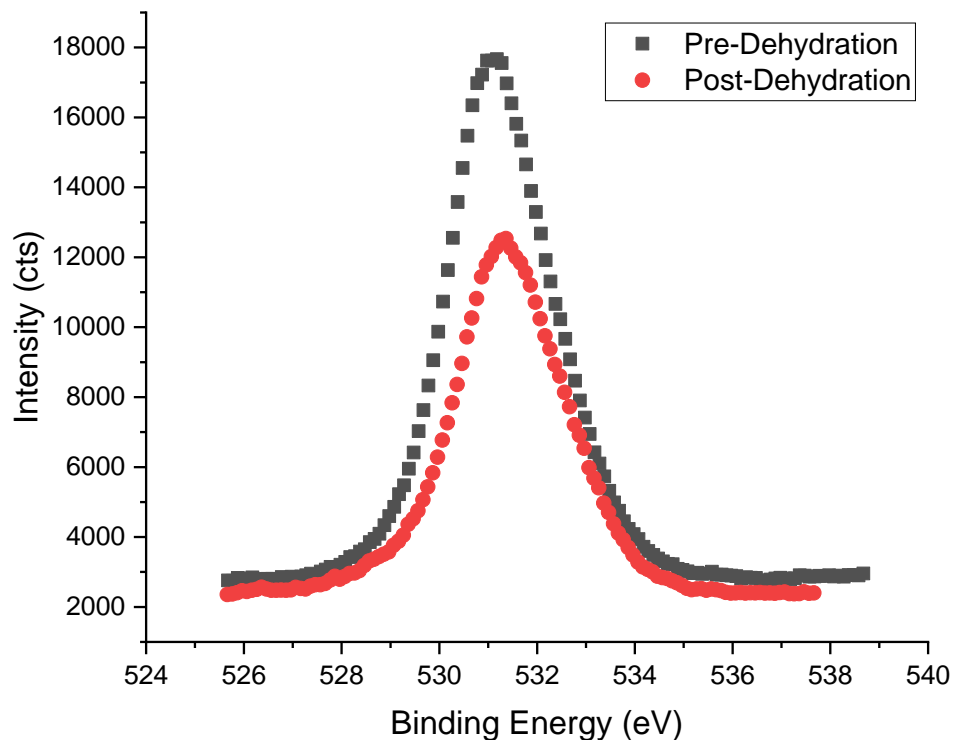


Figure 46. XPS high-resolution normalized peaks for pre- and post-dehydration MPC Base.

As the dehydration reaction studied is the volatilization of water (H_2O) from within struvite-k, a relative loss of oxygen was an expected outcome. Table 8 shows the elemental composition change from pre- to post-dehydration across all elements observed.

Table 8. The elemental change in percent of MPC Base from pre- to post-dehydration samples.

Carbon	Silicon	Fluorine	Phosphorus	Calcium	Magnesium	Potassium	Oxygen
+2%	+2%	0	0	-1%	-2%	-2%	-2%

While it may seem that a 2% variation in elemental composition between pre- and post-dehydration samples does not seem incredibly impactful, the dehydration reaction the samples were driven through only went through a 2% mass loss change, as opposed to the exhaustive full dehydration that studies show proceeds to 58.5% (Zhang, Shi, Huang, & Zhang, 2013).

The elemental analysis of these samples also showed the presence of another trace element that neither XRD nor EDS indicated, which is fluorine. EDS confirmed the presence of aluminum and sodium in the samples tested, while XPS confirmed the presence of fluorine but neither technique observed the trace elements present in the other. This continued to illustrate the challenge of elemental analysis on composite materials made in manufacturing conditions.

8.4 Dehydrated Mechanical Results

With the dehydration as fully characterized as possible, strict measurements of the material properties after dehydration were made using the same techniques as described in each individual chapter, the details of which will not be repeated. Figure 47 shows the results of ultimate compressive force before and after dehydration for MPC Base, MPC 2020, and MPC 3030 alongside that of Portland. Dehydration reduced the ultimate compressive force for MPC Base by 7.6%, MPC 2020 by 3.3%, and MPC 3030 by 0.2%. As the aggregate compounds in MPC 2020 and MPC 3030 replaced magnesium phosphate cement, they correspondingly replaced struvite-k in the hydrated concrete, so the impact of dehydration was mitigated in aggregate-rich samples. The dehydration of struvite-k as shown under SEM imaging introduced microcracks in the bulk, which were responsible for the largest degradation of mechanical properties under compression of any microcracks within concrete.

Loss of strength to heating has dire consequences for applications at elevated temperatures, such as the construction of dry-storage casks with the decay heat loads associated with the stored spent nuclear fuel.

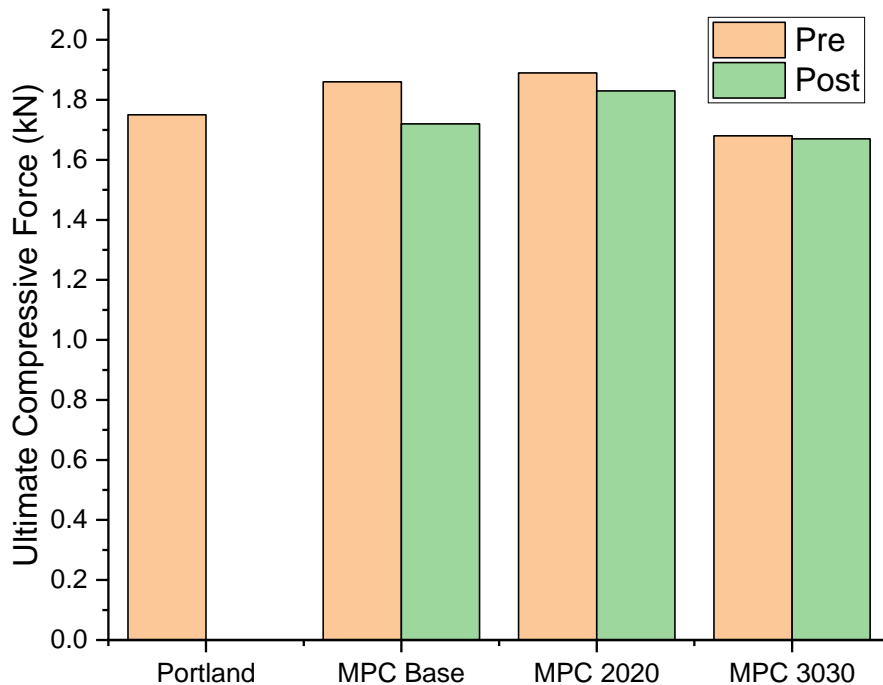


Figure 47. Ultimate compressive force results for MPC Base, MPC 2020, and MPC 3030 pre- and post-dehydration compared to Portland.

Similarly, there is a reduction in density associated with the loss of bound water and introduction of voids and cracks within the microstructure where water escaped, and anhydrous struvite-k began to degrade. In MPC Base this corresponded to a 2.0% loss in density, in MPC 2020 a 4.4% loss, and in MPC 3030 a 3.8% loss. The results of this evaluation are shown in Figure 48

A loss in density tends to directly impact the radiation attenuation capability of a material, as the voids and cracks that formed replaced shielding compounds far superior to air. The impact this dehydration had on the linear attenuation was studied next, for this reason.

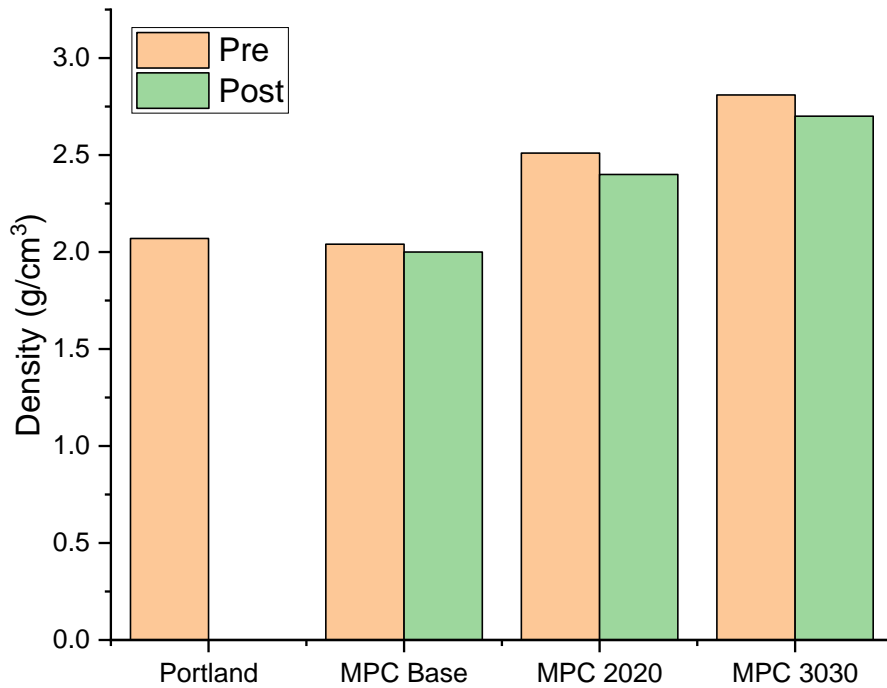


Figure 48. Density for MPC Base, MPC 2020, and MPC 3030 pre- and post-dehydration compared to Portland.

The impact of the dehydration reaction of these parameters is summarized in Table 9, reported as a percent deviation from the pre-dehydration samples.

Table 9. Mechanical property changes as a result of dehydration for MPC Base, MPC 2020, and MPC 3030.

Property	MPC Base	MPC 2020	MPC 3030
Density (g/cm ³)	-2.0%	-4.4%	-3.9%
Ultimate Compressive Force (kN)	-7.6%	-3.3%	-0.2%

8.5 Dehydrated Attenuation Results

Since the linear attenuation coefficient was deemed sufficient to discuss trends between samples, as confirmed by the comparison to the mass attenuation coefficient, it will be used to compare the samples pre- and post-dehydration. Figure 49 shows the linear attenuation coefficient of Portland alongside pre- and post-dehydration MPC Base, MPC 2020, and MPC 3030.

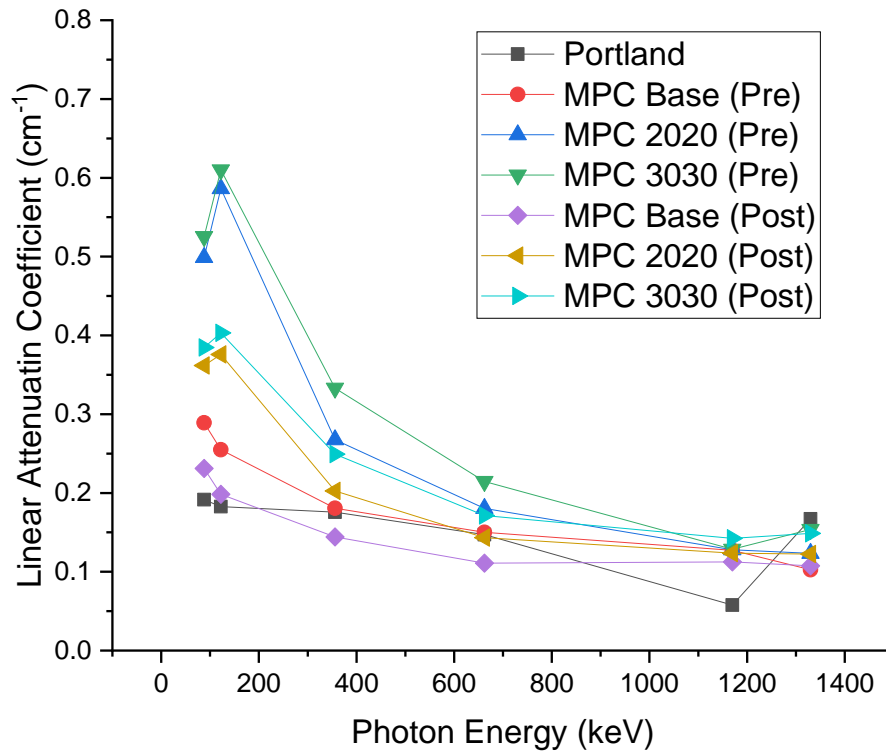


Figure 49. Linear attenuation coefficient for Portland, and pre- and post-dehydration MPC Base, MPC 2020, and MPC 3030.

Some apparent trends emerged from this investigation. The first pair of curves compared are those of the green and blue triangles to those of the cyan and gold triangles. Green and blue corresponded to the pre-dehydration aggregate samples, while cyan and gold corresponded to the post-dehydration samples. For both pairs of curves, a similar large reduction in attenuation occurred at low energies before tapering to relatively similar attenuation at higher energy levels. The same relative trend held true for MPC Base. Prior to dehydration (red circle) the material maintained better linear attenuation at low energies, while maintaining relatively similar levels at higher energies post-dehydration (purple diamonds). The average change in property with dehydration is summarized in Table 10.

Table 10. Average linear attenuation changes as a result of dehydration for MPC Base, MPC 2020, and MPC 3030.

MPC Base	MPC 2020	MPC 3030
-18%	-25%	-24%

8.6 Dehydrated Outgas Results

Repeating the experiments for outgas mass loss evaluation after the dehydration reaction occurred was less relevant than performing an outgas experiment as the samples were driven through the dehydration reaction. Given that in accident scenarios, in which the outgassing of a material entraining radioisotopes will involve heating events beyond the degradation temperature, hydrated struvite-k will implicitly be forced through a dehydration reaction. In these experiments, all conditions from Chapter 7 remained the same other than the temperature, which was set to 115 °C instead of 55 °C. The results of these outgas experiments are plotted alongside those from Chapter 7 for comparison in Figure 50.

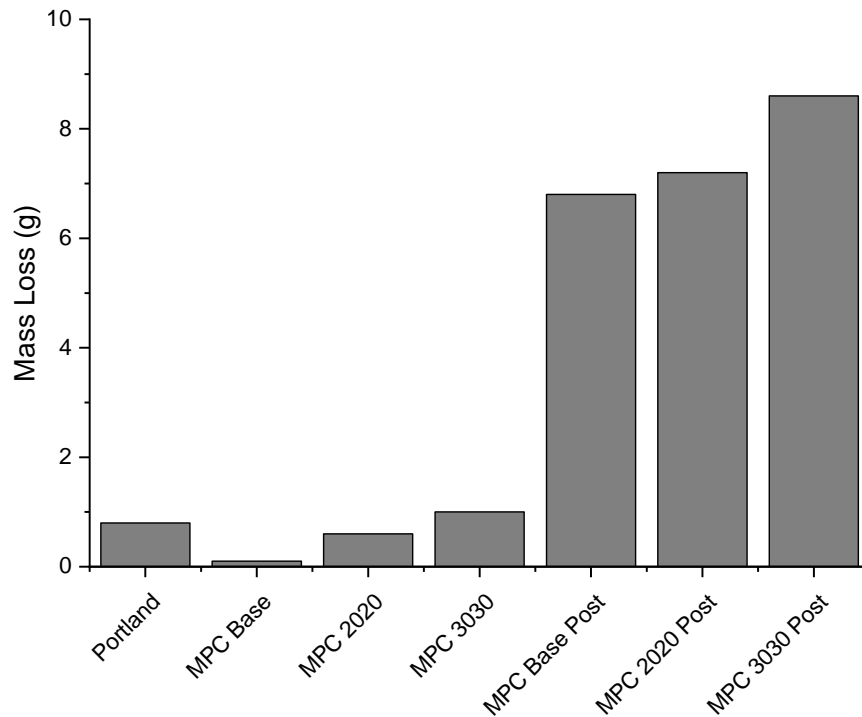


Figure 50. Outgas mass loss before dehydration and through dehydration for all tested samples.

The results are quite apparent, when mass loss was measured through a dehydration event, the MPC outgassed significantly more. MPC Base lost 242% more mass, MPC 2020 lost 217% more, and MPC 3030 lost 225% more. For entrainment conditions, this would be a severe breach of immobilization, and as such any immobilization applications would require that these materials be incapable of being dehydrated.

Chapter 9. Evaluation of the Suitability for Nuclear Waste Storage

9.1 Summary

The goal of this project was to optimize an aggregate composition for use with a magnesium phosphate cement binder to create a better shielding concrete, and thoroughly investigate its suitability for use in a variety of nuclear waste storage applications. This was done through experiments designed to evaluate the material characteristics related to gamma attenuation, mechanical strength, corrosive/erosive behavior, outgas mass retention, and thermal degradation.

First, magnesium phosphate concrete was tested based on gamma attenuation characteristics. Four aggregate materials each with several concentration variations were evaluated for their linear attenuation coefficient. This information, along with manufacturer provided ultimate compressive strength, informed the selection of an aggregate composition that seemed best suited for shielding gamma rays. By mass, 20% magnetite and 20% lead were chosen to make MPC 2020, and 30% magnetite and 30% lead were chosen to make MPC 3030. This was due to the magnetite improving the mechanical strength and workability of the concrete to offset the loss due to lead, which itself significantly improved the gamma attenuation. The chosen aggregate composition MPC were evaluated more rigorously alongside Portland and a traditional MPC as controls. The samples were tested for their resistance to corrosion/erosion in brine and acidic solution, with 60 day exposures and consistent mass tracking performed to evaluate the loss of material due to acidolysis and the growth of precipitate reactant due to corrosion. Then they were tested for mass retention through outgas conditions, being dried thoroughly and the loss of bound water due to heating compared to indicate the retention of entrained particles. Mechanical properties such as density and the ultimate compressive force were evaluated to confirm that the materials were capable of maintaining safe structural properties despite the large concentration of weakening aggregate introduced to improve

the radiation shielding properties. Finally, thermal degradation was thoroughly investigated experimentally and with analytical imaging due to the notable weakness of various concretes to heat. After being driven through a dehydration reaction as part of the evaluation of thermal degradation, several material properties were reevaluated to determine the suitability of the material after its thermal degradation mechanism.

9.2 Conclusions

Fast to cure and stronger than Portland, magnesium phosphate concretes provide an attractive topic of research for nuclear storage. Reducing the geographic footprint of spent fuel would enable more waste to be stored in existing areas. Improving the gamma attenuation of a shielding barrier allows less material to be used, which not only applies to spent fuel, but to immobilization and decay storage methods.

Based on the thorough evaluation of the thermal degradation properties of MPC Base, MPC 2020, and MPC 3030 it can be concluded that none of the MPC compositions are suitable for use in conditions with normal operating temperatures above 50 °C. This is due to the inherent breakdown of the primary strength-compound within the concrete, struvite-k. A material that thermally degrades and loses 18% of its ability to shield gamma radiation will consistently bring that shield below its safe limit. This is in addition to more than 7% loss to physical strength, which could weaken a structure to near the safety limits, and outgassing equivalent to 600% that of Portland. Accommodating these property losses would result in a shield that is no longer preferential to ordinary Portland concrete, thus failing as a true improvement to the material. This then excludes the materials from use in spent nuclear fuel storage, as the decay heat present from the highly radioactive fuel bundles within generate heat on the order of twice the safe limit for MPC. Such a waste package would internally dehydrate, building pressure within the material or driving large cracking through the overpack; in either case this package would fail within years, not decades.

Fortunately, several of the intended applications for nuclear waste storage do not involve elevated temperatures. Medical radioisotope disposal and many grouting applications are at ambient conditions. In such temperature ranges, MPC Base and MPC 2020 consistently outperform Portland. A summary of the improvements these materials convey below 50 °C can be seen in Table 11.

Table 11. Property comparison for rigorously tested samples below 50 °C.

Property	Portland	MPC Base	MPC 2020	MPC 3030
Linear Attenuation Coefficient (cm ⁻¹)	0.15	0.19	0.27	0.31
Mass Change from Circulator (mmpy)	-3.0	-1.0	-0.4	-0.3
Ultimate Compressive Force (kN)	1.8	1.9	1.9	1.7
Outgas Mass Loss (%)	0.29	0.04	0.18	0.26

For conditions under 50 °C, the gamma attenuation of both aggregate samples (MPC 2020 and MPC 3030) improved on the control groups by more than 70%. Basic mechanical evaluation of the ultimate compressive force showed minor improvement on the part of MPC 2020, and minor loss on the part of MPC 3030. Corrosion/erosion circulators provided a means to study the degradation of the material in acidic conditions and in brines; test results indicated that both aggregate samples had reduced mass loss due to acidolysis by more than a factor of two in highly acidic conditions. Long-time 55 °C drying was used to evaluate the mass retention due to outgassing of the materials, which was the only experiment in which aggregate samples underperformed compared to MPC Base, though all three retained more mass than Portland. For applications where material usage must be minimized while gamma attenuation maximized, such as in space constraining storage of grouting or radioisotope immobilization, MPC 2020 has superior characteristics.

9.3 Future Work

While the dehydration degradation of MPC 2020 is of significant concern, if temperature can be removed as a factor it is a superior material to that of most other concretes. For these reasons, further work can be done into the layering of concretes in structure design. MPC have a particularly beneficial property here, which is that they can form bonds to other concretes which are not weakened at the joint. For these reasons, protective layers of the more thermally resistant Portland, with thermally insulating aggregates such as polymers or even air, should be tested to allow more widespread use of materials like MPC 2020 which can deliver better shielding for less thickness.

References

- Ahn, K.-I., Shin, J.-U., & Kim, W.-T. (2016). Severe accident analysis of plant-specific spent fuel pool to support a SFP risk and accident management. *Annals of Nuclear Energy*, 70-83.
- Akkurt, I., Akyildirim, H., Mavi, B., Kilincarslan, S., & Basyigit, C. (2010). Gamma-ray shielding properties of concrete including barite at different energies. *Progress in Nuclear Energy*, 620-623.
- Alvarez, R. (2011). *Spent Nuclear Fuel Pools in the U.S.: Reducing the Deadly Risks of Storage*. Institute for Policy Studies. Washington, D.C.: U.S. Congress.
- Amritphale, S. S., Anshul, A., Chandra, N., & Ramakrishnan, N. (2007). Development of celsian ceramics from fly ash useful for X-ray radiation-shielding application. *Journal of the European Ceramic Society*, 4639-4647.
- Antonaci, P. (2013, April 11). Effects of Corrosion on Linear and Nonlinear Elastic Properties of Reinforced Concrete. *Cement and Concrete Research*, vol. 51, 51, 96-103.
- ASTM C185-15a. (2015). *Standard Test Method for Air Content of Hydraulic Cement Mortar*. Conshohocken: ASTM International.
- Barrow, A. R. (2010). Portland Cement in the Energy Industry. *OpenStax*.
- Baster, I. I. (1997). Calculation of radiation attenuation coefficients for shielding concretes. *Annals of Nuclear Energy*, 1389-1401.
- Bažant, Z. P. (1983). Mathematical model for creep and thermal shrinkage of concrete at high temperature. *Nuclear Engineering and Design*, 183-191.
- Beaudoin, J. J. (1990). *Handbook of Fiber-Reinforced Concrete: Principles, Properties, Developments and Applications*. Noyes Data Corporation.
- Bell, A. (2019). Building construction: The invention of reinforced concrete. In *Encyclopedia Britannica*. Britannica.
- Bertolini, L., Elsener, B., Pedferri, P., & Polder, R. (2004). *Corrosion of steel in concrete*. Wiley Online Publishers.
- Bjerge, L.-M., & Brevik, P. (2014). CO₂ Capture in the Cement Industry, Norcem CO₂ Capture Project (Norway). *Energy Procedia*, 6455-6463.
- Bowman, S. (2019). The Radioactive Dirt: An Analysis of the Role Information has Played Throughout Hanford's History. *Documents to the People*.
- Brichni, A., Hammi, H., Aggoun, S., & Adel, M. (2016). Optimisation of magnesium oxychloride cement properties by silica glass. *Advances in Cement Research*, 654-663.

- Brown, J. M. (1966). W. B. Wilkinson (1819-1902) and his place in the History of Reinforced Concrete. *Transactions of the Newcomen Society*, 129-142.
- Canadian Nuclear Safety Commission . (2019). *Ontario Power Generation Deep Geologic Repository*. Ottawa: Canadian Nuclear Safety Commission.
- Chang, C.-F., & Chen, J.-W. (2006). The experimental investigation of concrete carbonation depth. *Cement and Concrete Research*, 1760-1767.
- Choi, Y. S., & Yang, E. I. (2013). Effect of calcium leaching on the pore structure, strength, and chloride penetration resistance in concrete specimens. *Nuclear Engineering and Design*, 126-136.
- Collins, M. (2019). *Concrete at your fingertips: Heavyweight Concrete*. The Concrete Society.
- Condit, C. W. (1968). The First Reinforced-Concrete Skyscraper: The Ingalls Building in Cincinnati and Its Place in Structural History. *Technology and Culture*.
- Department of Civil Engineering. (2015). *History of Concrete Building Construction*. University of Memphis.
- Dhir, R. K., Brito, J., Silva, R. V., & Lye, C. Q. (2019). *Sustainable Construction Materials: Recycled Aggregates*. Elsevier Ltd.
- Doh, W. H., Papaefthimiou, V., & Zafeiratos, S. (2015). Applications of Synchrotron-Based X-Ray Photoelectron Spectroscopy in the Characterization of Nanomaterials. *Surface Science Tools for Nanomaterials Characterization*, 317-366.
- Dorrepaal, R. M., & Gowen, A. A. (2018). Identification of Magnesium Oxychloride Cement Biomaterial Heterogeneity using Raman Chemical Mapping and NIR Hyperspectral Chemical Imaging. *Scientific Reports*.
- Dutrow, B. L., & Clark, C. M. (2019). *X-Ray Powder Diffraction (XRD)*. Carleton College.
- Ekström, T. (2001). *Leaching of concrete : experiments and modelling*. Lund: Lund University.
- Elsener, B. (2013). *Corrosion of Steel in Concrete - Prevention, Diagnosis, Repair, 2nd Edition*. John Wiley & Sons Inc.
- Evdokimoff, V., Cash, C., Cardenas, A., & Buckley, K. (1994). Potential for Radioactive Patient Excreta in Hospital Trash and Medical Waste. *Health Physics*, 209-211.
- Farage, M. C., & Galle, C. (2003). Rehydration and microstructure of cement paste after heating at temperatures up to 300°C. *J Cement Concrete*, 1047-1056.
- Federally Funded Research and Development Center. (2019). *Review of the Final Draft Analysis of Supplemental Treatment Approaches of Low-Activity Waste at the Hanford Nuclear Reservation*. Richland: National Academies Press.

- Ferreira, M., & Simoes, A. (1995). Passivation of Reinforcing Steel in Concrete. *Materials Science Forum*, 891-898.
- Fischer, L. E., & Howe, A. (1999, September 1). Qualification of independent spent fuel storage installation. *Nuclear Engineering and Design*, 217-228.
- Gencturk, B., & Attar, A. (2015). Material Durability Performance of Reinforced Concrete Dry Cask Storage Systems for Nuclear Waste. *Structures Congress*. American Society of Civil Engineers.
- Ghandi, K. (2013). A Review of Ionic Liquids, Their Limits and Applications. *Green and Sustainable Chemistry*.
- González, J. A., Molina, A., Escudero, M. L., & Andrade, C. (1985). Errors in the electrochemical evaluation of very small corrosion rates—I. polarization resistance method applied to corrosion of steel in concrete. *Corrosion Science*, 917-930.
- Graeser, S., Postl, W., Bojar, H.-P., Berlepsch, P., Armbruster, T., Raber, T., . . . Walter, F. (2008). Struvite-(K), $\text{KMgPO}_4 \cdot 6\text{H}_2\text{O}$, the potassium equivalent of struvite – a new mineral. *European Journal of Mineralogy*, 629–633.
- Grangeon, S., Claret, F., Linard, Y., & Chiaberge, C. (2013). X-ray diffraction: a powerful tool to probe and understand the structure of nanocrystalline calcium silicate hydrates. *Acta Crystallographica*, 465-473.
- Greenberg, M., Lowrie, K., Burger, J., Powers, C., Gochfield, M., & Mayer, H. (2007). Nuclear Waste and Public Worries: Public Perceptions of the United States' Major Nuclear Weapons Legacy Sites. *Human Ecology Review*, 1-12.
- GROENEWOUD, W. M. (2001). CHAPTER 1 - DIFFERENTIAL SCANNING CALORIMETRY. In W. M. GROENEWOUD, *Characterisation of Polymers by Thermal Analysis* (pp. 10-60). Elsevier.
- Hager, I. (2013). Behaviour of cement concrete at high temperature. *Bulletin of the Polish Academy of Sciences: Technical Sciences*, 61.
- Head, M. K., & Buenfeld, N. R. (2006). Measurement of aggregate interfacial porosity in complex, multi-phase aggregate concrete: Binary mask production using backscattered electron, and energy dispersive X-ray images. *Cement and Concrete Research*, 337-345.
- Hewlett, P. (2019). *Lea's Chemistry of Cement and Concrete*. Elsevier Science & Technology.
- Huang, C.-C., & Wu, T.-Y. (2009). A study on dynamic impact of vertical concrete cask tip-over using explicit finite element analysis procedures. *Annals of Nuclear Energy*, 213-221.
- International Atomic Energy Agency. (2013). *The Behaviours of Cementitious Materials in Long Term Storage and Disposal of Radioactive Waste*. Vienna: International Atomic Energy Agency.

- Johnson, W. H., & Parsons, W. H. (1944). THERMAL EXPANSION OF CONCRETE AGGREGATE MATERIALS. *Journal of Research of the National Bureau of Standards*, 101-126.
- Kaech, A. (2013). *An Introduction to Electron Microscopy: Instrumentation, Imaging and Preparation*. Zurich: Center for Microscopy and Image Analysis.
- KAERI. (n.d.). *Table of Gamma Rays*. Retrieved from Nuclear Data Center at Kaeri: <http://atom.kaeri.re.kr:8080/gamrays.html>
- Kamal, M. M., Safan, M. A., Etman, Z. A., & Salama, R. A. (2014). Behavior and strength of beams cast with ultra high strength concrete containing different types of fibers. *HBRC Journal*.
- Kan, Y.-C., Pei, K.-C., & Chang, C.-L. (2004). Strength and fracture toughness of heavy concrete with various iron aggregate inclusions. *Nuclear Engineering and Design*, 119-127.
- Kaplan, M. F. (1989). *Concrete Radiation Shielding*. John Wiley and Sons Inc.
- Khan, S., Syed, A. T., Ahmad, R., Rather, T. A., Ajaz, M., & Jan, F. A. (2010). Radioactive Waste Management in A Hospital. *International Journal of Health Sciences*, 39-46.
- Kharita, M. H., Takeyeddin, M., Alnassar, M., & Yousef, S. (2008). Development of special radiation shielding concretes using natural local materials and evaluation of their shielding characteristics. *Progress in Nuclear Energy*, 33-36.
- Komloš, K., Babál, B., & Nürnbergerová, T. (1995). Hybrid fibre-reinforced concrete under repeated loading. *Nuclear Engineering and Design*, 195-200.
- Kosmatka, S. H., & Wilson, M. L. (1988). *Design and Control of Concrete Mixtures*. Portland Cement Association.
- Kotsovos, M. D. (1984). Concrete. A brittle fracturing material. *Materials and Construction volume*.
- Kousksou, T., Rhafiki, T. E., Mahdaoui, M., Bruel, P., & Zeraouli, Y. (2012). Crystallization of supercooled PCMs inside emulsions: DSC applications. *Solar Energy Materials and Solar Cells*, 28-36.
- Koyanbayev, Y. T., Skakov, M. K., Ganovichev, D. A., Martynenko, Y. A., & Sitnikov, A. A. (2019, April 11). Simulation of the Thermal Conditions of Cask with Fuel Assemblies of BN-350 Reactor for Dry Storage. *Science and Technology of Nuclear Fuel Installations*.
- Kurup, A. R., & Kumar, K. S. (2017). Novel Fibrous Concrete Mixture Made from Recycled PVC Fibers from Electronic Waste. *Journal of Hazardous, Toxic, and Radioactive Waste*.
- Laguitton, D., & Parrish, W. (1977). Experimental Spectral Distribution versus Kramers' Law for Quantitative X-ray Fluorescence by the Fundamental Parameters Method. *X-Ray Spectrometry*, 201.

- Lahalle, H., Coumes, C. C., Mesbah, A., Lambertin, D., Cannes, C., Delpech, S., & Gauffinet, S. (2016). Investigation of magnesium phosphate cement hydration in diluted suspension and its retardation by boric acid. *Cement and Concrete Research*, 77-86.
- Leung, C. K. (2001). Concrete as a Building Material. In *Encyclopedia of Materials: Science and Technology* (pp. 1471-1479). Elsevier Ltd.
- Levy, R., & Przyborski, P. (2019). *Acid Rain*. NASA Earth Observatory.
- Li, J., & Liu, Y. (2016). Thermal modeling of a vertical dry storage cask for used nuclear fuel. *Nuclear Engineering and Design*, 74-88.
- Li, J., Tharakan, P., Macdonald, D., & Liang, X. (2013). Technological, economic and financial prospects of carbon dioxide capture in the cement industry. *Energy Policy*, 1377-1387.
- Li, W., Zhang, D., Zhang, T., Wang, T., Ruan, D., Xing D., & Li H. (1999). *Study of solid–solid phase change of (n-C_nH_{2n+1}NH₃)₂MCl₄ for thermal energy storage*. *Thermochimica Acta*.
- Llorca, J., Needleman, A., & Suresh, S. (1991). An analysis of the effects of matrix void growth on deformation and ductility in metal-ceramic composites. *Acta Metallurgica et Materialia*, 2317-2335.
- Ma, F.-Y. (2012). Corrosive Effects of Chlorides on Metals. In N. Bensalah, *Pitting Corrosion* (pp. 139-178). InTech.
- Mahmud, I. (2019). *Difference Between Fine and Coarse Aggregate*. Civil Engineering Today.
- Mai, Y. W. (1979). Strength and fracture properties of asbestos-cement mortar composites. *Journal of Materials Science*, 2091-2102.
- Maslehuddin, M., Naqvi, A. A., Ibrahim, M., & Kalakada, Z. (2013). Radiation shielding properties of concrete with electric arc furnace slag aggregates and steel shots. *Annals of Nuclear Energy*, 192-196.
- Mattingly, J. (2020). *Ch. 8 - Radiation Detection Fundamentals*. Raleigh: NCSU.
- McWhinney, H. G., Cocke, D. L., Balke, K., & Ortego, J. D. (1990). An investigation of mercury solidification and stabilization in portland cement using X-ray photoelectron spectroscopy and energy dispersive spectroscopy. *Cement and Concrete Research*, 79-91.
- Meyers, R. (2008). Subcommittee on Energy and Air Quality Committee on Energy and Commerce. Washington, D.C.: U. S. House of Representatives.
- Mommaas, D. H. (2014). *Trends in global CO₂ emissions*. Netherlands Environmental Assessment Agency.
- Morita, M. (2018). Scanning Electron Microscope Energy Dispersive X-Ray Spectrometry. In *Compendium of Surface and Interface Analysis* (pp. 557-561). The Surface Science Society of Japan.

- Moulder, J. F. (1991). *Handbook of X-ray Photoelectron Spectroscopy: A Reference Book of Standard Spectra for Identification and Interpretation of XPS Data*. Perkin Elmer Corporation.
- National Research Council. (2006). *Safety and Security of Commercial Spent Nuclear Fuel Storage: Public Report*. Washington DC: The National Academies Press.
- Naus, D. (2005). *The Effect of Elevated Temperatures on Concrete Materials and Structures*. Oak Ridge National Laboratory. Oak Ridge, TN: U.S. Department of Energy.
- Nochaiya, T., Wongkeo, W., & Chaipanich, A. (2010). Utilization of Fly Ash with Silica Fume and Properties of Portland Cement–Fly Ash–Silica Fume Concrete. *Fuel*, 768-774.
- Noghabai, K. (2000). Beams of Fibrous Concrete in Shear and Bending: Experiment and Model. *Journal of Structural Engineering*.
- Nuclear Regulatory Commission. (1987). *Code of Federal Regulations: Title 10*. Washington DC: United States Government.
- Nuclear Regulatory Commission. (2011). *Dry Cask Storage of Nuclear Spent Fuel*. US Government.
- Nuclear Regulatory Commission. (2018). *What Are The Different Types of Radiation?* NRC.
- NUREG- 1275 . (1997). *Causes and Significance of Design Basis Issues at US Nuclear Power Plants*. Washington, DC: US Nuclear Regulatory Commission.
- Office of Medical Products and Tobacco, Center for Devices and Radiological Health. (2008). *Radiation Safety Considerations for X-Ray Equipment Designed for Hand-Held Use*. Washington, DC: U.S. Department of Health and Human Services.
- Office of Nuclear Material Safety and Safeguards. (2010). *Standard Review Plan for Spent Fuel Dry Storage Systems at a General License Facility: Final Report*. U.S. Nuclear Regulatory Commission. Washington, D.C.: U. S. Congress.
- Ouda, A. S. (2015). Development of high-performance heavy density concrete using different aggregates for gamma-ray shielding. *Progress in Nuclear Energy*, 48-55.
- Park, J. W., Kim, K. H., & Ann, K. Y. (2016). Fundamental Properties of Magnesium Phosphate Cement Mortar for Rapid Repair of Concrete. *Advances in Materials Science and Engineering*.
- Park, J. W., Kim, K. H., & Ann, Y. k. (2016). Fundamental Properties of Magnesium Phosphate Cement Mortar for Rapid Repair of Concrete. *Advances in Materials Science and Engineering*.
- Parker, R. P., Smith, P. H., & Taylor, D. M. (1984). *Basic Science of Nuclear Medicine*. Churchill Livingstone.
- Portland Cement Association. (2019). *Recycled Aggregates*. Portland Cement Association.

- Poursaeed, A., & Hansson, C. M. (2007). Reinforcing steel passivation in mortar and pore solution. *Cement and Concrete Research*, 1127-1133.
- Prassinis, P., Kimura, C., McCallen, D., Murray, R., Ravindra, M., Campbell, R., . . . Tong, W. (1989). *Seismic failure and cask drop analyses of the spent fuel pools at two representative nuclear power plants*. NRC, LLNL.
- Rao, A., Jha, K. N., & Misra, A. (2007). Use of aggregates from recycled construction and demolition waste in concrete. *Resources, Conservation and Recycling*, 71-81.
- Ravichandran, R., Binukumar, J. P., Sreeram, R., & Arunkumar, L. S. (2011). An overview of radioactive waste disposal procedures of a nuclear medicine department. *Journal of Medical Physics*, 95-99.
- Ravichandran, R., Binukumar, J. P., Sreeram, R., & Arunkumar, L. S. (2011). An overview of radioactive waste disposal procedures of a nuclear medicine department. *Journal of Medical Physics*, 95-99.
- Rodgers, L. (2018, December 17). Climate change: The massive CO2 emitter you may not know about. *BBC News*.
- Rollefson, G. H. (1925). Characteristic X-Rays from Lithium. *Physical Review Journals Archive*.
- Scrivener, K. L., Füllmann, T., Gallucci, E., Walenta, G., & Bermejo, E. (2004). Quantitative Study of Portland Cement Hydration by X-Ray Diffraction/Rietveld Analysis and Independent Methods. *Cement and Concrete Research*, 1541-1547.
- Sellevoid, E. J., & Bjøntegaard, Ø. (2006). Coefficient of thermal expansion of cement paste and concrete: Mechanisms of moisture interaction. *Materials and Structures*, 809-815.
- Šesták, J. (2005). *Science of Heat and Thermophysical Studies: A Generalized Approach to Thermal Analysis*. Elsevier.
- Shih, K., & Yan, H. (2016). The Crystallization of Struvite and Its Analog (K-Struvite) From Waste Streams for Nutrient Recycling. In K. Shih, *Environmental Materials and Waste* (pp. 665-686). Academic Press.
- Shirai, K., & Saesuga, T. (2006). Demonstrative drop tests of transport and storage full-scale canisters with high corrosion-resistant material. *International symposium on the packaging and transportation of radioactive materials* (p. 10). Berlin: Institute of Nuclear Materials Management, IAEA, BAM.
- Shohanna, I. (2015). Relation Between Density and Compressive Strength of Hardened Concrete. *Concrete Research Letters*.
- Shultis, J. K., & Faw, R. E. (1996). *Radiation Shielding and Radiological Protection*. Prentice Hall.
- Sindelar, R. L., Duncan, A. J., Dupont, M. E., Lam, P.-S., Louthan, M. R., & Skidmore, J. T. (2011). *Materials aging issues and aging management for extended storage and*

- transportation of spent nuclear fuel*. SRNL-STI-2011-00005, NUREG/CR-7116. Aiken, SC: Savannah River National Laboratory.
- Sonawane, T. R., & Pimplikar, S. S. (2019). Use of Recycled Aggregate Concrete. *Journal of Mechanical and Civil Engineering*, 52-59.
- Song, Y., Jiang, G., Chen, Y., Zhao, P., & Tian, Y. (2017). Effects of chloride ions on corrosion of ductile iron and carbon steel in soil environments. *Scientific Reports*.
- Sorrell, C. A. (1977). Suggested Chemistry of Zinc Oxychloride Cements. *Journal of the American Ceramic Society*, 217-220.
- Spalding, B. P., Hyder, L. K., & Munro, I. L. (1985). Grouting as a Remedial Technique for Buried Low-Level Radioactive Wastes. *Journal of Environmental Quality*, 389-396.
- Spence, R. D., Gilliam, T. M., Mattus, C. H., & Mattus, A. J. (1999). Laboratory stabilization/solidification of surrogate and actual mixed-waste sludge in glass and grout. *Waste Management*, 453-465.
- Stellman, J. (2012). Radiation: Ionizing. In J. Stellman, *Encyclopedia of Occupational Health and Safety*. International Labor Organization.
- Suryawanshi, V. B., & Chaudhari, R. T. (2014). Synthesis and Characterization of Struvite-k Crystals by Agar Gel. *Journal of Crystallization Process and Technology*, 212-224.
- Swanson, G. (2001). *Magnesium Oxide, Magnesium Chloride, and Phosphate-based Cements*. Building Biology Based New Building Protocol.
- Taylor, H. F. (1997). *Cement Chemistry, 2nd Ed*. London: Academic Press.
- Testimony of the Principal Deputy Assistant Administrator for the Office of Air and Radiation U.S. Environmental Protection Agency (U. S. House of Representatives July 15, 2008).
- Thayalan, K. (2014). *The Physics of Radiology and Imaging*. Jaypee Digital.
- Tufail, M., Shazada, K., Gencturk, B., & Wei, J. (2017). Effect of Elevated Temperature on Mechanical Properties of Limestone, Quartzite and Granite Concrete. *International Journal of Concrete Structures and Materials*, 17-28.
- U.S. Federal Highway Administration. (2007). *Silica Fume*.
- U.S. Nuclear Regulatory Commission. (2019, August). *Spent Fuel Storage in Pools and Dry Casks*. Retrieved from U.S. NRC: <https://www.nrc.gov/waste/spent-fuel-storage/faqs.html>
- Used Fuel Disposition Campaign. (2012). *Review Of Used Nuclear Fuel Storage and Transportation Technical Gap Analyses*. US Department of Energy. Washington, DC: U.S. Government.

- Vaccaro, S., Tobin, S. J., Favalli, A., Grogan, B., Jansson, P., Liljenfeldt, H., . . . Vo, D. (2017). *PWR and BWR Spent Fuel Assembly Gamma Spectra Measurements*. U.S Department of Energy.
- Wald, M. (2011, August 9). Researching Safer Nuclear Energy. *New York Times*.
- Walling, S. A., & Provis, J. L. (2016). Magnesia-Based Cements: A Journey of 150 Years, and Cements for the Future? *Chemical Reviews*, 4170-4195.
- Walling, S., & Provis, J. L. (2016). Magnesia-Based Cements: A Journey of 150 Years, and Cements for the Future? *Chemical Reviews*, 4170-4204.
- Weber, W. J., Navrotsky, A., Stefanosky, S., Vance, E. R., & Vernaz, E. (2009). Materials Science of High-Level Nuclear Waste Immobilization. *Materials Challenges for Advanced Nuclear Energy Systems*, 46-53.
- Werner, J. D. (2012). *U.S. Spent Nuclear Fuel Storage*. Washington, DC: Congressional Research Service.
- William, K., Rhee, I., & Xi, Y. (2005). Thermal Degradation of Heterogeneous Concrete Materials. *Journal of Materials in Civil Engineering*.
- William, K., Rhee, I., & Xi, Y. (n.d.). Thermal Degradation of Heterogeneous Concrete Materials.
- Xing, S., & al., e. (2017). Research on A3 steel corrosion behavior of basic. *Earth and Environmental Science* (p. 94). IOP Conference Series.
- Yamaguchi, E., & Chan, W.-F. (1991). Microcrack Propagation Study of Concrete under Compression. *Journal of Engineering Mechanics*.
- Yuan, C. Y., & Yehia, S. A. (2004). Evaluation of Electrically Conductive Concrete Containing Carbon Products for Deicing. *American Concrete Institute Materials Journal*, 287-293.
- Zhang, S., Shi, H.-S., Huang, S.-W., & Zhang, P. (2013). Dehydration characteristics of struvite-K pertaining to magnesium potassium phosphate cement system in non-isothermal condition. *Journal of Thermal Analysis and Calorimetry*, 35-40.